EUROPEAN LABORATORY FOR PARTICLE PHYSICS

Status report to the proposal SPSC-P-330

Report from the NA61/SHINE experiment at the CERN SPS

By the NA61/SHINE Collaboration
http://na61.web.cern.ch/

Abstract

This document reports on the status and plans of the NA61/SHINE experiment at the CERN SPS as of October 2016.

October 8, 2016

CERN-SPSC-2016-038 / SPSC-SR-197
08/10/2016

Contents

1 Introduction **5**

2 Data-taking Summary **5**

3 Facility Modifications **7**
3.1 Magnets . . . 7
3.2 Projectile Spectator Detector . . . 8
3.3 Vertex Detector . . . 11
3.4 Forward TPC . . . 13
3.5 Electronics upgrade . . . 15

4 Software and Calibration Modifications **17**
4.1 "Legacy" software maintenance . . . 17
4.2 NA61/SHINE IT infrastructure . . . 18
4.3 The deployment of the SHINE reconstruction within the production chain 18
4.4 Native SHINE software . . . 18
4.5 SHINE calibration . . . 20

5 New Results **21**
5.1 New results for physics of strong interactions . . . 21
5.2 Flow performance in Pb+Pb collisions . . . 37
5.3 New results for neutrino physics . . . 46
5.4 New results for cosmic-ray physics . . . 51

6 Proposed run schedule **56**

7 Ideas to Extend the NA61/SHINE Physics Program **57**

8 Summary **61**

A Vertex Detector: Tests on Beam, Integration, Hardware Upgrades and Software **64**
A.1 Analysis of data collected during November 2015 and July 2016 test. . . . 64
A.2 Latch-up protection and new firmware on TRBv3 . . . 71
A.3 Current status of sensor integration . . . 72
A.4 DAQ integration . . . 74
A.5 Tolerance of the VD sensors to heavy ions . . . 76
A.6 VD software status in SHINE . . . 80

B List of Recorded Data and Physics Results **84**

The NA61/SHINE Collaboration

A. Aduszkiewicz[18], Y. Ali[15], E. Andronov[24], T. Antićić[3], N. Antoniou[8], B. Baatar[22], M. Baszczyk[16], F. Bay[26], V. Blinov[7], A. Blondel[28], M. Bogomilov[2], A. Brandin[23], A. Bravar[28], J. Brzychczyk[15], S.A. Bunyatov[22], O. Busygina[21], P. Christakoglou[8], M. Ćirković[25], T. Czopowicz[20], A. Damyanova[28], A. Datta[32], N. Davis[13], H. Dembinski[5], M. Deveaux[7], F. Diakonos[8], S. Di Luise[26], P. von Doetinchem[32], W. Dominik[18], P. Dorosz[16], J. Dumarchez[4], R. Engel[5], A. Ereditato[27], G.A. Feofilov[24], Z. Fodor[9,19], A. Garibov[1], M. Gaździcki[7,12], M. Golubeva[21], K. Grebieszkow[20], A. Grzeszczuk[17], F. Guber[21], A. Haesler[28], T. Hasegawa[10], A.E. Hervé[5], M. Hierholzer[27], J. Hylen[29], S. Igolkin[24], A. Ivashkin[21], S.R. Johnson[31], K. Kadija[3], A. Kapoyannis[8], E. Kaptur[17], M. Kiełbowicz[13], J. Kisiel[17], V. Klochkov[7], N. Knezević[25], T. Kobayashi[10], V.I. Kolesnikov[22], D. Kolev[2], V.P. Kondratiev[24], A. Korzenev[28], V. Kovalenko[24], K. Kowalik[14], S. Kowalski[17], M. Koziel[7], A. Krasnoperov[22], W. Kucewicz[16], M. Kuich[18], A. Kurepin[21], D. Larsen[15], A. László[9], M. Lewicki[19], B. Lundberg[29], V.V. Lyubushkin[22], M. Maćkowiak-Pawłowska[20], B. Maksiak[20], A.I. Malakhov[22], D. Manić[25], A. Marchionni[29], A. Marcinek[15,19], A.D. Marino[31], K. Marton[9], H.-J. Mathes[5], T. Matulewicz[18], V. Matveev[22], G.L. Melkumov[22], A. Merzlaya[24], B. Messerly[33], Ł. Mik[16], G.B. Mills[30], S. Morozov[21,23], S. Mrówczyński[12], Y. Nagai[31], T. Nakadaira[10], M. Naskręt[19], M. Nirkko[27], K. Nishikawa[10], V. Ozvenchuk[13], A.D. Panagiotou[8], V. Paolone[33], M. Pavin[4,3], O. Petukhov[21,23], C. Pistillo[27], R. Płaneta[15], B.A. Popov[22,4], M. Posiadała[18], S. Puławski[17], J. Puzović[25], R. Rameika[29], W. Rauch[6], M. Ravonel[28], A. Redij[27], R. Renfordt[7], E. Richter-Wąs[15], A. Robert[4], D. Röhrich[11], E. Rondio[14], M. Roth[5], A. Rubbia[26], B.T. Rumberger[31], A. Rustamov[1,7], M. Rybczynski[12], A. Rybicki[13], A. Sadovsky[21], K. Sakashita[10], R. Sarnecki[20], K. Schmidt[17], T. Sekiguchi[10], I. Selyuzhenkov[23], A. Seryakov[24], P. Seyboth[12], D. Sgalaberna[26], M. Shibata[10], A. Shukla[32], M. Słodkowski[20], P. Staszel[15], G. Stefanek[12], J. Stepaniak[14], H. Ströbele[7], T. Šuša[3], M. Szuba[5], M. Tada[10], A. Taranenko[23], A. Tefelska[20], D. Tefelski[20], V. Tereshchenko[22], R. Tsenov[2], L. Turko[19], R. Ulrich[5], M. Unger[5], M. Vassiliou[8], D. Veberič[5], V.V. Vechernin[24], G. Vesztergombi[9,*], L. Vinogradov[24], M. Walewski[18], A. Wickremasinghe[33], A. Wilczek[17], Z. Włodarczyk[12], A. Wojtaszek-Szwarc[12], O. Wyszyński[15], L. Zambelli[4,10], E.D. Zimmerman[31], and R. Zwaska[29]

[1] National Nuclear Research Center, Baku, Azerbaijan

[2] Faculty of Physics, University of Sofia, Sofia, Bulgaria

[3] Ruđer Bošković Institute, Zagreb, Croatia

[4] LPNHE, University of Paris VI and VII, Paris, France

[5] Karlsruhe Institute of Technology, Karlsruhe, Germany

[6] Fachhochschule Frankfurt, Frankfurt, Germany

[7] University of Frankfurt, Frankfurt, Germany

[8] University of Athens, Athens, Greece

[9] Wigner Research Centre for Physics of the Hungarian Academy of Sciences, Budapest, Hungary

[10] Institute for Particle and Nuclear Studies, Tsukuba, Japan
[11] University of Bergen, Bergen, Norway
[12] Jan Kochanowski University in Kielce, Poland
[13] H. Niewodniczański Institute of Nuclear Physics of the Polish Academy of Sciences, Kraków, Poland
[14] National Centre for Nuclear Research, Warsaw, Poland
[15] Jagiellonian University, Cracow, Poland
[16] University of Science and Technology, Cracow, Poland
[17] University of Silesia, Katowice, Poland
[18] University of Warsaw, Warsaw, Poland
[19] University of Wrocław, Wrocław, Poland
[20] Warsaw University of Technology, Warsaw, Poland
[21] Institute for Nuclear Research, Moscow, Russia
[22] Joint Institute for Nuclear Research, Dubna, Russia
[23] National Research Nuclear University (Moscow Engineering Physics Institute), Moscow, Russia
[24] St. Petersburg State University, St. Petersburg, Russia
[25] University of Belgrade, Belgrade, Serbia
[26] ETH Zürich, Zürich, Switzerland
[27] University of Bern, Bern, Switzerland
[28] University of Geneva, Geneva, Switzerland
[29] Fermilab, Batavia, USA
[30] Los Alamos National Laboratory, Los Alamos, USA
[31] University of Colorado, Boulder, USA
[32] University of Hawaii at Manoa, USA
[33] University of Pittsburgh, Pittsburgh, USA
[*] Deceased

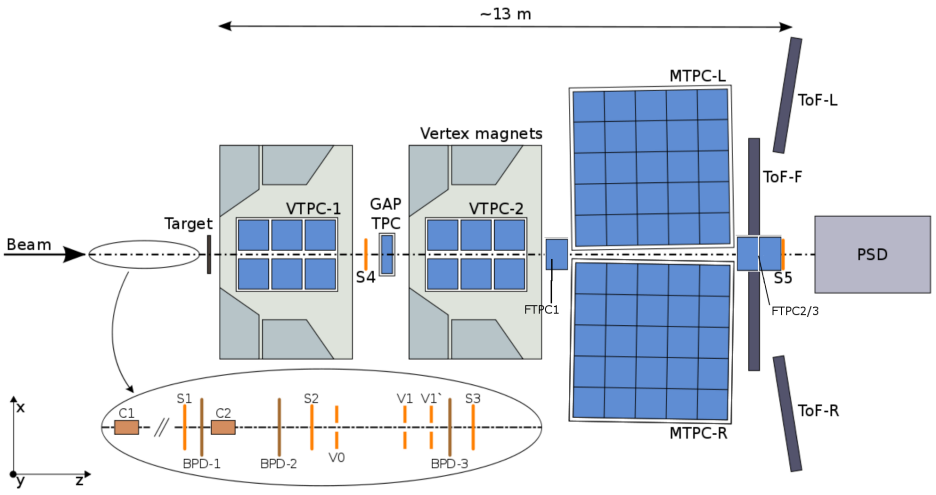

Figure 1: The NA61/SHINE detector.

1 Introduction

This annual report presents briefly the status and plans of the NA61/SHINE experiment [1], (see Fig. 1) at the CERN SPS. The report refers to the period October 2015 – October 2016.

The document is organized as follows. The data taking summary is given in Section 2. An overview on the detector maintenance and upgrades performed during the last year is given in Section 3, with additional details on the Vertex Detector in Appendix A. Progress in software and calibration as well as new results released in 2016 are briefly reviewed in Sections 4 and 5, respectively. Finally, plans for data taking in 2017-2018 are outlined in Section 6 and progress on the proposal to extend the NA61/SHINE physics program are summarized in Section 7. The summary in Section 8 closes the paper. Finally, the list of recorded data and corresponding physics results is given in Appendix B.

2 Data-taking Summary

The VERTEX-1 magnet failed in September 2015. Both VERTEX-1 and VERTEX-2 remained inoperative until May 2016. More details are given in Sec. 3.1.

Due to the magnet failure the data taking on inelastic p+p interactions at 400 GeV/c planned for October 2015 was cancelled. The beam time allocated in September 2015 for measurements of hadron production for Fermilab was used for measurements of cross sections of the hadron-nucleus collisions. In November the Pb+Pb collisions were measured, to evaluate possibility of the event plane determination in NA61/SHINE and numerous test of the detector. Table 1 summarises these measurements.

Table 1: Data collected without magnetic field in September–November 2015.

beam	target	beam momentum	number of events
π^+	C	31 GeV/c	1.11 M
π^+	Al	31 GeV/c	0.54 M
π^+	C	60 GeV/c	0.53 M
π^+	Al	60 GeV/c	0.35 M
K^+	Al	60 GeV/c	0.33 M
K^+	C	60 GeV/c	0.51 M
p	C	31 GeV/c	0.37 M
Pb	Pb	30A GeV/c	1.82 M

In November 2015 the Pb beam at 30A GeV/c was used for detector tests for future heavy ion data taking and potential extension of the NA61/SHINE data taking program after Long Shutdown 2. The beam and beam line were successfully tested with 8×10^5 Pb ions/spill. It was verified that the TPCs operate correctly with high multiplicity Pb+Pb collisions. The test was necessary, because it was hypothesised that the gas amplification may become less stable due to removal of flammable methane from the gas mixture in NA61/SHINE. The first evaluation of possibility to use S3 minimum bias trigger counter was performed with 500 μm thick scintillator (see analysis results in Sec. 5.2).

Tests of Small Acceptance Vertex Detector (see Sec. 3.3) and Projectile Spectator Detector (see Sec. 3.2) were performed. A test of the Scintillating Fibres was performed.

During the two week test period in May 2016 the Magnet Safety System was commissioned and the VERTEX magnets were tested successfully. 250 μm thick S3 prototype was tested. Tests and calibration of the Projectile Spectator Detector with new MPPCs were performed. However, due to beam stop between May 20 and 26 the planned program had to be narrowed.

Two weeks of the four week test period in July 2016 were used for SAVD installation and tests. The FTPC test planned during the last two weeks was postponed. The beam time was used for the data taking on p+C and p+Pb interactions. These reactions belong to the approved NA61/SHINE data taking programme. Table 2 summarises the data statistics.

The data taking period for Fermilab neutrino beams was started in September 2016, as scheduled. Table 2 lists the data already recorded, and planned to be recorded until October 18 within this program.

Table 2: Data collected with magnetic field in July, September and October 2016. The reactions ongoing and planned at the time of writing this report are marked with an asterisk (*).

beam	target	beam momentum	number of events
p	Pb	80 GeV/c	2.8 M
p	C	60 GeV/c	2.8 M
π^+	C	60 GeV/c	2.6 M
p	C	120 GeV/c	4.1 M
p	Al	60 GeV/c	3.2 M
p	Be	60 GeV/c	3 M*
π^+	Be	60 GeV/c	3 M*
p	Be	120 GeV/c	3 M*

3 Facility Modifications

The most important facility modifications performed during the last year are briefly summarized here.

3.1 Magnets

In September 2015 the VERTEX-1 superconducting magnet turned off with fast discharge emergency mode during test before the data taking. Subsequent attempts to turn it on resulted in instabilities in the liquid helium flow, and following two fast discharges. An investigation by EP-ADO revealed perturbation in the helium flow through the current leads. The existing quench protection system made it however impossible to check whether the magnet was damaged in the incident.

Installation of a new Magnet Safety System (MSS) to replace the old protection in VERTEX-1 and VERTEX-2 system was recommended by EP-ADO for any future operation of the magnets. The magnets remained turned off until the installation was complete in May 2016. The cryogenic system was maintained, repaired, and its parameters were optimised.

The tests performed with the new MSS revealed that VERTEX-1 is not damaged and can be used normally. Both magnets operate properly since then.

The details of the modifications are provided in presentations in Refs. [2–4]. A summary note by EP-ADO is in preparation.

The VERTEX-1 shutdown lead to significant changes and limitations of the NA61/

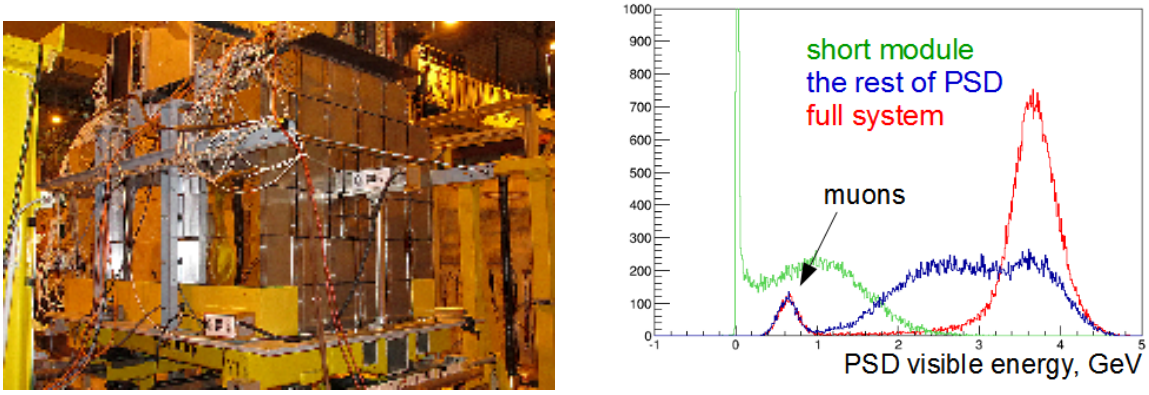

(a) (b)

Figure 2: (a) PSD with the short module installed and (b) energy spectra measured with the short module alone (green), without the short module (blue) and with PSD and the short module together (red).

SHINE data taking planned for September–December 2015. For details see Sec. 2.

3.2 Projectile Spectator Detector

Recent upgrades of the Projectile Spectator Detector (PSD) are summarized in this section.

3.2.1 Construction and test of short central module

A significant part of hadronic shower (about 12%) created by Ar ions escapes through the rear side of the calorimeter what leads to an underestimation of detected beam energy and affects the accuracy of the PSD trigger threshold. An additional short module was constructed in order to fix the problems. It consists of 12 lead/scintillator layers with 16 mm and 4 mm thickness, respectively. The lead/scintillator plates are tied together and placed in a box made of 0.5 mm thick steel. The transverse size of the module is 10×10 cm^2. A full length of the module corresponds to 1.2 nuclear interaction lengths comparing with 5.7 interaction lengths of the standard PSD modules. The short module installed before the PSD is shown in Fig. 2(a).

Performance tests were done with new short module in Fall 2015 during proton and Pb ion beams. Results of the tests are presented in Figs. 2(b) and 3. Energy spectra are presented in Fig. 2(b), calorimeter performance improvement is given in Fig. 3(a) and energy resolution curves are shown in Fig. 3(b). One can see that the short module improves energy resolution in higher energy range significantly (from ~9.4% to ~7.1%). Meanwhile a decrease of the resolution is small at low energies. The resolution drops here due to a small transverse shower leakage.

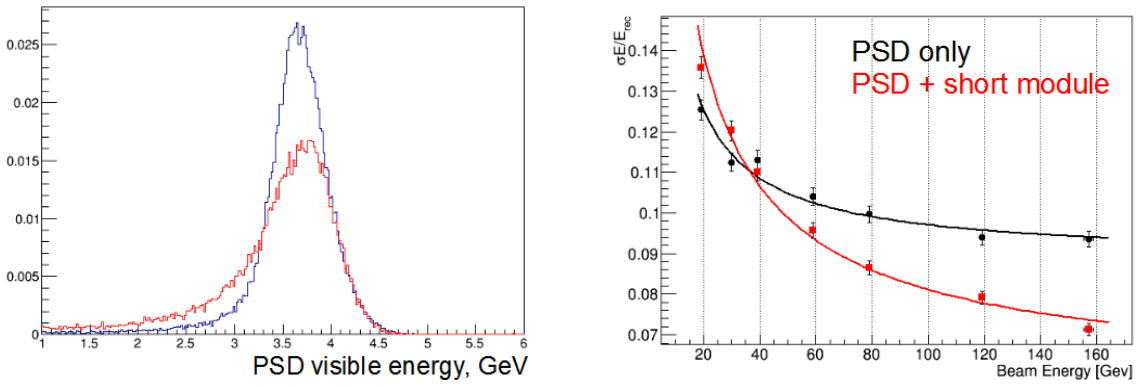

(a) (b)

Figure 3: (a) energy distribution spectra measured with PSD and the short module together (blue) with respect to the PSD alone(red); (b) energy resolution for PSD (black) and for PSD with the short module (red).

3.2.2 New photo-detectors for central modules

The light of WLS-fibres in PSD is read out by micro-pixel avalanche MAPD-3A photo-diodes with the size 3×3 mm^2. These photo-diodes have high dynamic range due to high density of about 10^4 pixels/mm^2 that is well matched for the calorimetry applications. However recovery time of the pixels reaches a few microseconds and might become significant to cause drop of the signal. This signal drop is observed in the central modules when they are irradiated with a high intensity heavy ion beam. The effect is shown in Fig. 4(a) with red dots. It was decided to replace MAPD-3A photo-diodes in central modules by fast silicon photo-multipliers recently developed by Hamamatsu Co to avoid the drawback. MPPCs S12572-010C/P were used to replace photo-diodes in 16 central modules. The recovery time of the pixels as well as the length of the single electron pulses is less than 10 ns. An exchange of photo-diodes in 16 central modules of the PSD has been done in February 2016. PSD performance with new photo-diodes is shown in Fig. 4(a) with blue dots. Small amplitude drop at high rates is due to limitation of current read-out electronics. In order to check performance of new MPPCs a fast read-out system was used based on DRS4 chip. Results of the test are given in Fig. 4(b).

Calibrations of PSD with new MPPCs has been done in summer 2016 using proton beams with momenta 20, 30, 40, 60, 80 and 150 GeV/c. Results of the tests are present in Fig. 5. The linearity of response is shown in Fig. 5(a) and the energy resolution is given in Fig. 5(b). Fit of the resolution results in stochastic term $68.36 \pm 0.01\%$ and constant term 0.031 ± 0.003. Noise term is close to zero.

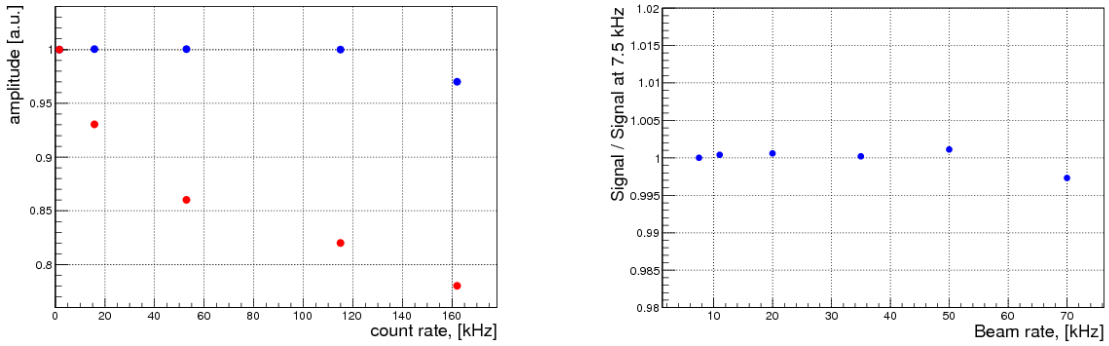

(a) (b)

Figure 4: (a) MAPD (red) and MPPC (blue) response as a function of proton beam intensity (rate) and (b) the beam rate dependence of MPPC response on Pb ions.

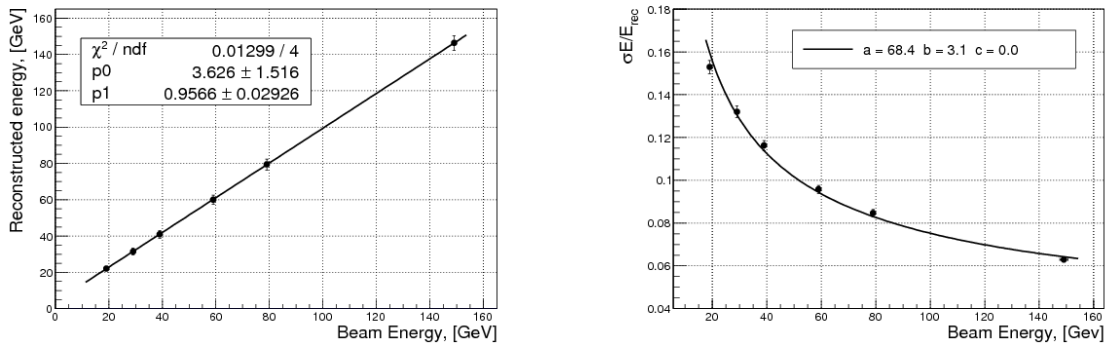

(a) (b)

Figure 5: (a) linearity of PSD response and (b) energy resolution measured for proton beams.

3.2.3 Vortex cooling for PSD compressed air cooling system

Silicon photo-diodes have a gain temperature coefficient of about 4%/(1° C). The temperatures are stabilized and controlled with an accuracy of about 0.01° C for each photo-diode using a cooling system based on Peltier elements. The photo-diodes of a single module are mounted on an aluminium plate which provides a common thermal contact to all 10 photo-diodes. Compressed air is used to cool an aluminium heat sink which is glued to the other (hot) side of the Peltier element. During beam tests in summer 2015 it was realized that the compressed air is not cold enough. A new stage of cooling was introduced based on vortex tube. Schematic view of a vortex tube is shown in Fig. 6(a). Pressurized air enters the tube and separates itself into hot and cold parts. Hot and cold air out from different sides of the tube. Cold air from the vortex tube is used in PSD

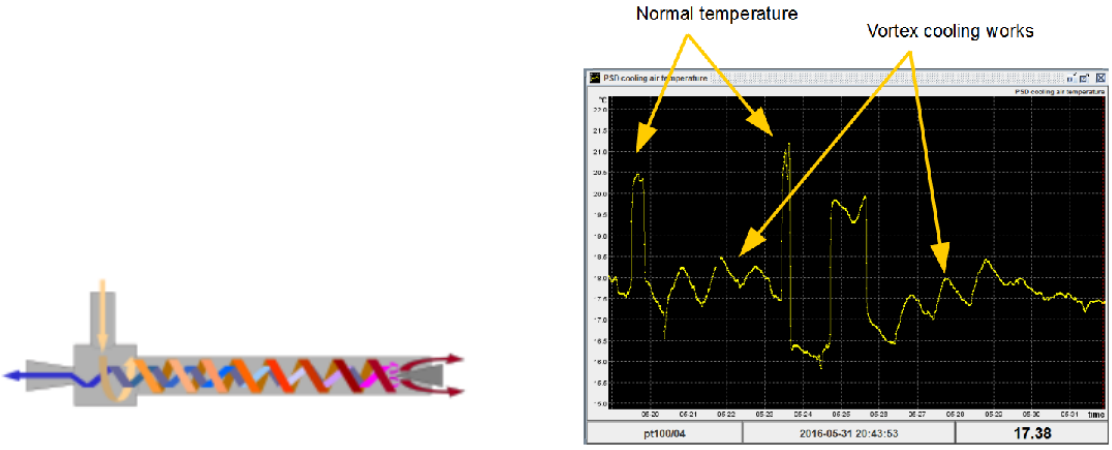

(a) (b)

Figure 6: (a) operational principle of a vortex tube and (b) results of vortex cooling tests.

cooling system as additional cooling element. Results of the tests are shown in Fig. 6(b). Vortex tube cooling system can drop compressed air temperature to 3° C with respect to the ambient one.

3.3 Vertex Detector

In 2015 the NA61/SHINE Vertex Detector (VD) program reached a phase of prototyping and tests on beam. According to the plan given in the VD project proposal [5] the first test of single MIMOSA-26AHR sensor was performed in November 2016 using Pb beam at 30A GeV/c. The main motivation of this measurement was to test the resistivity of MIMOSA-26AHR sensor to the heavy ion beam in regards to the latch-up effects. We used also the advantage of Pb beam availability to irradiate a set of different sensors with the high intensity beam to check their resistivity to the large radiation doses mostly in terms of the so-called NIEL effects. The tests performed in November are described in Appendix A Secs. A.1 and A.5.

In the fall of 2015 and the beginning of 2016 the preparations to the test of integrated detector have been conducted. The design of the start version of vertex detector named Small Acceptance Vertex Detector (SAVD) was described in Ref. [5]. Several activities were carried in parallel to accomplish construction of SAVD, namely:

- integration of sensors on the carbon fiber ladders,
- mechanical construction of SAVD which includes: mechanics structure of the inner arms, the helium box, sensor coolant distribution system and the signal feedthoroughs helium box side walls,

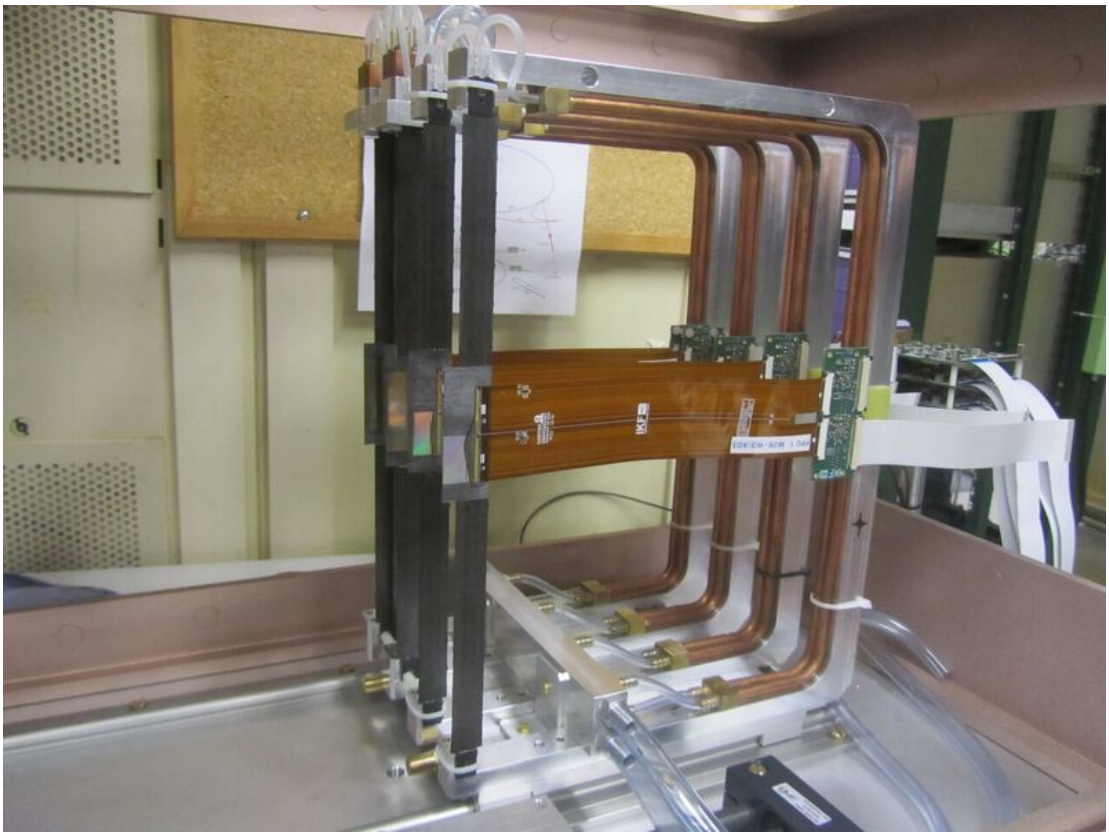

Figure 7: Inner arm of SAVD detector integrated for the test at CERN in July 2016.

- the VD DAQ adaptation to NA61/SHINE requirements and its integration with the central NA61/SHINE DAQ,
- installation of movable support platform for the SAVD detector installation on beam.

The sensor integration was carried out at the Goethe-University Frankfurt am Main. The sensors have been installed on the carbon fiber ladders deliver to NA61/SHINE from the ALICE collaboration together with the alignment system based on ruby balls. The ladders where developed and manufactured within the ALICE-ITS upgrade project [6]. The picture of integrated sensors on the carbon fiber ladders installed in the arm of SAVD can be seen in Fig. 7. The integration technology with the related aspects like sensors performance after full integration is described in details in Appendix A Sec. A.3.

The detail description of integration and modifications of the VD local DAQ system is provided in Appendix A in Secs. A.3 and A.4, respectively. Here the main effort was focused on writing new software to provide communication of the low level VD DAQ system with high level central NA61/SHINE DAQ and to upgrade the peripheral FPGA code and firmware used on Converted Board micro-controller. This upgrades were introduced to provide synchronization and the latch-up protection to sensors.

In July 2016 the integrated detector was transported to CERN and installed in the NA61/SHINE experimental area for the test on beam of protons at 150A GeV/c. The analysis of data collected during the test demonstrated the ability of the detector to reconstruct tracks with expected position resolution of about 4 μm and the ability of the primary vertex reconstruction. The description of the test, details of data analysis and the obtained results are presented in Appendix A Sec. A.1.

In parallel to the hardware activities the VD related software is being developed within the NA61/SHINE software framework SHINE. The main challenge of this software is to provide high efficient tracking in the in-homogeneous magnetic field present in the VD location. The progress on this field is described in Appendix A Sec. A.6.

3.4 Forward TPC

The forward tracking subproject is intended to allow the measurement of secondary protons in the moderate- to high-x_F region. This is primarily motivated by interaction studies for the neutrino program, where these protons are responsible for up to 25% of the ν_μ flux in the NuMI beam and likely a comparable fraction in the LBNF beam. A secondary goal of the system is to measure the high-momentum part of the π^+ production.

The NA61/SHINE detector is designed primarily to track particles that bend out of the beam; only one small tracking detector, the GAP TPC (GTPC), covers the forward region. We are instrumenting the forward region with two TPCs, one immediately upstream and one immediately downstream of the MTPCs. The new TPCs will have electric field and readout geometry based largely on the existing NA61/SHINE TPCs, and will use existing spare electronics. One chamber will be placed immediately upstream of the MTPCs and the other (with two field cages) immediately downstream of the MTPCs (see Fig. 1).

Higher-rate running conditions are expected to generate enough tracks in the beam region so that out-of-time tracks may produce significant backgrounds. Out-of-time tracks are reconstructed as spatially separated tracks. In order to reject these tracks, successive field cages will have opposite drift directions so out-of-time tracks will appear unconnected at chamber boundaries. This "tandem TPC" concept originated with the Budapest group and will be implemented for the first time here.

3.4.1 Design and construction

The chambers have been designed, to the extent practical, to take advantage of the existing infrastructure of NA61/SHINE. They will use spare front-end boards, readout motherboards, and data concentrators (motherboard-DAQ interface). Drift field high-voltage supplies of the same model used for the MTPCs have been purchased from Heinzinger. The pad plane and wire grid arrangement for the upstream chamber is the same as a single module of the MTPCs, with twelve full rows of 4×40 mm^2 pads.

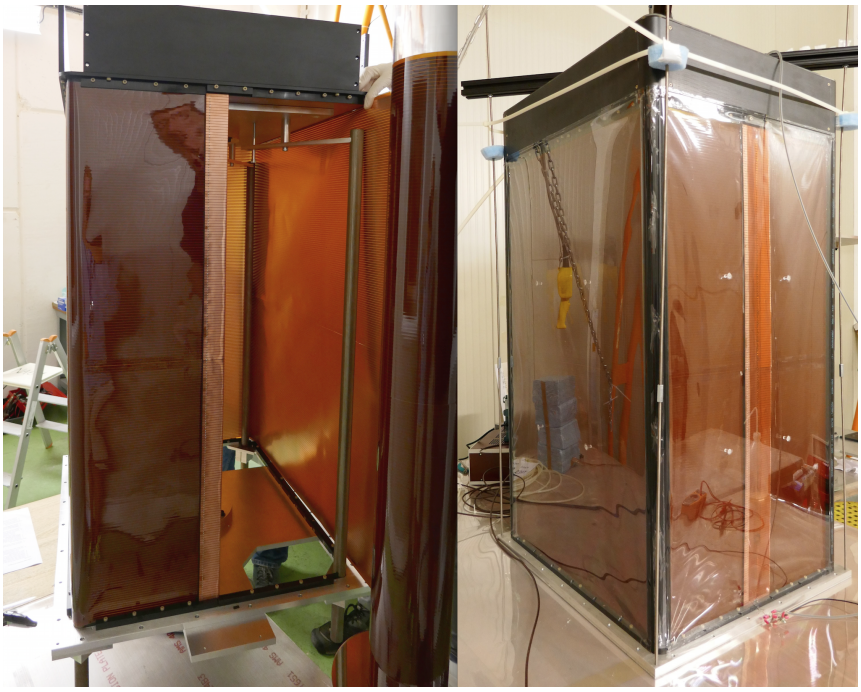

Figure 8: Left: top hat during field cage wrapping, July 2016. Right: completed FTPC1 "top hat".

The downstream chamber will be a two-cage tandem system. The upstream and downstream pads will be of the normal size, with larger pads in the center in order to maximize dE/dx coverage while minimizing the channel count.

The FTPCs use a novel field cage made of etched polyimide films with divider resistors soldered directly to the film. The field cage and cathode are built as a single detachable assembly (the "top hat", see Fig. 8).

The pad plane and wire grid for each field cage has been assembled separately into a wire grid module that will be attached to the top hat only at the final assembly stage of the chamber. The wire grid components were produced at the University of Colorado, and the wire winding for FTPC1 (see Fig. 9) was completed at KFKI-Wigner (Budapest) and delivered to CERN in June 2016. The remaining wire grids are scheduled for winding in autumn 2016.

3.4.2 Gas system

The chambers' gas system will use a simple one-way flow of Ar+CO_2, the same mixture used by the other TPCs in NA61/SHINE. The system consists of 3 separate gas mixing stations, 3 separate gas lines and 3 separate drift monitoring subsystems (one for each FTPC gas volume). Gas mixing is provided by a BetaErg set-up (2 mass flow flowmeters with controllers and power supplies). The gas lines are constructed with stainless steel

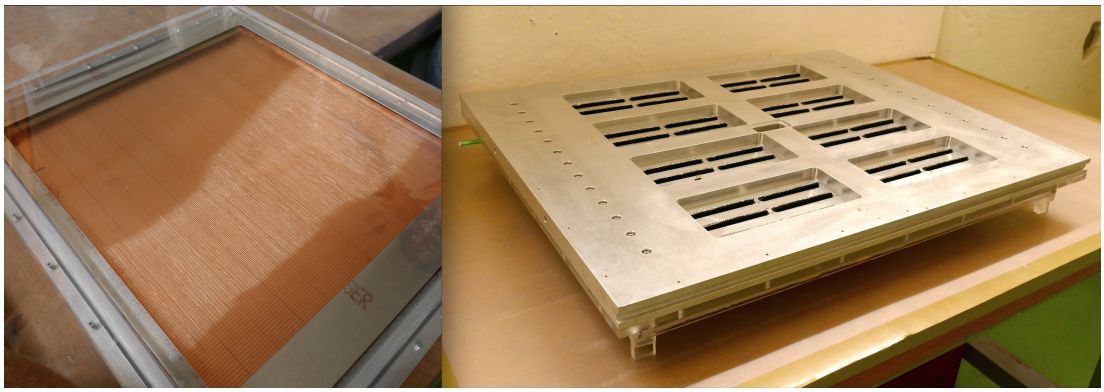

Figure 9: Top and bottom views of the wire grid module for FTPC1.

pipes. Drift velocity is monitored by three newly constructed drift velocity monitors. The complete monitors with α sources of special design and readout [7] were installed and tested in the experiment. An oxygen content monitoring system was also provided. The system consists of one OEM Zircodox (by Gruter & Marchand) sensor and is common for all FTPC chambers. Its design allows for monitoring of one chamber at a time. Further development of the system is proposed: overpressure monitoring in the chambers will be installed. Also, additional monitoring is proposed to monitor pressures in the TPCs simultaneously with drift velocity in order to provide an easier and more accurate drift velocity calibration.

3.4.3 Assembly and installation plans

As of the completion of this Status Report, all major components of the FTPCs have been procured. The wire grid module has been completed for FTPC1 and the field cage has been wrapped and tested for gas leaks and high voltage problems. The two subassemblies are scheduled for assembly soon, with installation in the beam planned to take place before the end of 2016.

The assembly and installation of FTPC2 and FTPC3 are planned for completion in time for summer 2017 data taking.

3.5 Electronics upgrade

The NA61/SHINE readout electronics has been inherited from the NA49 experiment. We decided to replace and upgrade the old electronics using the DRS digitizer developed at PSI [8]. The development of the new readout electronics is close to completion. For details on the overall structure and functioning of the new DRS readout see the 2013, 2014, and 2015 Status reports.

Figure 10 shows the DRS readout board for the NA61/SHINE DAQ upgrade developed at the University of Geneva. It contains 32 analog inputs, 4 DRS chips, an 8 channel

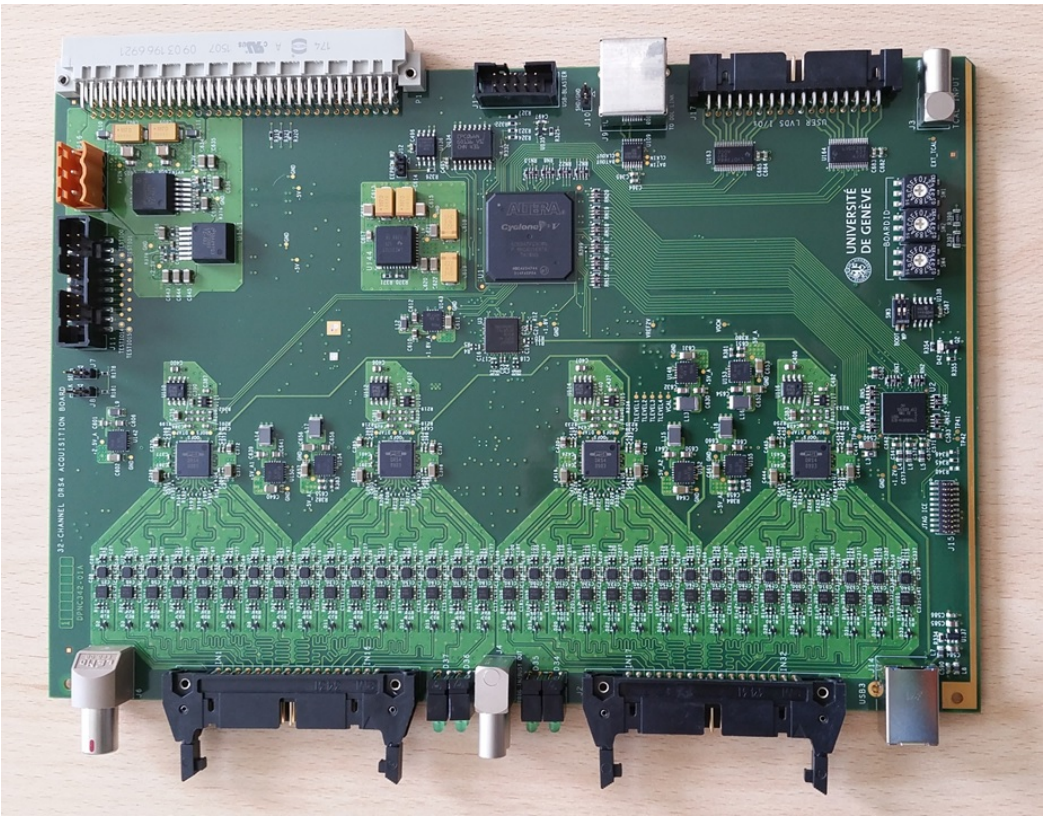

Figure 10: 32 channel DRS board.

12 bit ADC for the digitization of the waveforms sampled in the capacitor arrays, and a Cyclone V FPGA. Two readout solutions are foreseen: the first via the USB 3.0 microcontroller currently used for debugging end evaluating the board in detail, the second via the DDL link (4 LVDS lines with a RJ45 connector), which needs still to be implemented. The trigger can be distributed via the front panel or the backplane. The DRS boards are being currently evaluated and the FPGA program is being developed. So far no hardware issues of strange behavior have been observed. A small system consisting of 8 DRS boards for a total of 256 channels will be tested in a beam before the end of the year. If successful, the system will be ready for mass production at the beginning of 2017.

Up to 16 DRS boards will be housed in 6U custom crates provided by Wiener. A custom backplane under development will be used for powering the boards, distribute the control signals and receive status signals, distribute clocks, and daisy chain the programming of the boards in the crate.

Figure 11 shows the linearity of the amplitude sampling over the whole dynamic range of the DRS digitizer for a channel picked up randomly. Calibration algorithms for the amplitude and timing calibrations are also being developed.

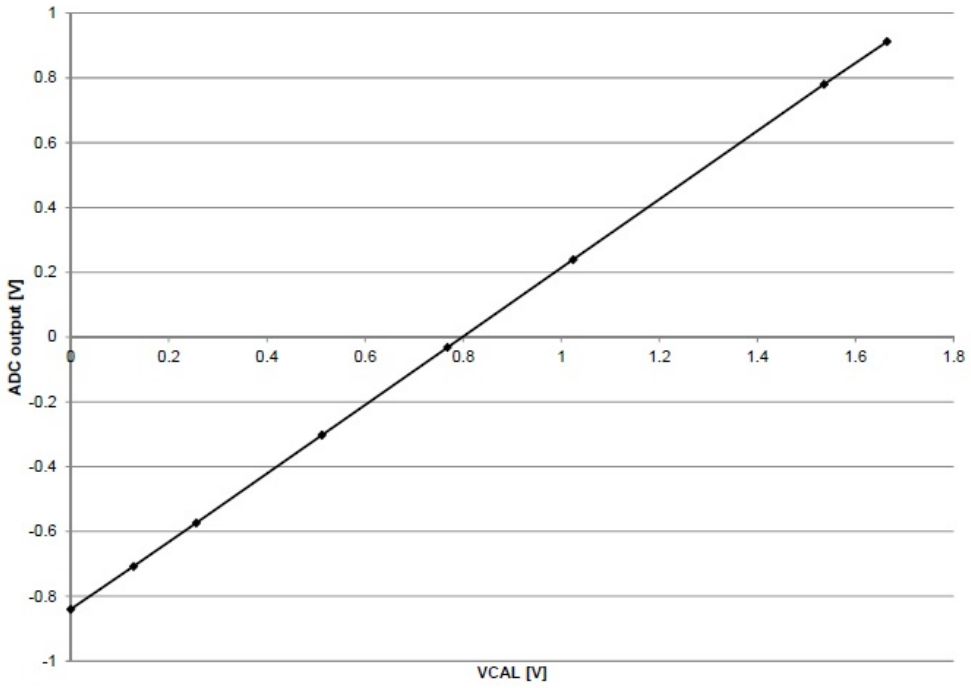

Figure 11: Linearity of the DRS digitizer for a channel picked up randomly.

4 Software and Calibration Modifications

Currently NA61/SHINE uses the old NA49 software framework for reconstruction, and simulations. The core of this "legacy" framework was developed in the early 1990s. It is written in different programming and scripting languages (C, pgi-Fortran, shell) and provides several concurrent data formats for event data model, which includes also obsolete parts. The new software framework, called SHINE is written in C++ and designed to comprise three principal parts: a collection of processing modules which can be assembled and sequenced by the user via XML files, an event data model which contains all simulation and reconstruction information based on STL and ROOT streaming, and a detector description which provides data on the configuration and state of experiment. Currently the NA61/SHINE uses the new framework SHINE for data analysis and quality assessments.

4.1 "Legacy" software maintenance

Over the last year, we assured maintenance of the "legacy" software. It is compiled using a dedicated 32-bit SLC5 Virtual Machine (VM) provided by CERN via the Cloud Infrastructure (`https://openstack.cern.ch`). The license for the required PGI Fortran compiler has been purchased by the Collaboration and is being maintained by CERN IT. The produced executables run successfully under the SLC6 operating system.

Two "legacy" software releases have been made since the time of the last Status Report in order to introduce required bug-fixes and updates. Given the progress with the new SHINE software framework, it was decided to minimize the "legacy" software support under SLC6 and to freeze its development.

Up to now, the "legacy" software is still routinely used within the collaboration to process raw data and to perform MC simulations.

4.2 NA61/SHINE IT infrastructure

The NA61/SHINE collaboration uses the CERN IT infrastructure as the main place to store, manage and analyze the data. The CERN CASTOR system serves as the main persistent storage of the data. The collaboration uses the EOS service to store data for the fast and easy access for physics analysis. Presently NA61/SHINE has allocated 400 TB (200 TB available for data storage) of space on the EOS service and around 75% of the space is already allocated by collaboration. The production and analysis processes use the CERN computing service (lxBatch). The CERN cloud infrastructure (CERN OpenStack) is used by NA61/SHINE as the main place where services are moved. The electronic logbook, bookkeeping, a new quality assessment system used the OpenStack virtual environment. Moreover the NA61/SHINE collaboration uses Jenkins (provided by CERN IT) as the application for software integrity checks. Since 2015 GitLab is a platform for the Git distributed version control system recommended by CERN hence the collaboration has started to migrate all repositories from SVN to the Git.

4.3 The deployment of the SHINE reconstruction within the production chain

NA61/SHINE entered into the final phase of the implementation of the new software in the production chain. All of the necessary steps were already reached. The new SHINE software was validated over the "legacy" production chain and is ready for deployment. The last necessary ingredient, Monte-Carlo simulation, was validated as well over the "legacy" reconstruction chain. The collaboration froze the "legacy" database and has started the process of data transformations to the new structures required by the SHINE production chain and it will be finished in the near future. Because the SHINE software still inherits some functions, modules and structures from the "legacy" reconstruction, the development of new modules is ongoing.

4.4 Native SHINE software

4.4.1 Monte Carlo simulation status and development

The native SHINE Monte Carlo simulation consists of major two steps; a GEANT 4 based detector description to simulate the passage of particles through detectors and a digitization simulation to simulate the detector responses.

A GEANT 4 based detector description in SHINE (Luminance) is fully implemented including the new sub-systems (F-TPCs and Vertex Detector). Its optimization is under progress, which is important to minimize CPU process time and event size without losing necessary precision. The Luminance will replace the outdated "legacy" GEANT 3 based simulation.

The Luminance outputs are then fed into the digitization process which simulates the detector response and outputs raw detector simulated signals. The "legacy" code calculating the drift of charge clouds in the TPCs has been re-written in SHINE with improved maintainability and precision. Validations toward the "legacy" digitization process have been done (see an example in Fig. 12) and validations toward the data are ongoing.

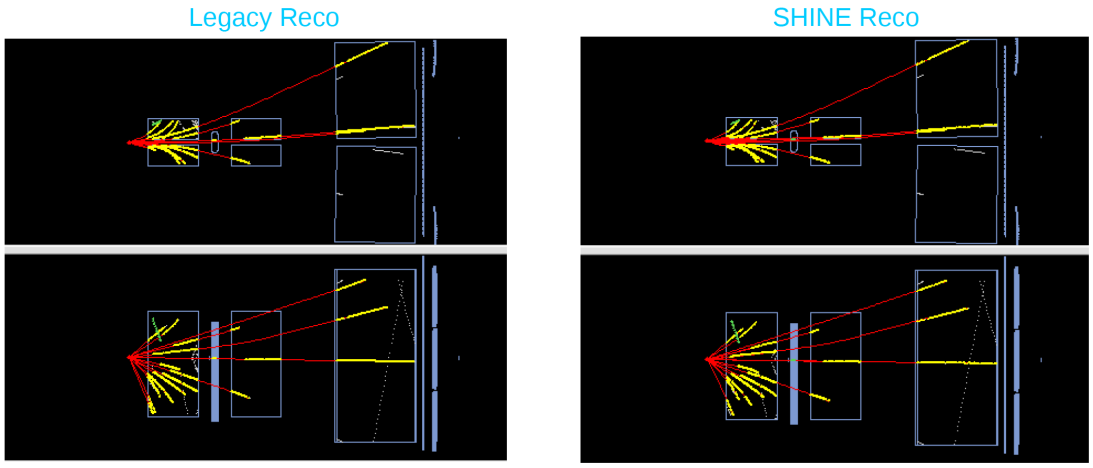

Figure 12: A comparison using a same p+C event with "legacy" MC simulation (left) and SHINE MC simulation (right). For the track reconstruction, the "legacy" reconstruction in SHINE is used for the both cases.

To sort out every problems within the newly developed MC simulation, full MC chain studies have started using Pb+Pb collisions, as these collisions are supposes to have the largest multiplicity of secondary particles produced on the target under the NA61/SHINE physics programs.

4.4.2 SHINE reconstruction

Global track reconstruction in SHINE is under development, which will replace current "legacy" software reconstruction and will include new detectors: F-TPC and VD. The Kalman Filter algorithm has been implemented in SHINE framework and it is validated using large statistics of data. Bridging of local track segments from different TPCs, which forms global tracks, is under development.

4.5 SHINE calibration

The report briefly presents the status and plans for the ongoing implementation of new calibration software modules based on the SHINE off-line framework and the SHOE data format. The existing NA61/SHINE calibration chain consists of software modules and tools which are implemented in different programming languages such as Fortran and C as well as linux shell scripts. The SHINE off-line framework is entirely written in C++ and is used for data analysis. Thus the entire calibration chain is going to be updated by new software modules within the new framework.

The following sections describe the progress of the ongoing software implementations, current status and the future plans.

4.5.1 ToF Left/Right Calibration Software

The main goal is to write an automated and more efficient ToF L/R calibration procedure which uses data in SHOE format and information from NA61/SHINE DB working under the SHINE framework. The group of developers is expecting a faster calibration software which will provide more precise calibration constants.

The first version of the module still working with data in old NA49/NA61/SHINE DSPACK format has been tested. The final version of the module will read SHOE data as the input. The old format existing calibration constants will be transferred to the new data format. The group will write a new calibration procedure to be included in the improved new ToF data calibration process. This new calibration procedure is currently under development. The new calibration procedure will be released and later validated by the comparison of new calibration results with those obtained by the old procedure. The group is expecting improved time resolution. The work is in progress and it is planned to be finished at the end of 2016.

4.5.2 Drift Velocity (vD-PA) Calibration Module

The vD-PA calibration module provides the TPC calibration parameters namely the drift velocity, global time offset and detector time offset for each chamber and vertical shift of each chamber. The module presently being processed for different data samples. The module has been tested for small statistics using low multiplicity p+p events and the tests will be carried out for large statistical samples. The extended tests will continue with the data set from the 2015: Pb+Pb collisions at 30 GeV/c recorded without the magnetic field.

4.5.3 GAP TPC vD Calibration Module

This module produces the drift velocity calibration constants by testing the track alignment of GAP-TPC to VTPC-2 local tracks. In the current implementation the straight line extrapolation of tracks is used but in the final version we plan to use the Kalman

filter in magnetic field. The module reads NA61/SHINE data in SHOE format. The software has been updated to be user friendly and automated. The module has already been tested for few data samples. The software was tested in detail for p+Pb collisions at 158GeV/c beam momentum. The current activity is concentrated on the implementation of Kalman filter in the module and the advanced validation of the new software.

5 New Results

5.1 New results for physics of strong interactions

This section summarizes new physics results from the programme on physics of strong interactions.

Inclusive spectra of negatively charged pions produced in central Ar+Sc collisions at 13A-150A GeV/c are presented. The current version of the *kink* plot is shown. We also show preliminary results on Λ-hyperon spectra in inelastic p+p interactions at 40 GeV/c and compare them with the world data.

The new results on transverse momentum and multiplicity fluctuations in Ar+Sc collisions at 13A-150A GeV/c are shown. The Ar+Sc results are compared to NA61/SHINE p+p and Be+Be data, as well as to NA49 $A+A$ results. Moreover, the latest results on higher order moments of net-charge multiplicity distribution in p+p interactions are also discussed.

Finally, we present the preliminary results on the inelastic and production cross-section of ^{7}Be on ^{9}Be and we discuss the method and its performance of anisotropic flow analysis in Pb+Pb collisions.

5.1.1 π^- spectra and mean multiplicity in Ar+Sc

The spectra of π^- in collisions of Ar+Sc at 13A-150A GeV/c were obtained using the so-called h^- analysis method assuming that the majority of negatively charged particles are π^- mesons. The contribution ($\approx$ 10%) of other particles (K^-, $\overline{p}$) is subtracted using EPOS1.99. We obtained precise large statistics results in full p_T and wide rapidity range in the whole SPS beam momentum range. The results are corrected for particles from weak decays (feed-down) and the detector effects using MC simulations. Out-of-target interactions are subtracted using events recorded with removed target. Examples of double differential spectra of negatively charged pions in rapidity and transverse momentum for the most central [1] Ar+Sc interactions are presented in Fig. 13.

Examples of preliminary m_{T} spectra of π^- mesons in central Ar+Sc collisions are shown in Fig. 14 and compared to the corresponding spectra in p+p interactions [9], preliminary NA61/SHINE Be+Be data, and NA49 Pb+Pb results [10,11]. The shape of Ar+Sc m_{T} spectra is similar to the one measured in central Pb+Pb collisions, but it differs

[1] NA61/SHINE selects central $A+A$ collisions using the Projectile Spectator Detector located on the beam axis. It measures the forward energy related to the non-interacting nucleons of the beam nucleus.

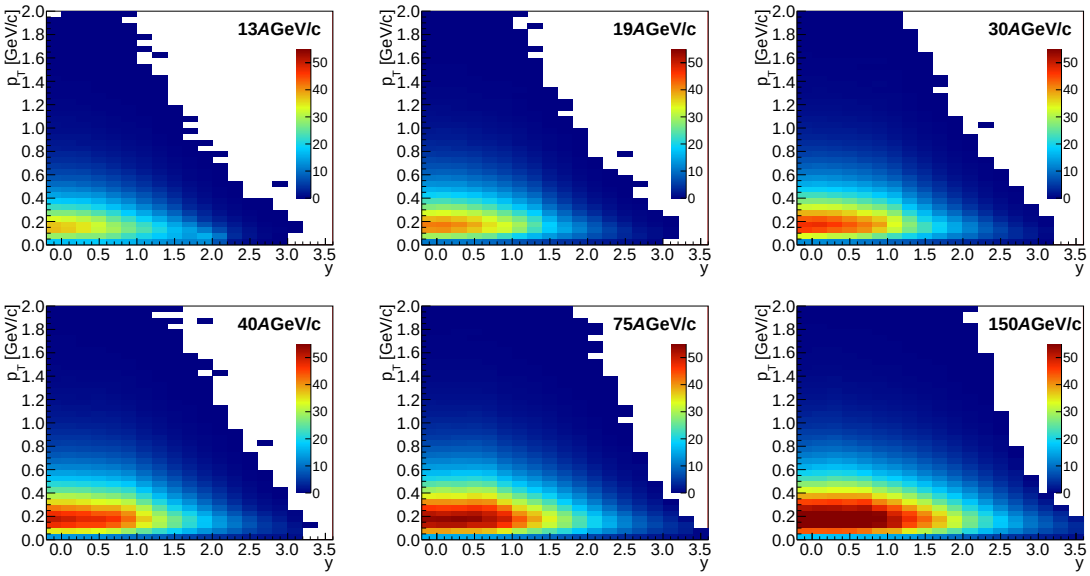

Figure 13: $d^2n/(dp_Tdy)$ spectra of π^- mesons in 0-5% central Ar+Sc collisions at 13A-150A GeV/c.

from the shape measured in p+p interactions, which may originate from isospin effects, collective flow, changing role of resonance production.

The data extracted using the h^- method is used to calculate mean pion multiplicities in the full phase-space. $\frac{dn}{dydp_T}$ spectra are extrapolated in transverse momentum p_T and rapidity y. The process consists of the following four steps:

1. Extrapolation in p_T– for a given y bin extrapolate p_T spectrum to p_T = 2 GeV/c, using the exponential form $f(p_T) = C \cdot p_T \cdot \exp\left(-\sqrt{p_T^2 + m^2}/T\right)$,

2. Integration of the p_T extrapolated $\frac{dn}{dydp_T}$ spectrum,

3. Fitting sum of two Gaussian functions – reflects separate contribution to the spectrum from the target and projectile nucleons. The Gaussians take form of

$$g(y) = g_T(y) + g_P(y)$$

$$g_T(y) = \frac{A_0 A_{rel}}{\sigma\sqrt{2\pi}} \exp\left(-\frac{(y-y_0)^2}{2\sigma}\right)$$

$$g_P(y) = \frac{A_0}{\sigma\sqrt{2\pi}} \exp\left(-\frac{(y+y_0)^2}{2\sigma}\right)$$

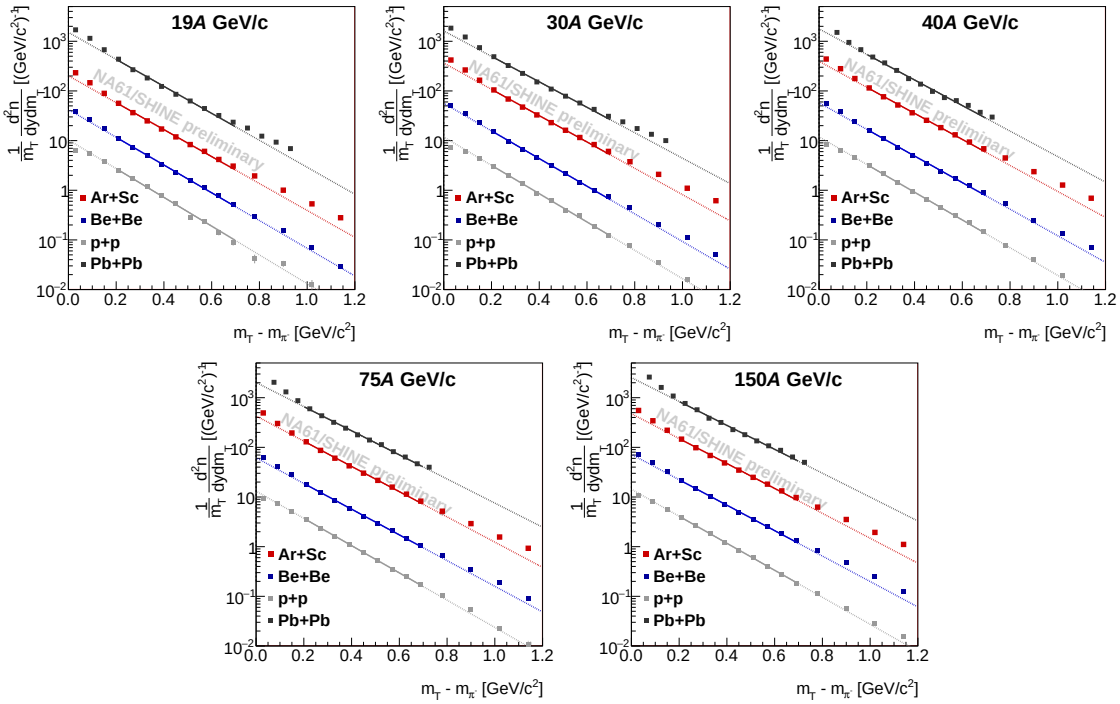

Figure 14: Transverse mass spectra of π^- mesons in 0-5% Ar+Sc collisions. The m_{T} spectra are compared to NA49 Pb+Pb [10, 11] and NA61/SHINE p+p [9] and Be+Be results. Note: p+p and Pb+Pb collisions were taken at 158A GeV/c beam momenta.

4. Mean π^- multiplicity is calculated as the sum of measured data and extrapolated Gaussian functions

$$\langle \pi^- \rangle = \int_{-4}^{y_{\mathrm{min}}} g(y)dy + \sum_{y_{\mathrm{min}}}^{y_{\mathrm{max}}} dy \left(\frac{dn}{dy}\right)_{\text{extrapolated in} p_{\mathrm{T}}} + \int_{y_{\mathrm{max}}}^{4} g(y)dy$$

The process is presented in Fig. 15. The corresponding p_{T}-extrapolated and p_{T}-integrated rapidity spectra of π^- mesons are shown in Fig. 16. One sees that the spectra extend below mid-rapidity.

Statistical uncertainties $\sigma_{\mathrm{stat}}(\langle \pi^- \rangle)$ are propagated from the statistical uncertainties of $\frac{dn}{dydp_{\mathrm{T}}}$ spectra. Systematic uncertainties $\sigma_{\mathrm{sys}}(\langle \pi^- \rangle)$ are assumed to be 5% based on previous NA61/SHINE analysis [9]. The procedure leads to the results presented in Table 3.

Statistical uncertainty is negligible comparing to the systematic one. The former is smaller than the bin size, therefore the total error calculated as $\sqrt{\sigma_{\mathrm{sys}}^2 + \sigma_{\mathrm{stat}}^2}$ will be presented.

In order to compare resulting multiplicities for Ar+Sc with other systems, it is necessary to normalize the results to mean number of wounded nucleons $\langle W \rangle$. The analysis of mean number of wounded nucleons was performed using two Monte Carlo models:

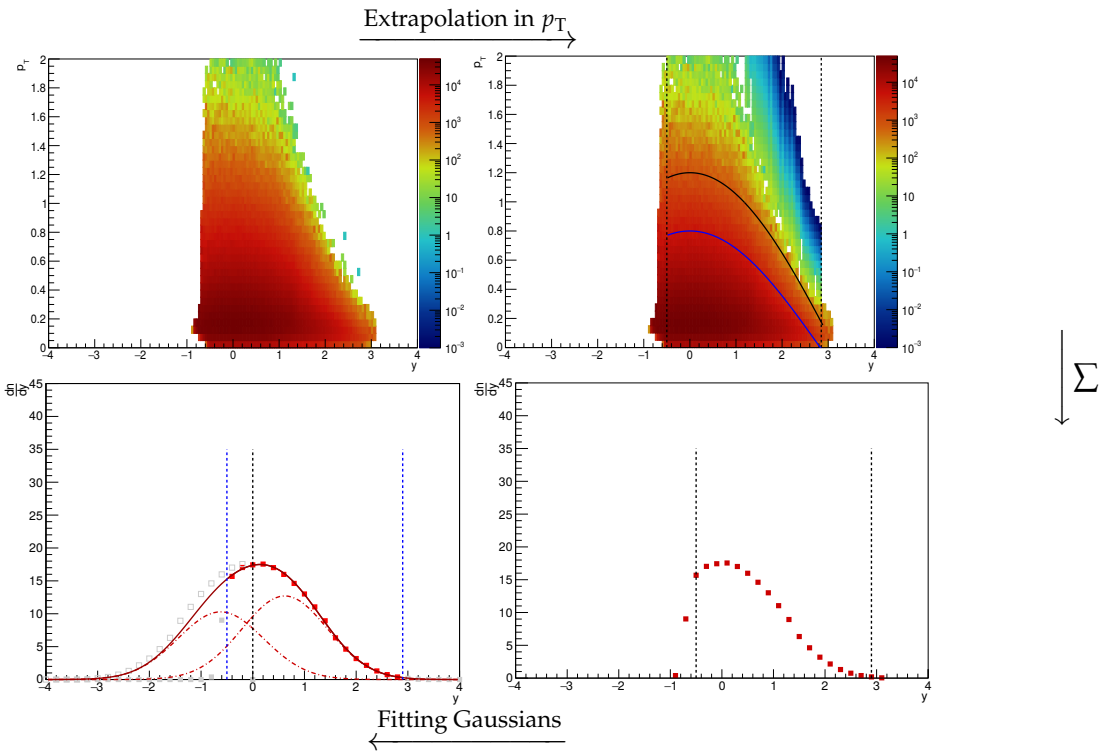

Figure 15: Schematic overview of the $\frac{dn}{dydp_T}$ spectrum extrapolation process.

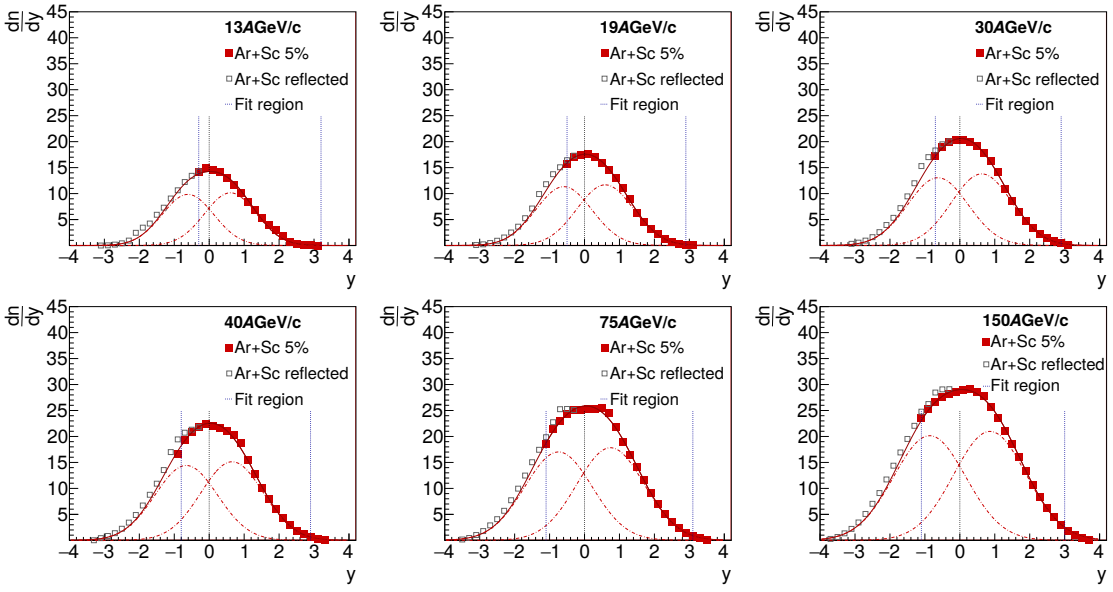

Figure 16: Rapidity spectra of π^- mesons produced in 0-5% Ar+Sc collisions.

- GLISSANDO 2.73 [12]
- EPOS1.99 (version CRMC1.5.3) [13]

Momentum [A GeV/c]	13	19	30	40	75	150
$\langle\pi^-\rangle$	38.46	48.03	59.72	66.28	86.12	108.92
$\sigma_{\text{stat}}(\langle\pi^-\rangle)$	$\pm$0.021	$\pm$0.021	$\pm$0.024	$\pm$0.018	$\pm$0.0079	$\pm$0.0088
$\sigma_{\text{sys}}(\langle\pi^-\rangle)$	$\pm$1.92	$\pm$2.40	$\pm$2.98	$\pm$3.31	$\pm$4.30	$\pm$5.44

Table 3: Mean multiplicity of negatively charged pions produced in 0-5% Ar+Sc collisions at 13A-150A GeV/c.

Momentum [A GeV/c]	13	19	30	40	75	150
$\langle W\rangle_{\text{EPOS}}$	50.63	54.68	58.44	59.01	61.12	63.04
$\langle W\rangle_{\text{GLISSANDO}}$	67.44	68.85	68.98	69.01	68.87	69.18

Table 4: Number of wounded nucleons $\langle W\rangle$ calculated using EPOS and Glissando.

GLISSANDO MC is based on Glauber model, whereas EPOS utilizes parton ladder model. Uncertainties of $\langle W\rangle$ will not be presented and in both cases the resulting $\langle W\rangle$ is calculated for 5% centrality. The differences between the $\langle W\rangle$ value calculated using the models are significant, as presented in the Table 4. For lower momenta EPOS gives much smaller values than GLISSANDO. This discrepancy is a starting point for a broader investigation within the framework of the NA61/SHINE experiment. In order to obtain a more reliable value, an extended collaboration with theoretical groups has been initiated. For the sake of comparison and consistency with previously calculated values, we will use the $\langle W\rangle$ calculated using GLISSANDO. As a result, one can obtain the $\langle\pi^-\rangle/\langle W\rangle$ ratio for all the measured energies (see Table 5).

Momentum [A GeV/c]	$\langle\pi^-\rangle$	$\langle W\rangle_{\text{GLISSANDO}}$	$\langle\pi^-\rangle/\langle W\rangle$
13	38.46	67.44	0.57 ± 0.028
19	48.03	68.85	0.69 ± 0.034
30	59.72	68.98	0.86 ± 0.043
40	66.28	69.01	0.96 ± 0.047
75	86.12	68.87	1.25 ± 0.062
150	108.92	69.18	1.57 ± 0.078

Table 5: $\langle\pi^-\rangle/\langle W\rangle$ ratio in central Ar+Sc collisions.

In order to compare results obtained for different systems, the isospin correction should be taken into account. To this end, phenomenological formulas are used

$$\langle\pi^-\rangle_{\text{N+N}} = \langle\pi^-\rangle_{\text{p+p}} + 1/3$$

$$\langle\pi^-\rangle^{\text{I}}_{\text{Au+Au}} = (\langle\pi^-\rangle_{\text{Au+Au}} + \langle\pi^+\rangle_{\text{Au+Au}})/2$$

It is based on the compilation of the world data presented in Ref. [14] and the model presented therein. The correction is only applied to measurements where its effect is significant. Figure 17 shows the comparison of $\langle\pi^-\rangle/\langle W\rangle$ ratio for Ar+Sc collisions with

corresponding results for other reactions at different energies. Data suggest a monotonic increase of the ratio with $\langle W \rangle$ at 150A GeV/c. Non-monotonic behaviour at lower beam momenta is observed. It is probably caused by a larger uncertainty of $\langle W \rangle$.

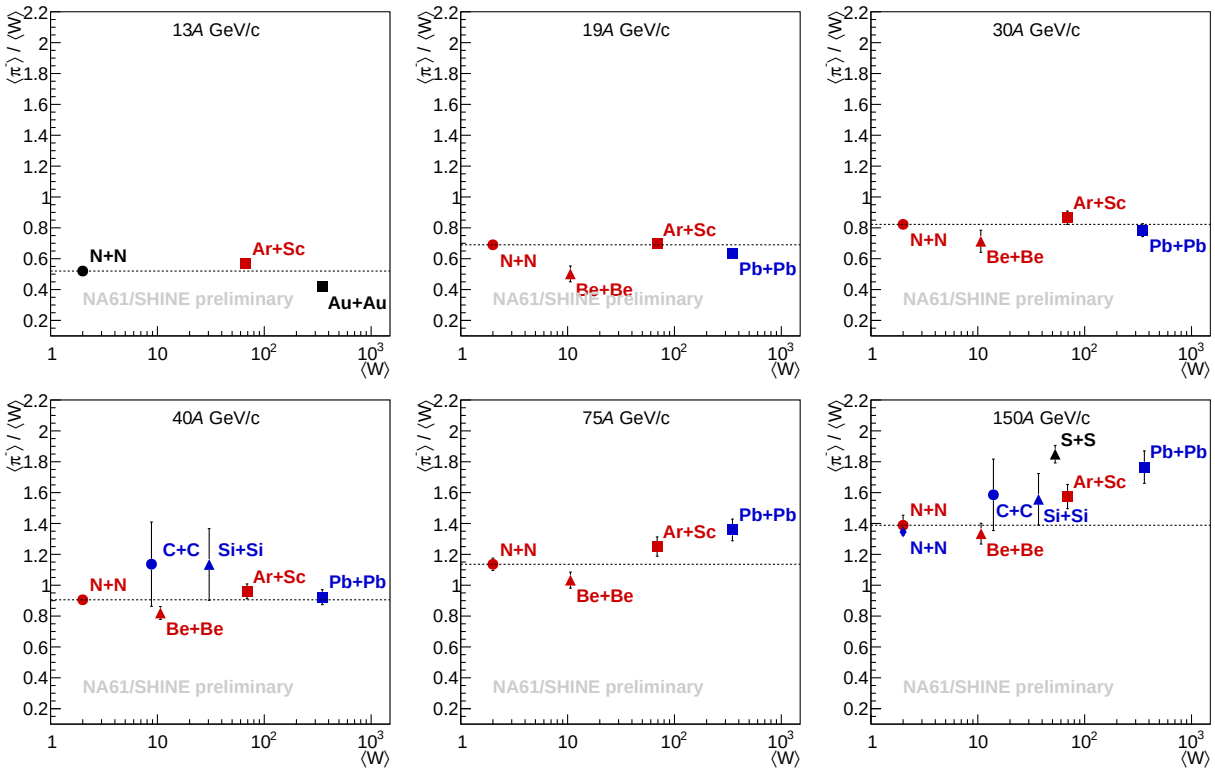

Figure 17: Comparison of $\langle \pi^- \rangle / \langle W \rangle$ ratio.

The $\langle \pi \rangle / \langle W \rangle$ is also plotted [2] against the Fermi collisions energy measure F. Figure 18 shows that mean π multiplicity per wounded nucleon increases faster with F at the SPS energies in central Pb+Pb than in p+p collisions (*kink*). The two dependences cross at about 40A GeV/c ($\sqrt{s_{NN}} = 8.77$ GeV, $F = 2.47$ GeV$^{1/2}$). For high SPS energies Ar+Sc follows the Pb+Pb trend and for low SPS energies Ar+Sc follows the p+p tendency. The situation is opposite for Be+Be collisions. One should remember that the results suffer from a significant model dependence of mean number of wounded nucleons.

5.1.2 Inelastic and production cross-section of ^{7}Be on ^{9}Be

Preliminary NA61/SHINE results on the inelastic and production cross-section of ^{7}Be on ^{9}Be are presented in Fig. 19. Inelastic cross-section (projectile nucleus charge change cross-section) and production cross section (cross section for production of at least one

[2] As for Ar+Sc, Be+Be and p+p data we only have the $\langle \pi^- \rangle$ value, we use following approximations: $\langle \pi \rangle_{\text{p+p}} = 3\langle \pi^- \rangle_{\text{p+p}} + 1$, $\langle \pi \rangle_{\text{Ar+Sc}} = 3\langle \pi^- \rangle_{\text{Ar+Sc}}$, $\langle \pi \rangle_{\text{Be+Be}} = 3\langle \pi^- \rangle_{\text{Be+Be}}$.

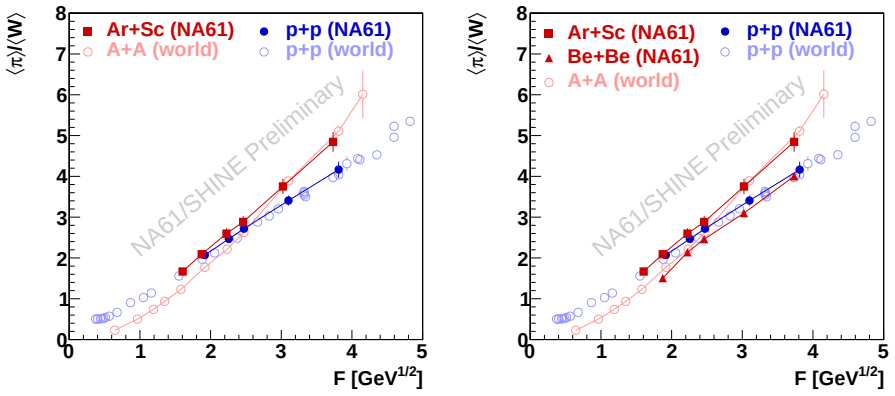

Figure 18: *Kink* plots: mean pion multiplicity divided by mean number of wounded nucleons as a function of Fermi collision energy measure F [15] ($F \simeq s_{NN}^{1/4}$).

new particle) are shown as a function of beam momentum. Values measured by NA61/SHINE are in good agreement with earlier measurement at lower momentum [16], as well as with predictions of the Glauber-based GLISSANDO model [12]. The NA61/SHINE measurements together with $\sim 1A$ GeV Bevalac data establish the energy dependence of the inelastic cross section from $1A$ GeV to $150A$ GeV.

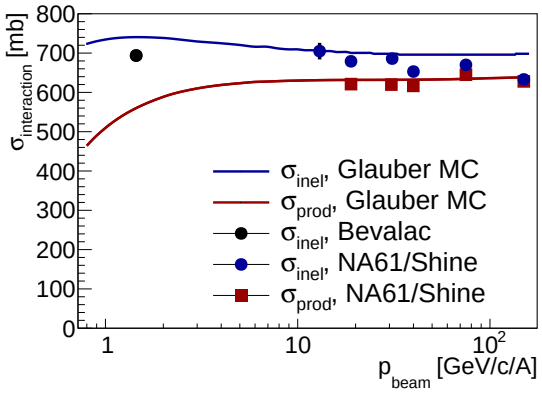

Figure 19: Inelastic and production cross-section of ^{7}Be on ^{9}Be as a function of beam momentum.

5.1.3 Λ production in p+p at 40 GeV/c

Preliminary results on Λ hyperon production in inelastic p+p interactions at 40 GeV/c are presented here. In the following, Λ denotes Λ hyperons produced via strong processes, as well as those from the electromagnetic Σ^0 decay, $\Sigma^0 \rightarrow \Lambda\gamma$ (branching ratio 100%).

Λ hyperons were identified by their charge decay channel $\Lambda \rightarrow p + \pi^-$ (branching ratio 63.9%) which has a characteristic V^0 topology. The candidates were searched for by forming pairs from all measured positively and negatively charged particles and requiring a distance of closest approach between the two trajectories of less than 1 cm at any point between the position of the first measured points on the tracks and the primary vertex. For each candidate the invariant mass was calculated assuming proton (pion) mass for positively (negatively) charged particles. To ensure a good momentum determination and reduce the combinatorial background from random pairs, a set of quality cuts was imposed. The raw number of Λ hyperons was extracted by fitting the invariant mass distributions by a sum of Lorentzian (signal) and a polynomial (background). The $p\ \pi^-$ invariant mass distribution for Λ candidates in the range $y \in [0.25, 0.50]$ and $p_{\mathrm{T}} \in [0.2, 0.4]$ GeV/c, together with the result of the fit is shown in Fig. 20. The position of Λ peak is in the agreement with the nominal value of the Λ mass, m_Λ = 1.115683 $\pm$ 0.000006 GeV/c^2 [17], indicated by the blue dashed line.

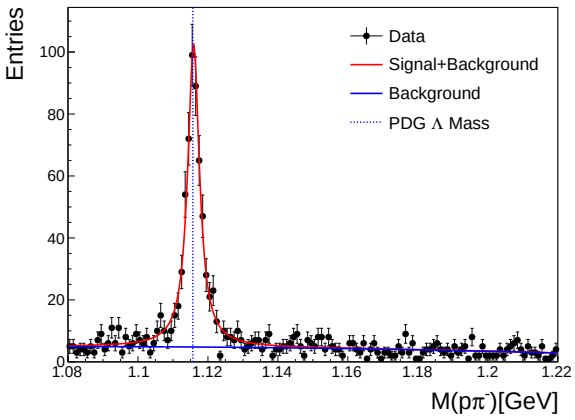

Figure 20: The $p\ \pi^-$ invariant mass distribution of Λ candidates in the range $y \in [0.25, 0.50]$ and $p_{\mathrm{T}} \in [0.2, 0.4]$ GeV/c. The red solid line shows a fit to signal plus background, while the blue solid line represents the background contribution. The Λ hyperon PDG mass is indicated by a blue dashed line.

Using the standard NA61/SHINE simulation and reconstruction chain, the raw number of Λ hyperons extracted in different $y(x_F) - p_{\mathrm{T}}$ bins was corrected for geometrical acceptance, reconstruction efficiency, the feed-down from secondary interactions and weak decays as well as for the losses due to the quality cuts, the trigger bias and the branching ratio. The preliminary double-differential $\frac{d^2n}{dydp_T}$ and $\frac{d^2n}{dx_Fdp_T}$ distributions are shown in Figs. 21 and 22, respectively. They are fitted by the function

$$f = \frac{d^2n}{dkdp_T} = A \cdot p_T \cdot e^{-\frac{\sqrt{m_\Lambda^2 + p_T^2}}{T}}, \tag{1}$$

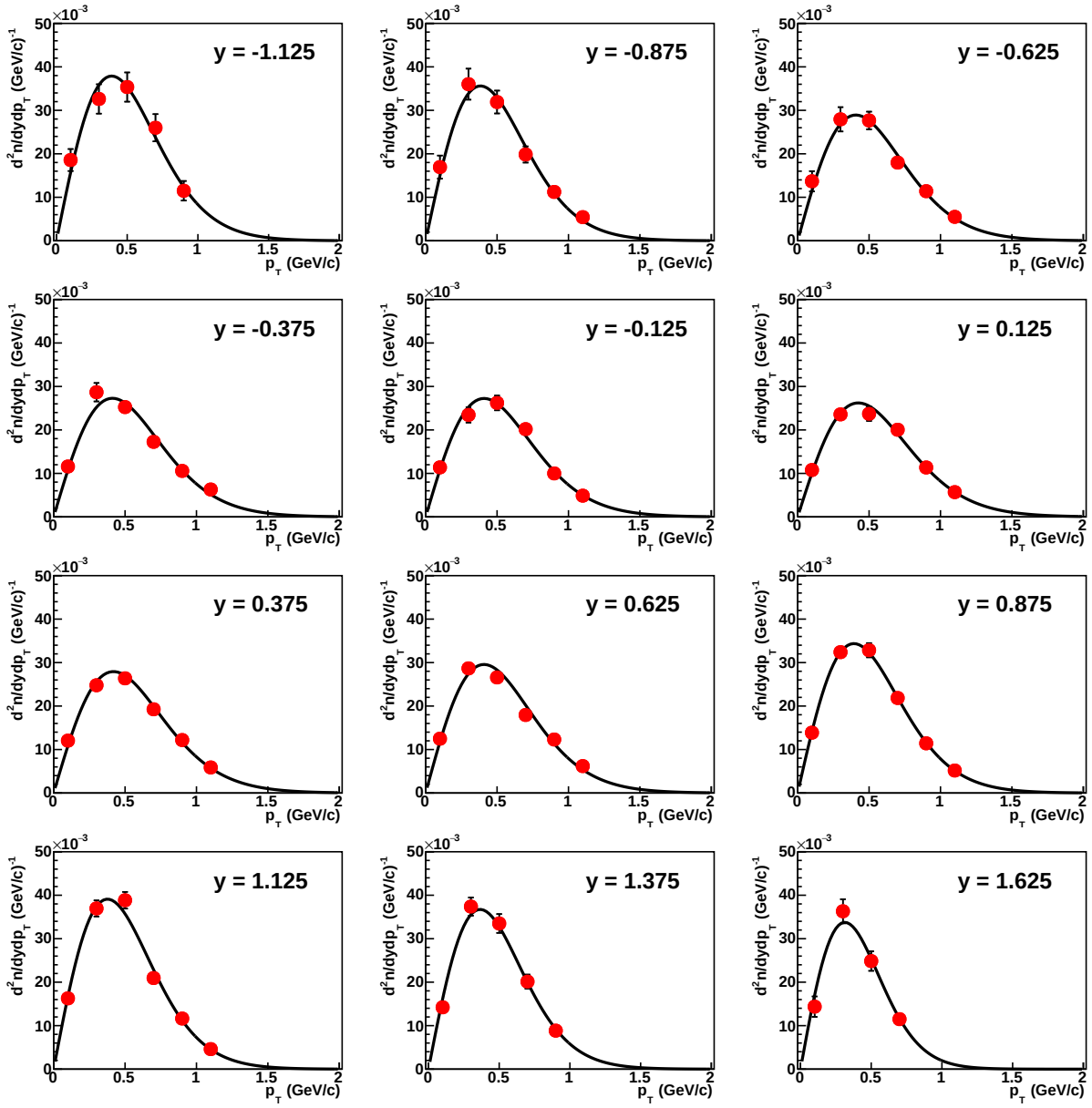

Figure 21: Double-differential $\frac{d^2n}{dydp_T}$ distributions of Λ hyperons produced in inelastic p+p interactions at 40 GeV/c. The fitted function is given by Eq. 1.

where $k = y, x_F$, A is the normalisation factor and T the inverse slope parameter. The extracted values of the inverse slope parameter T are presented in Fig. 23 and compared to the NA61/SHINE p+p results at 158 GeV/c [18].

Single-differential $\frac{dn}{dy}$ and $\frac{dn}{dx_F}$ distributions were obtained by summing up the double-differential yields over the p_{T} bins at fixed y and x_F and correcting the sum for the missing acceptance using the function Eq. 1. The obtained $\frac{dn}{dy}$ and $\frac{dn}{dx_F}$ distributions, to-

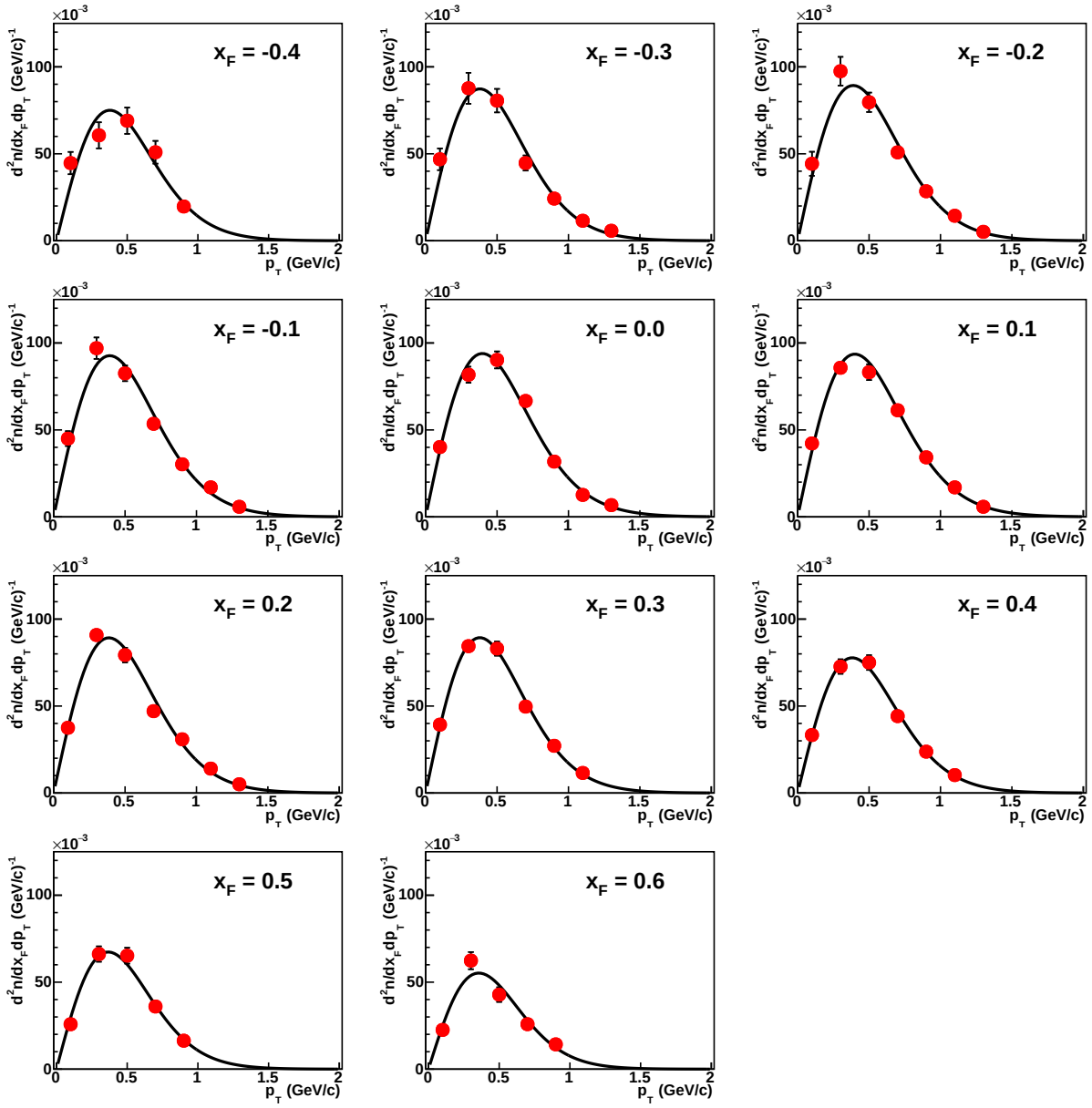

Figure 22: Double-differential $\frac{d^2n}{dx_F dp_T}$ distributions for Λ hyperons produced in inelastic p+p interactions at 40 GeV/c. The fitted function is given by Eq. 1.

gether with the predictions from EPOS1.99 [13], URQMD1.3.1 [22, 23] and Fritiof [24] embedded in HSD [25] model are presented in Fig. 24. The $\frac{dn}{dy}$ distribution obtained by averaging Λ yield in corresponding forward and backward rapidity bins is compared in Fig. 25 with the data from two bubble-chamber experiments performed at beam momentum 24 GeV/c [19] and 69 GeV/c [20].

Mean multiplicity of Λ hyperons ($\langle\Lambda\rangle$) was determined from the x_F distribution. The

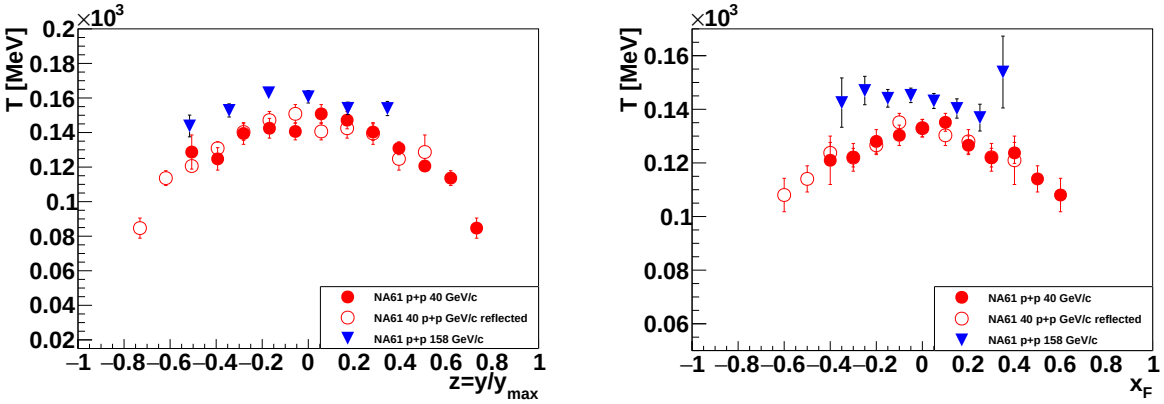

Figure 23: The inverse slope parameter as a function of scaled rapidity variable $z = y/y_{max}$ (left) and x_F (right) for Λ hyperons produced in inelastic p+p interactions at 40 (red) and 158 GeV/c (blue).

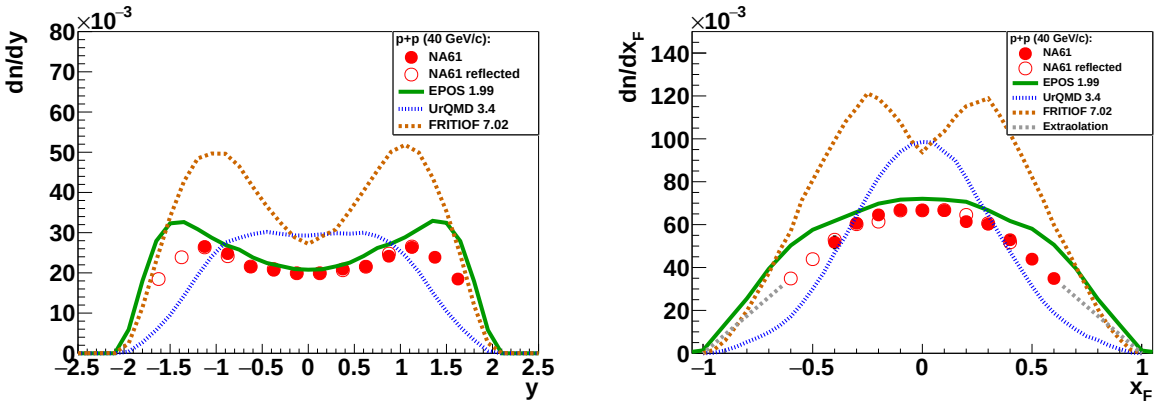

Figure 24: Single-differential $\frac{dn}{dy}$ (left) and $\frac{dn}{dx_F}$ (right) distributions for Λ hyperons produced in inelastic p+p interactions at 40 GeV/c, together with the predictions from EPOS, URQMD and Fritiof models.

Λ yield in the unmeasured x_F region was approximated by the straight line shown in Fig. 24 and amounts to 13% of the total Λ yield which is estimated to be $\langle\Lambda\rangle = 0.0816 \pm 0.0009$. The mean multiplicity of Λ hyperons in 40 GeV/c inelastic p+p interactions is compared in Fig. 26 with the world data [21] as well as with the NA61/SHINE p+p results at 158 GeV/c and the predictions of the EPOS1.99 model.

In order to validate the analysis procedure and detect possible biases the fully corrected lifetime distribution of Λ hyperons is determined and fitted with the exponential function. An example of the lifetime distribution is shown in Fig 27 (left). The ratio of the fitted mean lifetime $c\tau$ to the corresponding PDG value $c\tau_{PDG} = 7.89$ cm [17] is shown in Fig. 27 (right) as a function of rapidity. The fitted mean lifetimes agree with the PDG value indicating correctness of the analysis procedure.

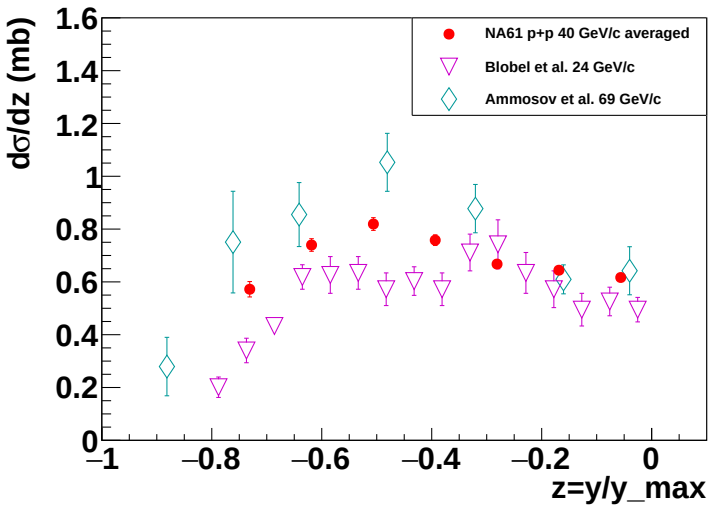

Figure 25: Comparison of average rapidity distribution from the NA61/SHINE with the data from two bubble-chamber experiments performed at beam momentum 24 GeV/*c* [19] and 69 GeV/*c* [20].

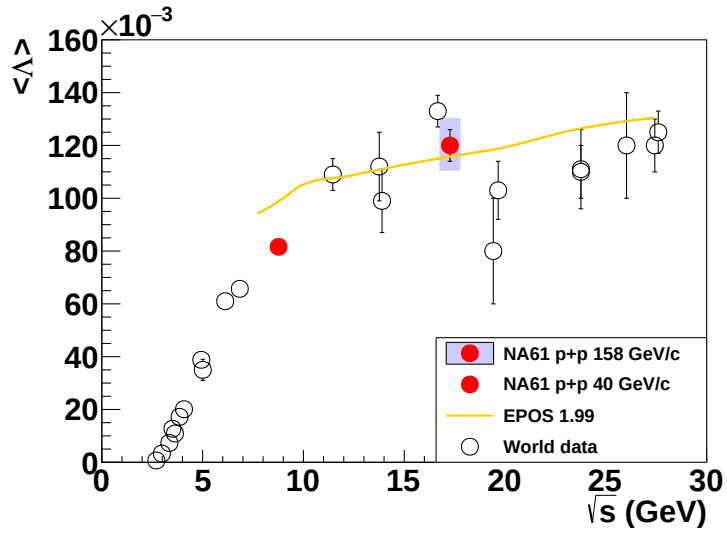

Figure 26: Mean multiplicity of Λ hyperons produced in inelastic p+p interactions as a function of collision energy. The NA61/SHINE results at 40 and 158 GeV/*c* are indicated by the closed point. Word data are taken from Ref. [21].

5.1.4 Transverse momentum and multiplicity fluctuations in Ar+Sc, Be+Be and inelastic p+p

The strategy of looking for the critical point (CP) of strongly interacting matter is based on a search for non-monotonic behaviour of CP signatures such as fluctuations of trans-

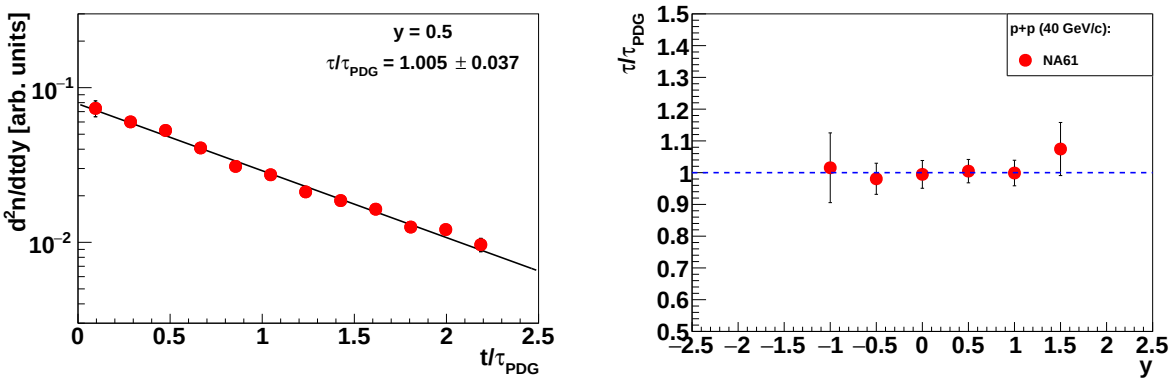

Figure 27: An example of the corrected proper lifetime distribution for Λ hyperons produced in inelastic p+p interactions at 40 GeV/c in the rapidity interval $y = 0.5 \pm 0.25$ (left). The ratio of the fitted mean lifetime to its PDG [17] value as a function of rapidity.

verse momentum, multiplicity, intermittency, etc. when the system freezes out close to the CP. NA61/SHINE uses the strongly intensive $\Delta[P_{\mathrm{T}}, N]$, $\Sigma[P_{\mathrm{T}}, N]$, and $\Phi_{p_{\mathrm{T}}}$ measures to study transverse momentum and multiplicity fluctuations [26,27]. For the Boltzmann ideal gas of particles in the Grand Canonical Ensemble they do not depend on volume and volume fluctuations. Moreover, $\Delta[P_{\mathrm{T}}, N]$ and $\Sigma[P_{\mathrm{T}}, N]$ have two reference values, namely they are equal to zero in case of no fluctuations and one in case of independent particle production. The recent NA61/SHINE results [27] show no sign of any anomaly, that can be attributed to a CP, neither in p+p nor centrality selected Be+Be collisions. On the other hand a maximum for Si+Si and C+C was observed by NA49 in transverse momentum and multiplicity fluctuations at 158A GeV/c (see Refs. [27, 28] and references therein).

Figure 28 shows preliminary NA61/SHINE results on transverse momentum and multiplicity fluctuations in p+p, Be+Be, and Ar+Sc collisions (note that p+p and Be+Be results were already shown by NA61/SHINE [26, 27] but in a slightly different acceptance). These three systems show no prominent non-monotonic behaviour that can be attributed to a CP. The same measurements presented in two-dimensional plots (mean number of wounded nucleons $\langle W \rangle$ from Ref. [12]) without statistical uncertainties are shown in Figs. 29 and 30. The values of $\Delta[P_{\mathrm{T}}, N]$ smaller than 1 and $\Sigma[P_{\mathrm{T}}, N]$ higher than 1 may be due to Bose-Einstein statistics and/or anti-correlation between event transverse momentum and multiplicity [29]. The $\Sigma[P_{\mathrm{T}}, N]$ values for h^- at 150/158A GeV/c are higher in Ar+Sc than in Be+Be and p+p, but this increase is seen also at lower energies so it is not necessarily connected with a CP.

Figure 31 (left and middle) shows that NA49 Pb+Pb [28] and NA61/SHINE Ar+Sc results (in NA49 narrower acceptance [28]) are similar. For the system size dependence of $\Sigma[P_{\mathrm{T}}, N]$ at 150/158A GeV/c (Fig. 31, right) the NA49 [28] and NA61/SHINE points show consistent trends. $\Delta[P_{\mathrm{T}}, N]$ (not shown) is more centrality width sensitive [29] and

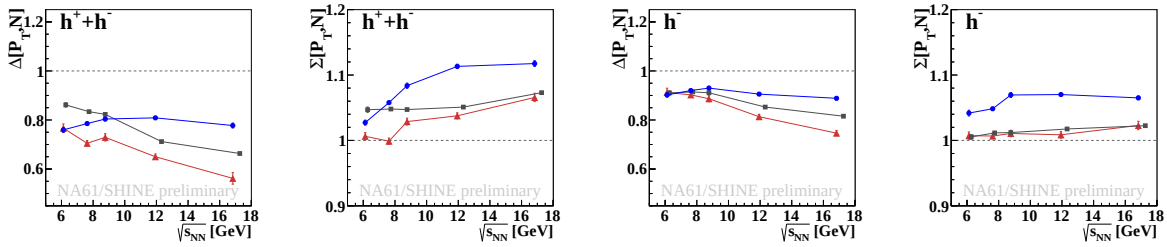

Figure 28: $\Delta[P_{\mathrm{T}}, N]$ and $\Sigma[P_{\mathrm{T}}, N]$ in inelastic p+p (grey squares), 0-5% Be+Be (red triangles), and 0-5% Ar+Sc (blue circles) collisions obtained by NA61/SHINE at forward-rapidity, $0 < y_{\pi} < y_{beam}$, and in $p_{\mathrm{T}} < 1.5$ GeV/c. Results for all charged hadrons ($h^+ + h^-$, left plots) and negatively charged ones (h^-, right plots).

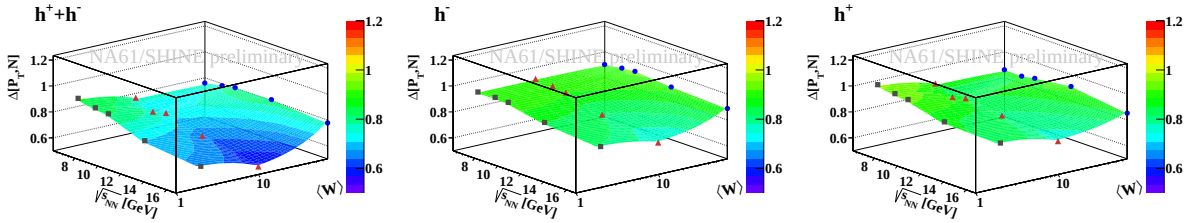

Figure 29: $\Delta[P_{\mathrm{T}}, N]$ in inelastic p+p (grey squares), 0-5% Be+Be (red triangles), and 0-5% Ar+Sc (blue circles) collisions obtained by NA61/SHINE at forward-rapidity, $0 < y_{\pi} < y_{beam}$, and in $p_{\mathrm{T}} < 1.5$ GeV/c. Results for all charged hadrons ($h^+ + h^-$, left), negatively charged ones (h^-, middle) and positively charged ones (h^+, right).

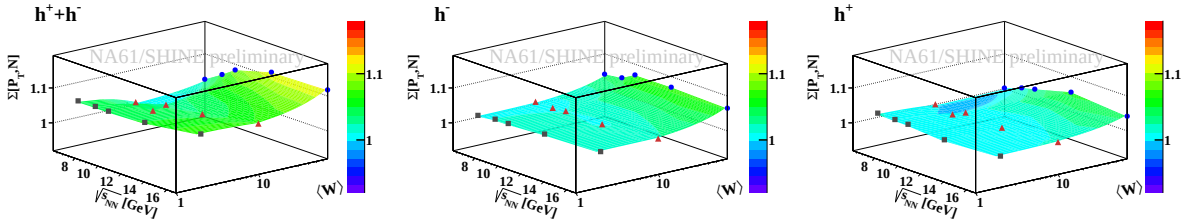

Figure 30: $\Sigma[P_{\mathrm{T}}, N]$ in inelastic p+p (grey squares), 0-5% Be+Be (red triangles), and 0-5% Ar+Sc (blue circles) collisions obtained by NA61/SHINE at forward-rapidity, $0 < y_{\pi} < y_{beam}$, and in $p_{\mathrm{T}} < 1.5$ GeV/c. Results for all charged hadrons ($h^+ + h^-$, left), negatively charged ones (h^-, middle) and positively charged ones (h^+, right).

points are scattered.

5.1.5 Multiplicity and forward energy fluctuations in Ar+Sc

The new NA61/SHINE results on multiplicity fluctuations in Ar+Sc collisions were obtained using the scaled variance of the multiplicity distribution ($\omega[N]$) and a newly

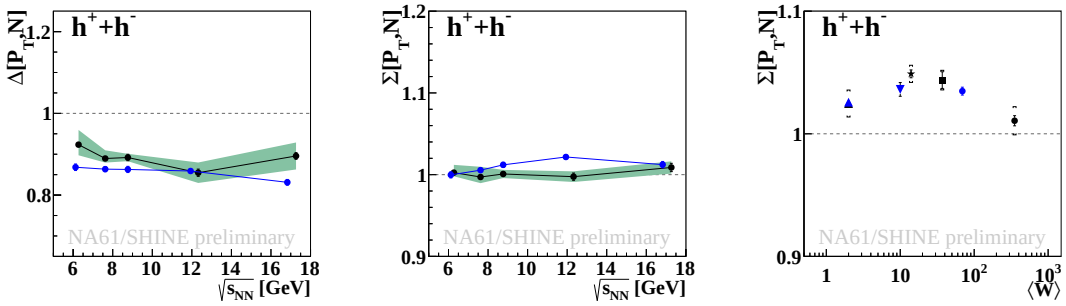

Figure 31: Left and middle: $\Delta[P_{\mathrm{T}}, N]$ and $\Sigma[P_{\mathrm{T}}, N]$ in NA61/SHINE 0-5% Ar+Sc (blue points) and NA49 0-7.2% Pb+Pb (black points). Results in $1.1 < y_\pi < 2.6$ and $y_p < y_{beam} - 0.5$ with narrow azimuthal acceptance [28]. Right: $\Sigma[P_T, N]$ at 150/158A GeV/c. Black points are NA49 [28] data (p+p, 0-15.3% C+C, 0-12.2% Si+Si, 0-5% Pb+Pb), blue ones preliminary NA61/SHINE (p+p, 0-5% Be+Be, 0-5% Ar+Sc). Results in $1.1 < y_\pi < 2.6$ and with almost complete azimuthal acceptance.

defined strongly intensive Ω measure [30]. Ω is defined as a mean of $\Delta[N, E_p]$ and $\Sigma[N, E_p]$, where $E_p = E_{beam} - E_{PSD}$. For the Boltzmann ideal gas of particles in the Grand Canonical Ensemble and for the absence of correlation between E_p and N in a fixed volume such quantity is equal to the scaled variance of multiplicity for one source. Therefore, for the most central collisions $\omega[N] = \Omega[N, E_p]$ is expected (Fig. 32). There is no significant non-monotonic behaviour in the energy dependence of those two measures, however an interesting effect was observed (see Fig. 33). Namely, for negatively charged hadrons (the cleanest sample) at 150/158A GeV/c the scaled variance of the multiplicity distribution is much below 1 for 0-0.2% Ar+Sc and 0-1% Pb+Pb and above 1 for p+p. Within the Wounded Nucleon Model (WNM) one can write [31]:

$$\omega[N] = \omega^*[N] + \langle N \rangle / \langle W \rangle \cdot \omega[W], \tag{2}$$

where W is the number of wounded nucleons, $\omega^*[N]$ is the scaled variance calculated for any fixed value of W (i.e. $= \omega[N]_{pp}$ because the number of wounded nucleons in p+p interactions is fixed to two), and $\omega[W]$ represents fluctuations in W. Thus, one can expect that $\omega[N]_{AA}$ should be grater or equal $\omega[N]_{pp}$. Therefore, the NA61/SHINE and NA49 results clearly contradict the Wounded Nucleon Model. Moreover, they also contradict a non-interacting (ideal) gas of Boltzmann particles in the grand canonical ensemble (IB-GCE). In the IB-GCE multiplicity distribution is Poissonian ($\omega[N] = 1$), independent of the (fixed) system volume, and thus $\omega[N]_{AA} < 1$ is forbidden in the IB-GCE. On the other hand, $\omega[N]$ can increase due to resonance decays and Bose-Einstein statistics and decrease due to conservation laws [32]. In fact, the NA49 Pb+Pb point is well described by the hadron gas model in the micro canonical ensemble (HG-MCE) [32]. Within the statistical models $\omega[N] \gg 1$, as seen in p+p, can be understood as a result of volume and/or energy fluctuations [33].

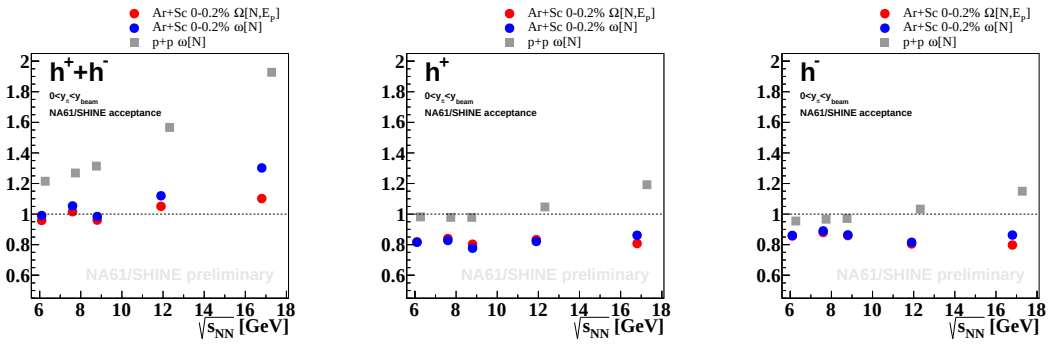

Figure 32: $\omega[N]$ (blue points) and $\Omega[N, E_p]$ (red points) in NA61/SHINE 0-0.2% Ar+Sc, as well as $\omega[N]$ in NA61/SHINE p+p (grey points). Results for all charged hadrons ($h^+ + h^-$, left), positively charged ones (h^+, middle) and negatively charged ones (h^-, right) and in $p_T < 1.5$ GeV/c.

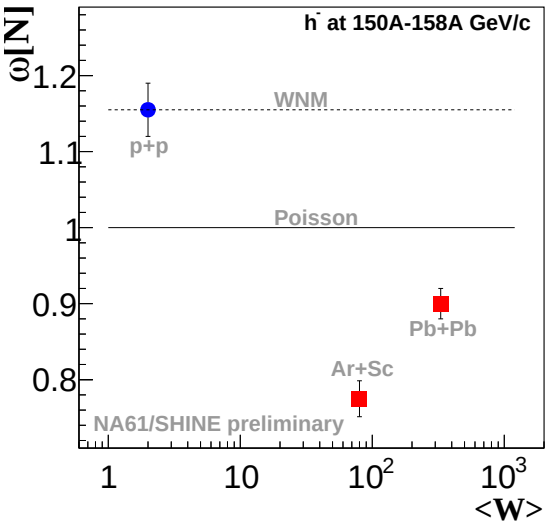

Figure 33: Scaled variance ($\omega[N]$) for negatively charged hadrons measured in p+p [26], 0-1% Pb+Pb [34], and 0-0.2% Ar+Sc collisions at 150/158A GeV/c. Results in $0 < y_\pi < y_{beam}$ and in NA49-B acceptance [34]. Experimental data are compared to predictions of Wounded Nucleon Model.

5.1.6 Higher order moments of net-charge distribution in p+p

Higher order moments of multiplicity distributions (e.g. skewness S and kurtosis κ) are expected to be more sensitive (than the variance σ^2) to fluctuations at a CP [35, 36]. Moreover, they can be used to test (statistical and dynamical) models (first moments do not allow to distinguish between different types of models; already for second moments fluctuations are different in string and statistical models). Finally, higher moments of

conserved quantum numbers ($i = B, Q, S$) allow for direct comparison to theory via susceptibilities: $S\sigma \approx \chi_i^3/\chi_i^2$, $\kappa\sigma^2 \approx \chi_i^4/\chi_i^2$.

The scaled variance (ω) and products of higher order moments of net-charge distributions, measured in inelastic p+p interactions, are shown in Fig. 34 (see also Fig. 35 for the same quantities for h^- only). No anomalies are observed suggesting a CP. Results of net-charge fluctuations disagree with expectations for independent particle production (Skellam) but EPOS1.99 describes the data quite well.

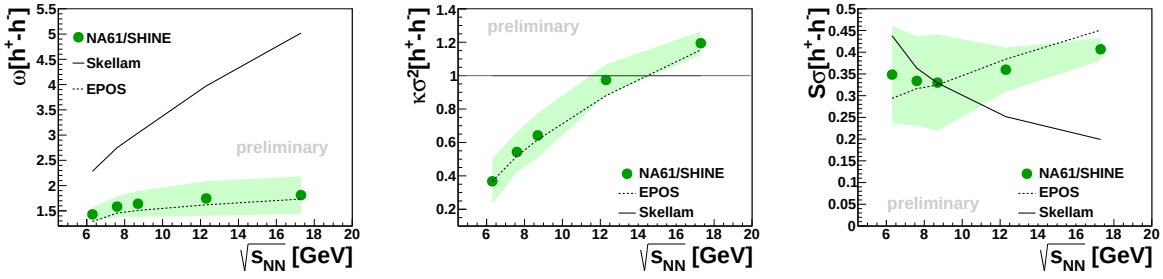

Figure 34: Scaled variance (ω) and products of higher order moments of net-charge distributions measured in inelastic p+p interactions as a function of collision energy.

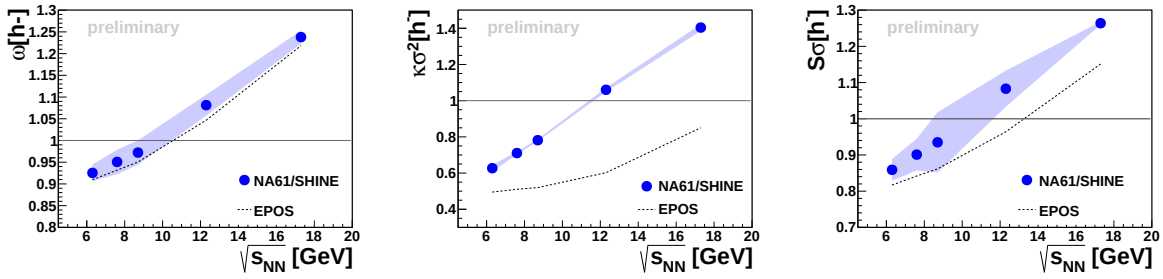

Figure 35: Scaled variance (ω) and products of higher order moments of multiplicity distribution of negatively charged hadrons measured in inelastic p+p interactions as a function of collision energy.

5.2 Flow performance in Pb+Pb collisions

The initial spatial asymmetry in a nucleus-nucleus collision due to the interaction among constituents should lead to the azimuthal asymmetry in momentum distribution of produced particles. This asymmetry can be measured via azimuthal distributions of produced particles with respect to the initial symmetry plane. In case of no fluctuations in the shape of the initial energy distribution, this plane is expected to coincide with the reaction plane (RP) spanned by the impact parameter and the beam direction. With

known reaction plane angle (Ψ_{RP}), the azimuthal angle (φ) distribution of particle momenta can be decomposed in a Fourier series:

$$\frac{dN}{d(\varphi - \Psi_{RP})} \sim 1 + 2\sum_{n=1}^{\infty} v_n \cos\Big(n(\varphi - \Psi_{RP})\Big), \tag{3}$$

where the flow coefficients v_n quantify the asymmetry in momentum space.

In NA61/SHINE the measurement of flow harmonics in Pb+Pb collisions provides a reference for studying collective flow effects in smaller systems explored by the collision energy and system size scan. At the moment the only published results for v_1 and v_2 of pions, protons, and Λ hyperons at 40A GeV and 158A GeV are available from NA49 [37,38]. With the new data samples of Pb+Pb collisions to be collected by NA61/

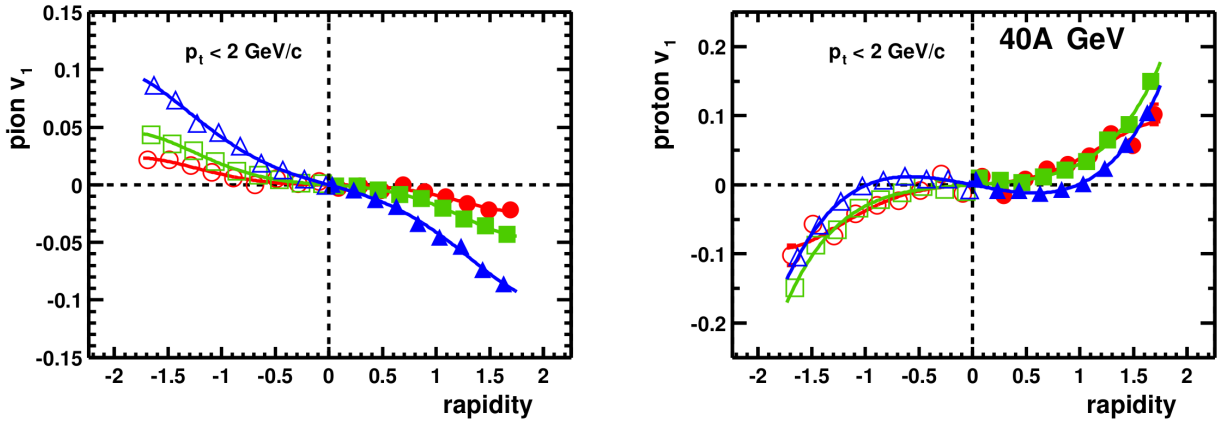

Figure 36: Directed flow of pions (left) and protons (right) in Pb+Pb collisions at 40A GeV measured by NA49 [37].

SHINE in November 2016 and 2018 it will be possible to extend the measurements of the anisotropic flow as a function of collision centrality with beams in the momentum range from 13A GeV/c to 158A GeV/c and to forward rapidities which are significantly larger than what is presently accessible by RHIC experiments (see e.g. results by STAR [39]).

Here we report on the NA61/SHINE performance studies of the charged hadron directed flow measurement performed based on Pb+Pb test data collected by NA61/SHINE in November 2015 without magnetic field. During this period about 2M events of minimum bias Pb+Pb collisions at 30A GeV/c were recorded. Figure 37(left) shows the minimum bias trigger performance.

The sub-groups of the PSD modules which were used for centrality determination and for flow analysis using sub-events PSD1, PSD2, PSD3, and PSD4 are shown in Fig. 37(right).

Events were selected according to the minimum bias trigger T4 in an interval around z-vertex position (z_v) along the beam $-589 < z_v < -584.5$. Additional selection criteria for the signal ($S3_{ADC}$) in the S3 trigger detector of $S3_{ADC} > 50$ was used to remove

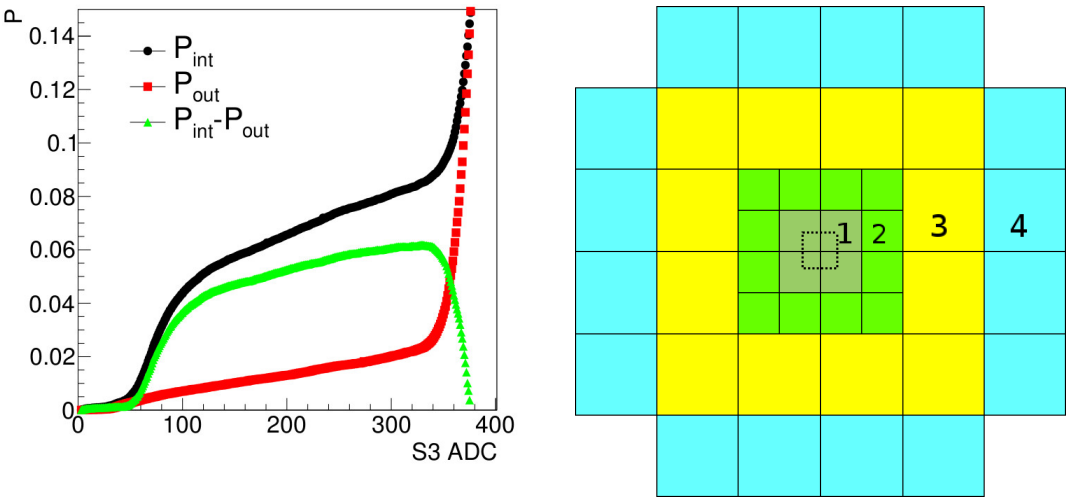

Figure 37: Left: Performance of the minimum bias trigger for Pb+Pb collisions at 30A GeV/c. About 90% of all inelastic Pb+Pb collisions were selected using a 500 μm thick S3 scintillation counter installed 20 cm downstream from the target. Over 70% percent of the registered events were interactions in the 3 mm thick Pb target. The remaining are off-target interactions. Right: Transverse to the beam layout of the PSD modules. Dashed line shows module number 45, which was used for centrality determination.

events which corresponds to the interaction with the detector material downstream the target. Event cuts based on the multiplicity of produced particles (M_{ref}) and energy of measured by PSD (E_{tot}) were also applied. The multiplicity M_{ref} is a number of accepted for analysis tracks at mid-rapidity $|\eta - \eta_{beam}| < 0.5$ ($\eta_{beam} = 2.0792$) and with tighter DCA cut of 2 cm. E_{tot} is a total energy for 44 modules in PSD. Details of the TPC track selection are provided below. To remove the outlier events around the main correlation band for M_{ref} vs. E_{tot} an empirical cut $|5717 - 23.8M_{ref} - E_{tot}| < 1200$ was introduced. With this event selection about 600 thousands of Pb+Pb collisions were used for the analysis. Distributions of the multiplicity and the PSD energy for different sub-events are shown in Fig. 38.

Correlation between multiplicity and energy in different PSD sub-events is shown in Fig. 39. Resulting acceptance map for the pseudo-rapidity η and azimuthal angle φ for the selected TPC tracks is shown in Fig. 39 (lower rightmost panel).

Tracks reconstructed in NA61/SHINE TPCs (VTPC-1/2 and MTPC-L/R) were selected in the region of pseudo-rapidity: $1 < \eta < 4.7$. The minimum (maximum) number of clusters ($N_{clusters}$) in either of VTPC-1, VTPC-2 and MTPC-L/R were required to be greater than 10, 6, and 10 (less than 72, 72, and 90), respectively. To reduce the number of the secondary tracks the cuts on the distance of closest approach (DCA) to the vertex in x and y directions were chosen to be $|DCA_{x,y}| < 3$ cm and $\sqrt{DCA_x^2 + DCA_y^2} < 3$ cm.

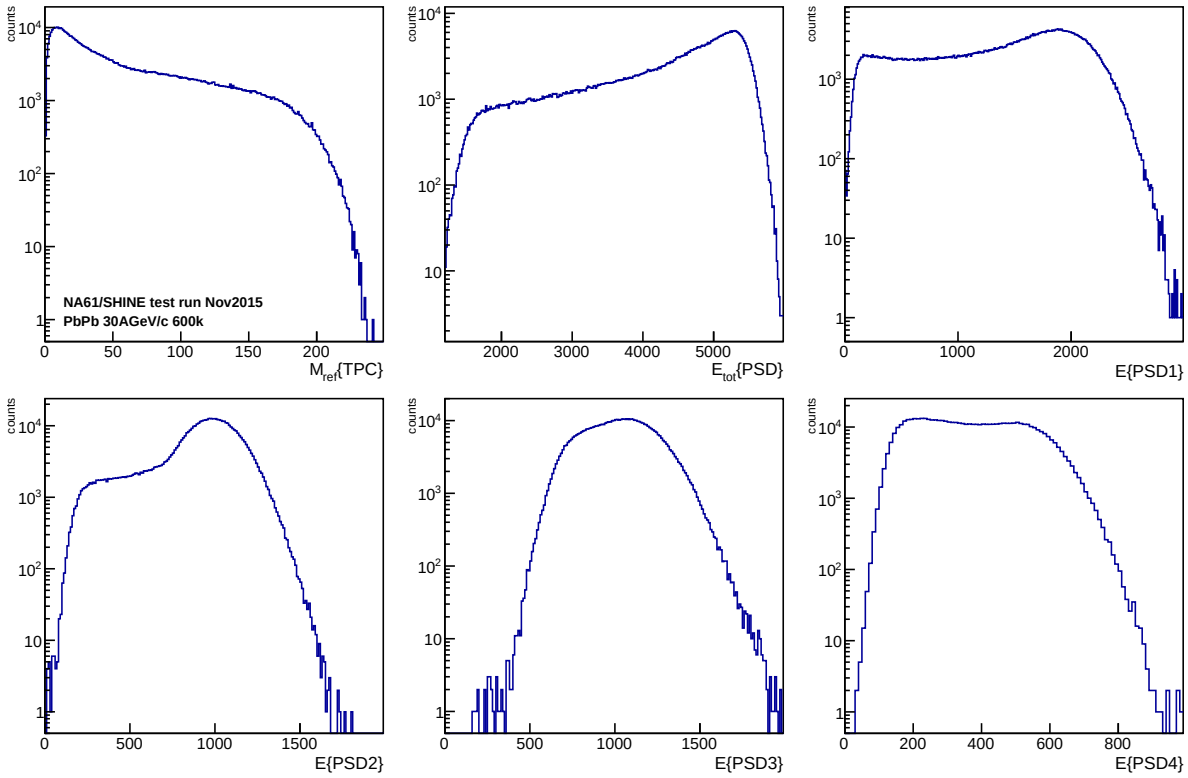

Figure 38: Distributions of the multiplicity and energy in different PSD sub-events.

Rejection of events with poorly reconstructed collision vertex was done by requiring the good quality of the vertex fit.

5.2.1 Centrality determination

The size and evolution of the medium created in a heavy-ion collision is expected to depend on collision energy and initial state geometry, the latter cannot be directly measured. Experimentally collisions are characterized by measured in TPCs particle multiplicity and/or forward energy measured by PSD, which is related to projectile spectators. For this, collisions are grouped into event (centrality) classes with the most central class defined by events with the highest multiplicity (smallest forward energy) which is expected to correspond to the smallest values of the impact parameter. For this analysis energy measured in the sub-groups of the PSD modules, PSD1, PSD2, PSD3 and PSD4 as shown in Fig. 37 (right), was used.

Centrality determination is performed following the procedure described in Ref. [40]. The procedure consists of the following steps:

(i) Determine the total cross-section and the "anchor" point (a value below which centrality determination is not reliable) based on a fit of the data multiplicity distribu-

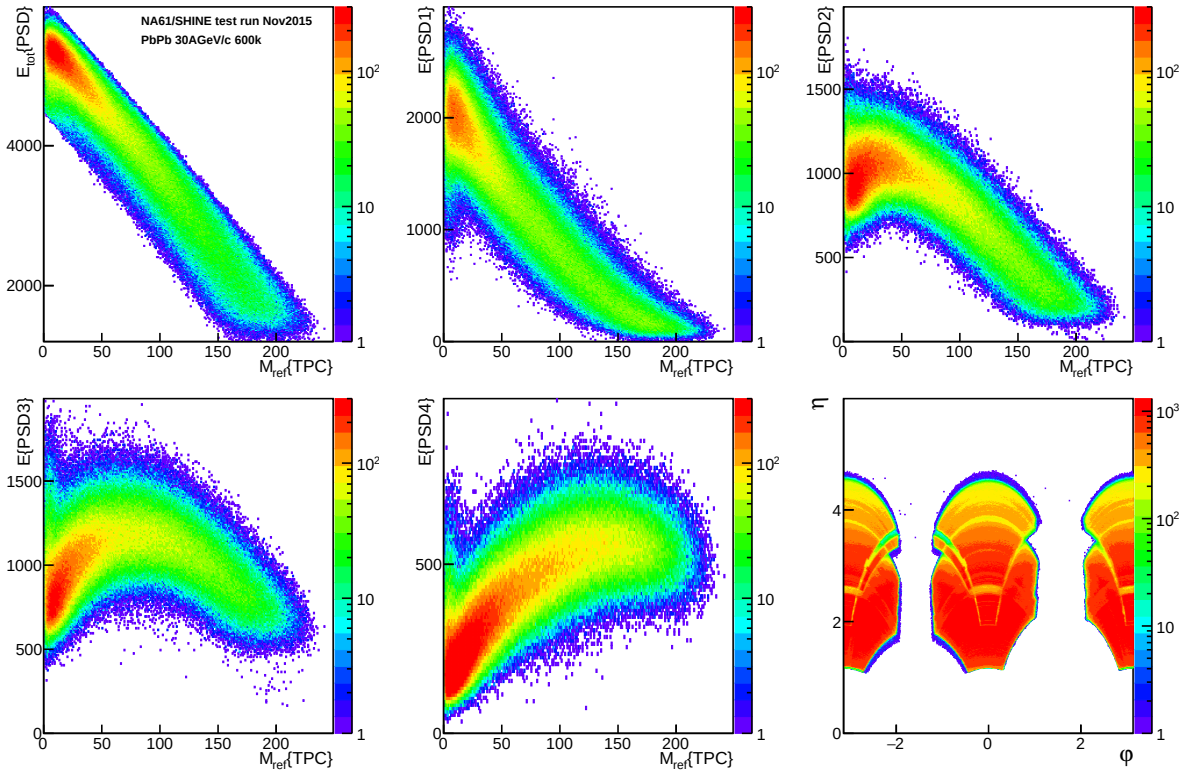

Figure 39: Correlation between multiplicity and energy in different PSD sub-events and acceptance map in pseudo-rapidity η and azimuthal angle φ for the selected TPC tracks.

tion with a distribution generated within an MC-Glauber model:

$$F_{fit}(f,\mu,\sigma) = P_{\mu,\sigma}[fN_{part} + (1-f)N_{coll}]. \quad (4)$$

Here $P_{\mu,\sigma}$ is a negative binomial distribution, N_{part} and N_{coll} number of participants and number of binary collisions generated with the MC-Glauber model. Figure 40 (left) shows the result of the MC-Glauber fit and Fig. 40(right) the χ^2 dependence on fit parameters.

(ii) Scale (equalize) energy in each PSD sub-event (E_{PSD}) and TPC multiplicity (M_{TPC}) determined run-by-run to the overall mean. The corresponding run-by-run correction factors are shown in Fig. 41.

(iii) Plot the correlation between M_{TPC}/M_{TPC}^{max} and E_{PSD}/E_{PSD}^{max}, where M_{TPC}^{max} and E_{PSD}^{max} are maximum values of M_{TPC} and E_{PSD}, respectively (see Fig. 42) and

(iv) Parametrize the correlation between multiplicity and/or energy in the PSD sub-events:

(a) fit the correlation profile (black circles) with a polynomial function (black line)

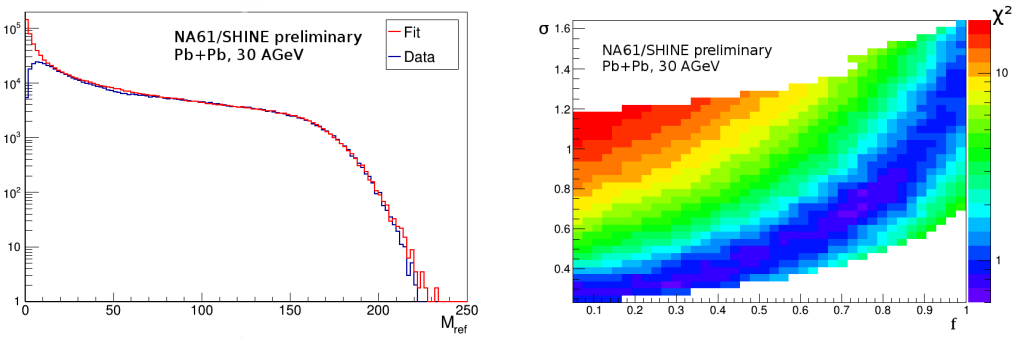

Figure 40: (Left) Multiplicity distribution of charged particles in NA61/SHINE TPCs produced in minimum bias Pb+Pb collisions at 30A GeV/c together with Glauber fit function. (Right) χ^2 distribution for different values of the Glauber function parameters.

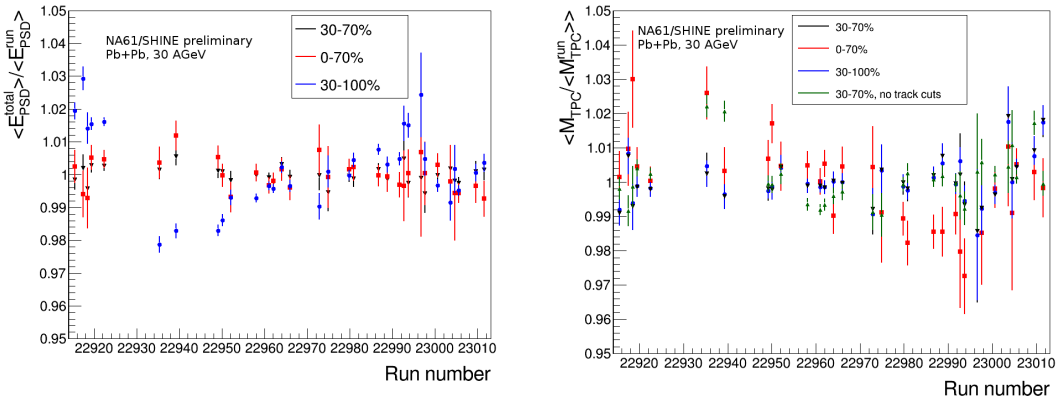

Figure 41: Run-by-run corrections to the measured PSD energy (left) and TPC multiplicity (right) for different event classes.

(b) recalculate profile (red squares) using the slope of the fit

(c) Refit profile (red line)

Figure 42 (right) shows the intermediate and resulting fit to the data.

(v) Slice the correlation in the direction perpendicular to the fit (Fig. 42 (left) or divide the M_{TPC} / E_{PSD} distribution in percentiles of the total number of events (see Fig. 43 (left).

5.2.2 Performance of the directed flow measurement

To estimate the reaction plane orientation it is common to use the azimuthal asymmetry of particle production in the transverse plane to the beam direction. Due to the momen-

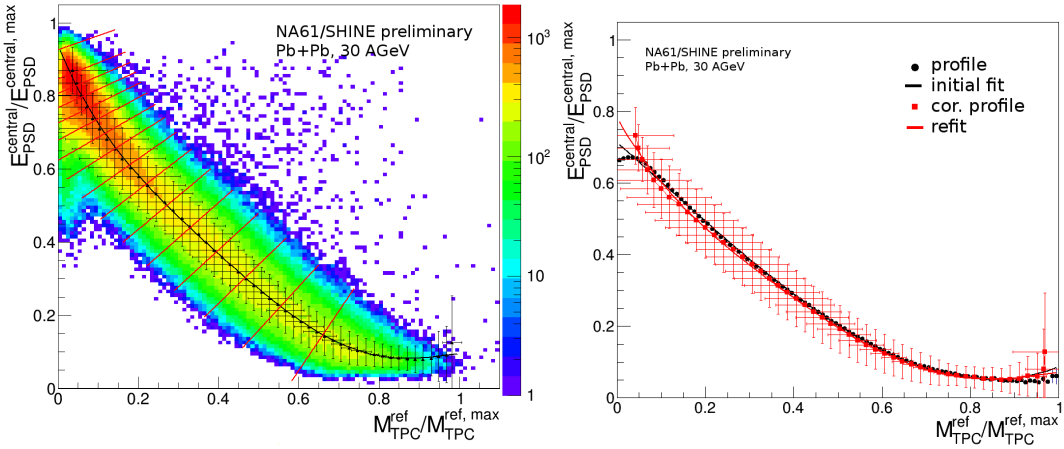

Figure 42: Illustration of the centrality determination procedure (left) with equal percentiles. The correlation between the energy deposited in the central modules of PSD (PSD1+PSD2+M45) and the TPC multiplicity overlayed with the result of the fit procedure (right).

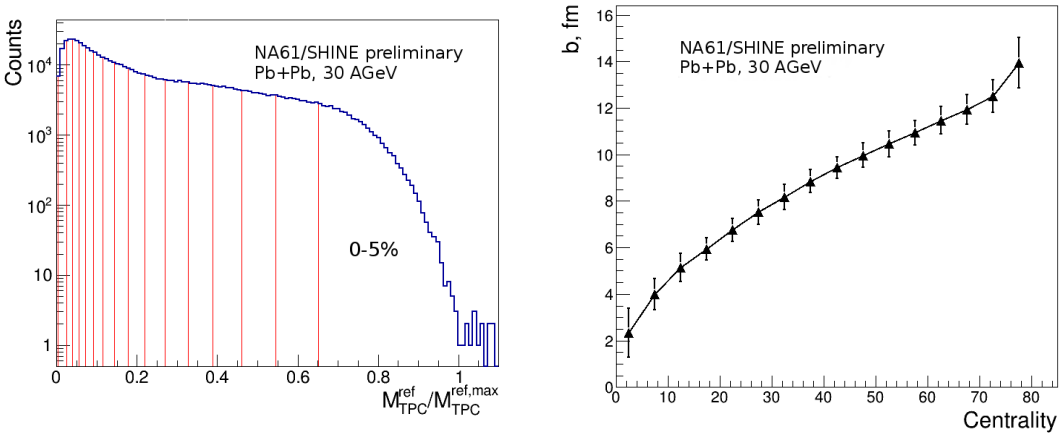

Figure 43: Illustration of the centrality determination procedure (left) with equal percentiles for the multiplicity in TPC. Dependence of the impact parameter versus centrality shown on the right panel.

tum transfer between participants and spectators, the spectators (fragments of projectile and target nuclei) are deflected in the course of the collision. For non-central collisions, the asymmetry of the initial energy density in the transverse plane is expected to be aligned in the direction of the reaction plane, and thus the spectator deflection direction is likely to be correlated with the impact parameter (or reaction plane) direction. Therefore it seems that one can estimate the reaction plane angle with spectators detected in the PSD and extract flow of produced particles detected in TPC with respect to this

plane.

The asymmetry of the measured distributions is described in terms of **Q**-vector defined on event-by-event basis for the PSD sub-events:

$$\mathbf{Q} = \frac{1}{E}\sum_i E_i \, \mathbf{n_i}, \tag{5}$$

where unit vector $\mathbf{n_i}$ points to the center of the i-th PSD module, E_i is the energy deposition in the i-th module and $E = \sum_i E_i$ is the total energy of the PSD sub-event. For each particle track i reconstructed with the TPC an n-th harmonic unit $\mathbf{u_{n,i}}$-vector is defined (for directed flow measurement $n = 1$):

$$\mathbf{u_{n,i}} = \{\cos n\varphi_i, \sin n\varphi_i\}. \tag{6}$$

The TPC **q**-vectors were calculated in 0.1 wide slices of pseudo-rapidity with an equation:

$$\mathbf{q} = \frac{1}{M}\sum_i \mathbf{u_{1,i}} \, , \tag{7}$$

where M is the number of particle tracks in a given slices of pseudo-rapidity. We used an observable for directed flow v_1 which is constructed from correlation between two reference PSD **Q**-vectors and from correlation for each of them with a TPC **q**-vectors. Assuming that the underlying distribution for azimuthal angles is given by Eq. (3), one can derive the relation between the **Q**-vector correlations and flow harmonics:

$$\langle Q_i^A Q_j^B \rangle \propto \frac{V_1^A V_1^B}{2}\,\delta_{ij}\,, \;\; \langle q_i Q_j^A \rangle \propto \frac{v_1 V_1^A}{2}\,\delta_{ij}\,, \tag{8}$$

where $i, j \in \{x; y\}$. According to Eq.(8), an independent estimates of the **Q**-vector correction factors $C_i^A\{B, C\}$ and flow harmonics $v_{1,i}\{A, B\}$ can be written as:

$$C_i^A\{B,C\} = \sqrt{2\frac{\langle Q_i^A Q_i^B\rangle\langle Q_i^A Q_i^C\rangle}{\langle Q_i^B Q_i^C\rangle}}\,, \;\; v_{1,i}\{A,B\} = \sqrt{2\frac{\langle q_i Q_i^A\rangle\langle q_i Q_i^B\rangle}{\langle Q_i^A Q_i^B\rangle}}. \tag{9}$$

Imperfect acceptance and efficiency of the detector bias the azimuthal angle distribution of measured particles (see e.g. Fig. 39 (lower rightmost panel)). A correction procedure for the **Q**-vectors was proposed in Ref. [41]. This procedure is implemented in a software framework (QnCorrections framework) [42,43]. In the current study, each **q**-vector for TPC and **Q**-vector for different PSD sub-events were corrected with the recentering procedure using the QnCorrections framework:

$$\mathbf{Q}' = \mathbf{Q} - \langle \mathbf{Q} \rangle \, , \;\; \mathbf{q}' = \mathbf{q} - \langle \mathbf{q} \rangle \, . \tag{10}$$

Other types of corrections provided by the QnCorrections framework will be investigated in a future. The recentering of the PSD **Q**-vectors and TPC **q**-vectors was applied

separately in different event classes defined by the PSD energy and track multiplicity, respectively. The average **Q**-vector value in each event class before and after recentering is shown in Fig. 44(left).

Figure 44(right) shows the correlation $C_i^A\{B,C\}$ defined by the LHS of the Eq. (9) for **Q**-vectors corrected with the recentering procedure. The operation of NA61/SHINE

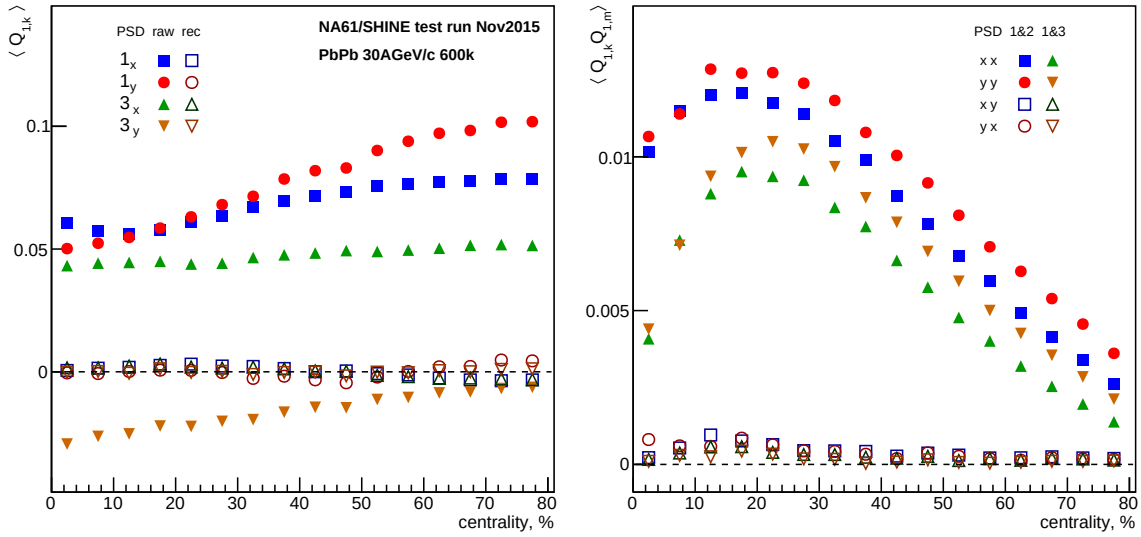

Figure 44: Left: The average **Q**-vector value in each event class before and after recentering for the PSD1 and PSD3 sub-event **Q**-vectors. Right: Correlation $C_i^A\{B,C\}$ defined by the LHS of the Eq. (9) for the PSD1 and PSD3 sub-event **Q**-vectors corrected with the recentering procedure.

without magnetic field during November 2015 Pb test run leads to rather good symmetry between **Q**-vector correlations for x and y components.

Event plane resolution correction is defined similar to Eq. (9) (left), but instead of the **Q**-vector components the event plane angles, defined as $\mathbf{Q} = |\mathbf{Q}|(\cos\Psi_{\rm EP}, \sin\Psi_{\rm EP})$, are used:

$$R_i^A\{B,C\} = \sqrt{\frac{\langle\cos(\Psi_{\rm EP}^A - \Psi_{\rm EP}^B)\rangle\langle\cos(\Psi_{\rm EP}^A - \Psi_{\rm EP}^C)\rangle}{\langle\cos(\Psi_{\rm EP}^B - \Psi_{\rm EP}^C)\rangle}}. \tag{11}$$

Figure 45(left) shows an example of the resolution correction for PSD2 sub-event. In future, such comparison will allow to study the systematic biases in the event plane determination.

Results for charged hadrons directed flow are shown in Fig. 45 (right). The absence of the magnetic field during the Pb test run does not allow to use particle identification capabilities of NA61/SHINE. Directed flow as a function of pseudo-rapidity (shifted to the that of the beam $\eta_{beam} = 2.0792$) was measured in 3 centrality classes ($0\% - 20\%$, $20\% - 40\%$ and $40\% - 60\%$) using the centrality determination procedure introduced in a previous subsection. No efficiency correction was used for extraction of v_1. The result

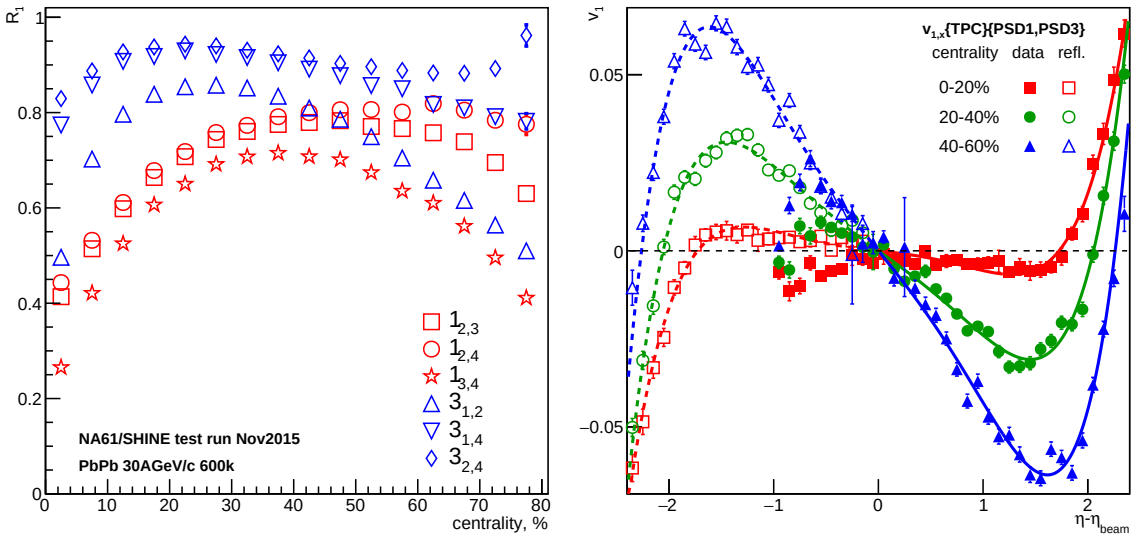

Figure 45: Left: resolution correction for the PSD1 and PSD3 sub-events. Right: Uncorrected charged hadrons directed flow in three centrality classes obtained using the x components of the TPC **q**-vectors and PSD1 and PSD3 **Q**-vectors.

is based on the x-component of the **q**- and **Q**-vectors which are least distorted due to the TPC geometry. The **Q**-vectors for PSD1 and PSD3 sub-events were used as a reference for v_1 determination.

In summary for this section, a sample of Pb+Pb collision collected during the test run in November 2015 with Pb beam of 30A GeV/c is very helpful for performance evaluation and preparation for the analysis of the date to be collected by NA61/SHINE in November 2016.

5.3 New results for neutrino physics

5.3.1 Measurements for T2K

Final results on hadron production in p+C interactions at 31 GeV/c have been recently published [44]. The analysis is based on the full set of data collected during the 2009 run using a graphite target with a thickness of 4% of a nuclear interaction length (the thin target). Inelastic and production cross sections as well as spectra of $\pi^{\pm}$, $K^{\pm}$, p, K^0_S and Λ have been measured with a high precision.

These measurements are essential for predictions of the initial neutrino and anti-neutrino fluxes in the T2K long baseline neutrino oscillation experiment in Japan. They have already been used for the updated T2K results presented during 2016 summer conferences. Furthermore, these measurements provide important input to improve hadron production models needed for the interpretation of air showers initiated by ultra high energy cosmic particles.

Recently new measurements of particle emission from a replica of the T2K 90 cm-long carbon target have been released [45]. These results are obtained using data collected during a high-statistics run in 2009. An efficient use of the long-target measurements for (anti-)neutrino flux predictions in T2K requires dedicated reconstruction and analysis techniques. Fully-corrected differential yields of $\pi^{\pm}$-mesons from the surface of the T2K replica target for incoming 31 GeV/c protons have been obtained. A possible strategy to implement these results into the T2K neutrino beam predictions has been discussed and the propagation of the uncertainties of these results to the final neutrino flux has been performed.

Although the recent $\pi^{\pm}$ long-target results will further reduce the T2K (anti-)neutrino flux uncertainty below 10%, the T2K goal is to reach uncertainty below 5%. For this purpose a high statistics dataset using the T2K replica target was recorded in 2010. Analysis of this dataset is being finalized. There are several key improvements in the data recored in 2010:

(i) 3.5 times higher statistics,

(ii) specially designed trigger with narrow beam profile, close to the T2K conditions,

(iii) about 10% of the events were collected with the maximum magnetic field, which can bend the beam particle to the TPCs and to measure its properties.

High statistics allow measurement of the $K^{\pm}$ differential yields coming from the surface of the T2K replica target. Neutrinos produced in kaon decays give rise to the high energy tail in the T2K (anti-)neutrino spectra. Different beam profiles can greatly change the emission of particles from the surface of the target. In order to reduce the difference between the T2K and the NA61/SHINE beam profiles, we used specially designed trigger which selects narrower beam hitting the target center (see Fig. 46). Events recorded with the maximum magnetic field are used to extract information about the beam particles which pass through the target without interaction. These protons interact with the elements of the T2K neutrino beam-line and also contribute to the (anti-)neutrino flux.

A dedicated analysis procedure based on the $\mathrm{d}E/\mathrm{d}x - m^2_{TOF}$ particle identification (see Ref. [45]) is applied to the T2K replica target data as shown in Figure 47. Up to now we have extracted uncorrected $\pi^{\pm}$ and $K^{\pm}$ yields. The results are presented in the bins of momentum, polar angle and longitudinal position along the target surface. Contribution of the hadrons to the neutrino flux depends on the longitudinal position of the particle at the target surface. The T2K requirement is to divide the target into five longitudinal bins and the target downstream face. An example of the uncorrected $\pi^{\pm}$ and $K^{\pm}$ differential yields are presented in Fig. 48 for the second longitudinal bin and one polar angle bin. Fully corrected preliminary results are expected before the end of this year. Our plan is to complete the analysis and to publish the $\pi^{\pm}$, $K^{\pm}$ and p yields by September 2017.

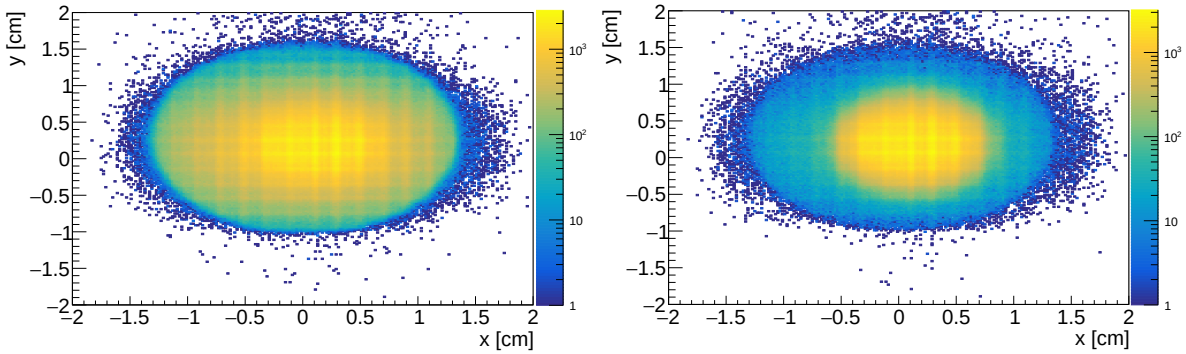

Figure 46: Proton beam profile for events with standard $T2$ interaction trigger (left) and narrower beam profile after selecting events with the specialized $T3$ trigger, closely reproducing the beam conditions in T2K (right).

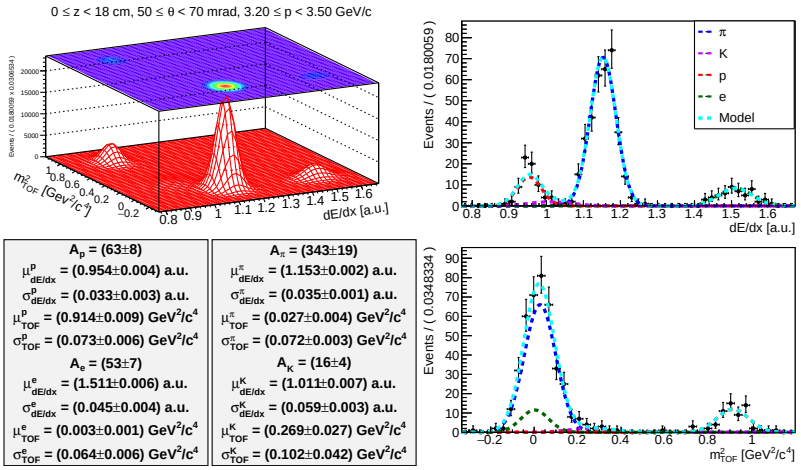

Figure 47: An example of the $\mathrm{d}E/\mathrm{d}x - m^2_{TOF}$ particle identification for a selected $\{z, \theta, p\}$ bin.

5.3.2 Measurements for Fermilab neutrino beams

NA61/SHINE has recently started on a program of hadron production measurements to benefit the Fermilab neutrino program. The current NuMI beam uses 120 GeV/c protons on a graphite target to produce neutrinos, and serves the MINOS+, Minerva, and NOvA experiments. The proposed future LBNF beamline from Fermilab to South Dakota will provide an even higher intensity beam using protons with an energy between 60-120 GeV/c (still to be determined) on a graphite or possibly beryllium target. In addition to measurements of the particles produced by the interactions of the primary beam protons, the hadrons produced by secondary interactions of lower-energy protons and pions in the target and aluminum horns also contribute significantly to the neutrino flux. NA61/SHINE is well-suited to make measurements that can reduce the flux uncertainties for the Fermilab neutrino experiments.

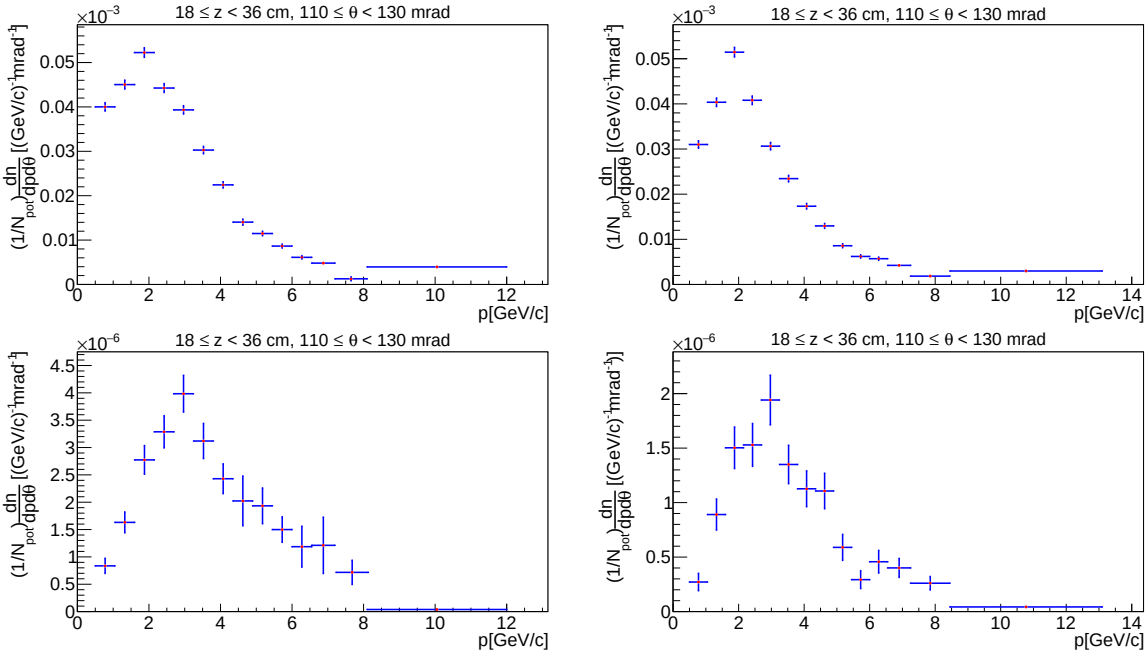

Figure 48: Uncorrected differential yields as a function of momentum for π^+ (top left), π^- (top right), K^+ (bottom left) and K^- (bottom right) for a selected $\{z, \theta\}$ bin.

In the fall of 2015, several weeks of data were collected (see Table 1) for various reactions. Unfortunately the vertex magnets were operational during these runs. So it is not possible to extract spectra, but analyses are in progress to determine production cross sections for all of these reactions. The preliminary result for K^+ + C at 60 GeV/c will be described below.

In the summer of 2016, data were collected for 60 GeV/c p+C with fully operational magnets, and a spectrum analysis will begin on this data set soon. Data for additional reactions (see Table 2) are being collected in September-October 2016, also with vertex magnets operational.

π^+ + C at 31 GeV/c

During the 2009 thin target data taking for T2K, the main trigger recorded data of protons interacting with a carbon target. A secondary trigger recorded all interactions. From studies of the beam composition, we know these beam particles are mostly π^+ particles. The beam has a small contamination of e^+ and K^+, which incurs an additional difficulty in normalizing the results. These pion interactions have been analysed and multiplicity spectra of π^+ and π^- have been measured. The preliminary results include statistical uncertainties only. Analysis of the systematic uncertainties and normalization uncertainties are ongoing. Because the overall normalization still needs to be understood, only the shapes of the multiplicity spectra have been released as preliminary. The overall vertical scale has been obscured by normalizing the momenta

distributions for each θ bin. A sample of the preliminary multiplicity spectra are shown in Fig. 49.

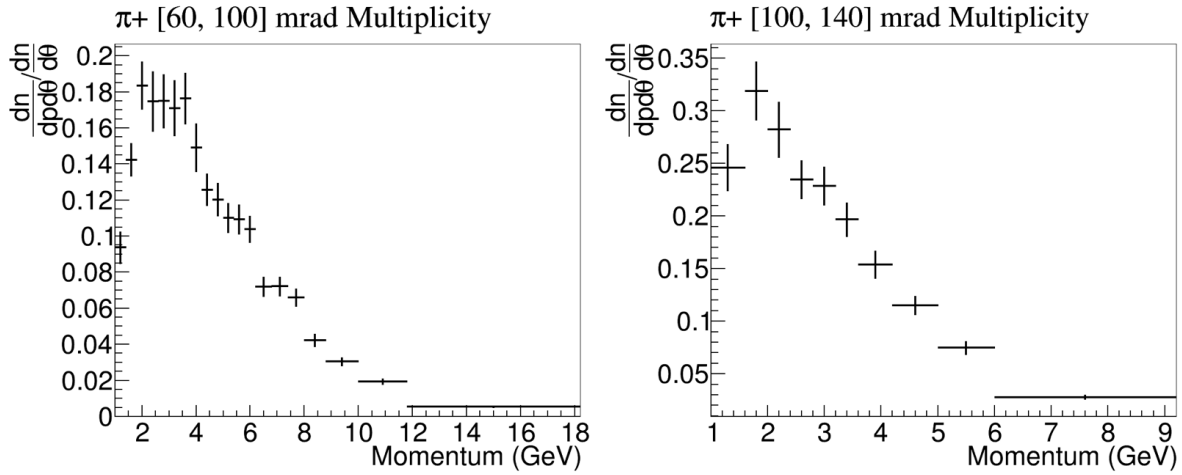

Figure 49: Normalized multiplicity spectra of π^+ from π^+ +C interactions at 31 GeV/c for two θ bins: $[60, 100]$ mrad (left) and $[100, 140]$ mrad (right). The absolute scale has been obscured by normalizing the momenta distributions for each θ bin. Only statistical uncertainties are shown.

π^+ + C and π^+ + Al at 31 GeV/c Total Cross Section Measurements

During the 2015 fall run, interactions of 31 GeV/c π^+ with carbon and aluminium targets were recorded. Because the magnets were turned off during this data run, no multiplicity analysis can be performed. However, studies are ongoing to measure the total inelastic and production cross sections for both targets. The π^+ + C cross section measurements will be used to perform the normalization correction and constrain the normalization uncertainty for the π^+ + C multiplicity analysis.

K^+ + C at 60 GeV/c

NA61/SHINE recorded data in 2015 using 60 GeV/c K^+ collisions on C target with no magnetic field. A measurement of the total production cross section from the collisions of 60 GeV/c kaons on a 2.0 cm long carbon (graphite) target is presented.

The events are selected by applying WFA beam time window cut, good BPD cut and beam radius cut [3]. After passing these event selections, the number of $T1$ triggered events is 454047 for target inserted (IN) sample and 218200 for target removed (OUT) sample, respectively. The total number of $T1 \wedge T2$ triggered events for IN target and

[3] Events are selected for BPD radius less than 1.0 cm ($\sqrt{x_{BPD}^2 + y_{BPD}^2} < 1.0$ cm).

OUT target data as 18864 and 2744, respectively. The interaction probability measured using IN and OUT target samples is determined to be 0.0293 ± 0.0004 (stat).

The interaction probability measurement allows one to calculate a trigger cross section of 161.4 ± 2.3 (stat) mb. The trigger cross section can be written as the sum of the total elastic (EL), quasi-elastic (QE) and production cross sections with the corresponding trigger correction factors. GEANT4 based Monte Carlo studies are performed to estimate the trigger correction factors. After applying the correction terms, the production (or absorption) cross section is extracted with a value 146.1 ± 2.3 (stat) mb.

An estimated systematic uncertainty of 2.8 mb for EL and QE subtraction is determined by varying the beam configurations using different physics models in the GEANT4 simulation. The systematics of kaon beam purity is estimated to 0.3 mb by using the CEDAR pressure scan. The systematics for the holder interactions is calculated to be 0.6 mb. In addition a MC study determined the S4 trigger counter and beam size systematics to be 0.4 mb and 0.3 mb, respectively. The target density systematics is 0.8 mb by assuming 0.01 g/cm^3 uncertainty on the target density. Finally the interaction trigger systematic is estimated to be 0.3 mb after determining the S4 counter efficiency.

After applying the target holder and trigger efficiency corrections on the measured production cross sections the final production cross section result is determined to be 144.9 mb $\pm$ 2.3 mb (stat) $\pm$ 3.0 mb (syst). This result is consistent with the measured absorption (production) cross section of K + C at 60 GeV/c published in Ref. [46].

5.4 New results for cosmic-ray physics

5.4.1 Air Shower Physics

When cosmic rays of high energy collide with the nuclei of the atmosphere, they initiate extensive air showers (EAS). The Earth's atmosphere then acts as a calorimeter in which the particle shower evolves. A complete measurement of the shower is not possible, often only the particles are sampled at select positions at ground level or the ionization energy deposited in the atmosphere is measured. Therefore the interpretation of EAS data, and in particular the determination of the composition of cosmic rays, relies to a large extent on a correct modelling of hadron-air interactions that occur during the shower development [47]. Experiments such as the Pierre Auger Observatory [48], KASCADE-Grande [49], IceTop [50], HiRes-MIA [51] or the Telescope Array [52] use models for the interpretation of measurements. However, there is mounting evidence that current models do not provide a satisfactory description of muon production in air showers (see Refs. [53–55]).

Regarding pion interactions, models used for air shower simulations such as QGSJETII-04 [56], EPOSLHC [57] and SIBYLL2.3 [58] were tuned only to data on π^+ + C interactions at 100 GeV/c of Barton *et al.* [59] and π^++p interactions at 250 GeV/c measured by the NA22 experiment [60–62].

Therefore the measurements of π + C data from NA61/SHINE would provide data

with the least amount of interpretation that any measurement previously, as the dominant interaction in the air showers is π + N.

Identified Particle Spectra In 2015, preliminary spectra of identified π^+ and π^- mesons in π + C interactions at 158 and 350 GeV/c was published [63]. This analysis is currently refined to include identified spectra of kaons, protons and anti-protons. The final results are expected to be published early next year.

Resonances Preliminary spectra of ρ^0 production in π + C interactions at 158 GeV/c have been published last year [63]. This preliminary release was limited in range of Feynman-x, x_F, between 0.3 and 0.9. Due to an improved analysis, the lower limit x_F range could be decreased to $x_F = 0$. The spectra of both the ω and K^{0*} mesons have also been determined, and the ρ^0 analysis has been performed for 350 GeV/c. The results of the updated resonance analysis are in the process of being finalised and will be published this year.

5.4.2 Cosmic-Ray Propagation and Dark Matter

Antideuterons may be generated in dark matter annihilations or decays, offering a potential breakthough in as yet unexplored phase space for dark matter. The unique strength of the search for low-energy antideuterons lies in the ultra-low astrophysical background. The dominant source of the astrophysical background is the production of antideuterons in the interactions of cosmic-ray protons with interstellar medium (predominantly H,He). However, the high production threshold and steep cosmic-ray spectrum mean that there are very few particles with sufficient energy to produce secondary antideuterons.

Part of the goals of the AMS-02 experiment on board International Space Station and the next-generation antideuteron experiment GAPS is to perform the first measurement of cosmic-ray antideuteron flux or to lower the current best exclusion limits drastically for the purpose of identifying the nature of dark matter.

Production of antideuterons and deuterons in nuclear interactions is a complex non-perturbative process. Using the NA61/SHINE data on p+p interactions at 158 GeV/c, this analysis endeavours to measure cross-section of deuteron production. Comparison of these measurements with theoretical predictions using models of coalescence between protons and neutrons will further improve the knowledge of the production mechanism. Extending the analysis techniques, a measurement of antideuteron cross-section will be helpful in limiting the astrophysical background for AMS-02 and GAPS measurements.

This analysis is performed using data collected in 2009, 2010 and 2011. Each set contains both target inserted and target removed data. Recorded events for the data sets are listed in Table 6.

Year	Target Inserted $\times 10^6$	Target Removed $\times 10^6$	Total Events $\times 10^6$
2009	3.55	0.43	3.98
2010	40.43	3.76	44.19
2011	12.93	1.18	14.11

Table 6: Yearly p+p data recorded by NA61/SHINE.

5.4.3 Identification of Low Momentum Deuterons

Energy deposition in clusters in TPCs along a track are sorted, truncated and normalized to MIP. Plotted as a function of momentum in the logarithmic bins, the dE/dx distributions show definite patterns (Bethe-Bloch curves). In the low momentum region (below 2 GeV/c), proton and deuteron regions are fairly well separated, staring at high dE/dx values and falling sharply. Pion and positron dE/dx values are low and close to MIP value. Before the proton and deuteron dE/dx lines start merging, deuterons can be identified.

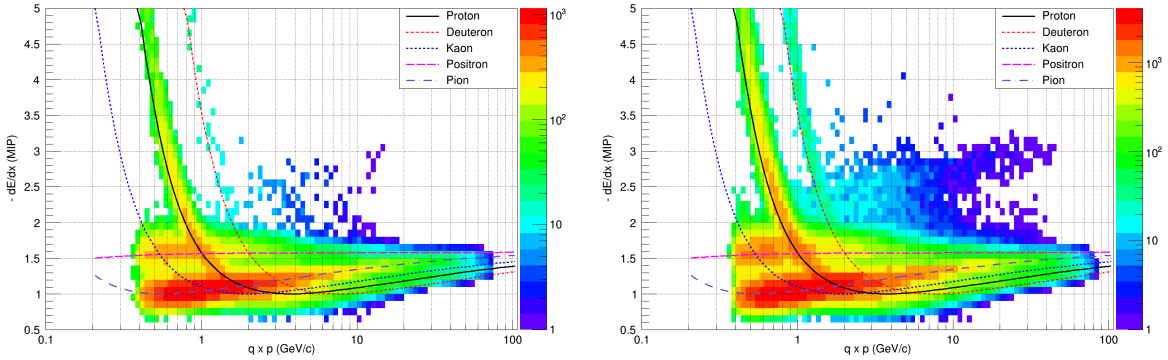

(a) (b)

Figure 50: dE/dx vs. $q * p$ for target inserted data for (a) 2009 and (b) 2010 p+p (158 GeV/c).

Figure 50 shows dE/dx as a function of $q \cdot p$ for 2009 and 2010 p+p data (158 GeV/c) after all the selections. Figure 51 shows the same plots for target removed data.

To confirm that after statistical subtraction of background form target Inserted data, dE/dx value based on Bethe-Bloch equation assuming a deuteron track is subtracted for every track. Figure 52 shows the concentration of deuteron tracks near dE/dx =0 region.

The spread comes from resolution of dE/dx and p measurements and the shift from dE/dx =0 is the result of imperfect dE/dx calibrations.

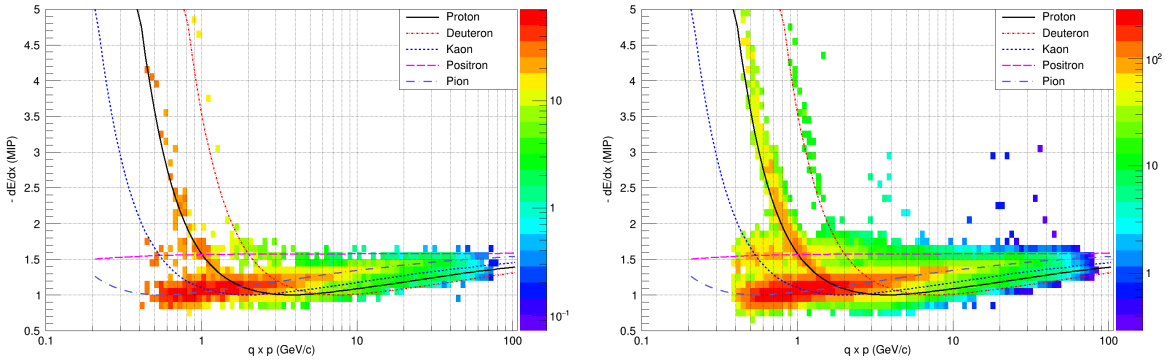

(a) (b)

Figure 51: dE/dx as a function of $q * p$ for target removed data for (a) 2009 and (b) 2010 p+p (158 GeV/c.

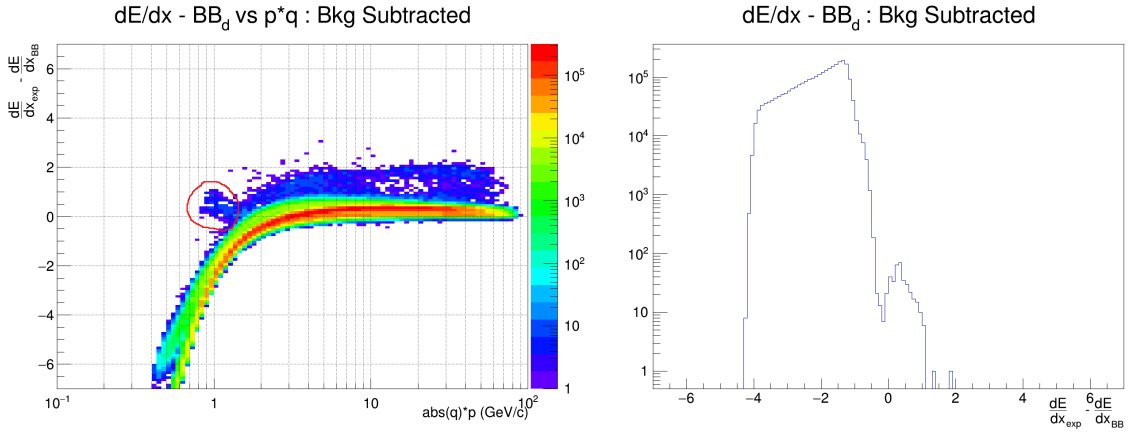

(a) (b)

Figure 52: From 2010 data : (a) re-normalized dE/dx vs. $q * p$ and (b) re-normalized dE/dx distribution.

5.4.4 Statistical Significance of Deuteron Measurement at Low p

Statistical significance of the identified deuteron measurement in the low momentum region is estimated using the technique from Ref. [64]

Let N_I and N_R be the counts of deuterons from target Inserted and Removed data respectively after all the applied selection criteria. With the normalization between target Inserted and Removed, $\alpha = t_I/t_R$ the statistical significance of the observed signal S is calculated as :

$$S = \sqrt{2}\{N_I \ln[\frac{1+\alpha}{\alpha}\frac{N_I}{N_I+N_R}] + N_R \ln[(1+\alpha)\frac{N_R}{N_I+N_R}]\}^{\frac{1}{2}} \quad (12)$$

The normalization for this analysis comes from the comparison of purely background dominated region in target inserted and target removed data. Counts of identified deuterons and the statistical significance are shown in Table 7 :

Low p Deuterons			
	2009	2010	2011
S+B	36	749	223
B	5	51	26
α	4.37	2.87	3.19
B (normalized)	22	145	83
S	14	604	140
Significance	1.1	14.5	5.4

Table 7: Deuteron counts in low momentum region and statistical significance of measurements for 2009, 2010 and 2011 p+p (158 GeV/c) data.

5.4.5 Towards Deuteron Cross-Section Measurement

Cross-sections of a particle of interest from NA61/SHINE data is calculated as follows :

$$\frac{d\sigma}{\mathrm{d}p} = \frac{\sigma_{trig}}{1 - p_{int}} \left(\frac{1}{N_I} \frac{\mathrm{d}n_I}{\mathrm{d}p} - \frac{p_{int}}{N_R} \frac{\mathrm{d}n_R}{\mathrm{d}p} \right) , \tag{13}$$

where σ_{trig} is the trigger cross-section, $N_I(N_R)$ is the number of events analyzed with target inserted (removed), dp is the width of momentum bin, $dn_I(dN_R)$ is the corrected (for acceptance and detector efficiency) number of final-state particle of interest (deuteron, for this analysis) and p_{int} is the net interaction probability, defined as :

$$p_{int} = \frac{P_T^I - P_T^R}{1 - P_T^R} , \tag{14}$$

where $P_T^I(P_T^R)$ is the trigger probability for target inserted (removed) data.

Trigger probability can be calculated as :

$$P_T^{I(R)} = \frac{N(T1 \cap T2)}{N(T1)} , \tag{15}$$

where $T1$ and $T2$ indicate, respectively, the beam and the interaction trigger.

For the 2010 p+p data, the interaction probability p_{int} was measured to be 0.02276 and uncorrected trigger cross-section was measured to be 27.23 mb. Further corrections are required for elastic and quasi-elastic contributions to calculate the proper inelastic trigger cross-section.

5.4.6 Path Forward

There has been significant progress in analysing the recorded data to identify deuterons. Identification will be improved in future by using mass-square values from Time-of-Flight detector.

For higher momentum region where identification of deuterons is difficult due to merging of Bethe-Bloch curves of different particle species, template fitting will be used to estimate the number of deuterons in various momentum bins.

As a major step toward calculating deuteron cross-section, efficiencies and geometrical acceptance factor of the detectors need to be measured. Present efforts are focused in this direction.

It is important to point out here that most event generators (PYTHIA, GEANT4, EPOS) do not allow for the production of deuterons (or anti-deuterons) as the production mechanism is poorly understood (an excellent motivation for the present analysis). Simulating p+p events will not help estimate the acceptance and efficiency of deuteron measurement. Efforts towards simulation is, of necessity, two-pronged.

Collaborators at Instituto de Fisica, UNAM in Mexico, especially Ph.D. candidate Diego Gomez Coral, have been working towards comparing (non-perturbative) model dependent calculations of proton and anti-proton cross-sections to data. This enables one to estimate model-dependent predictions of deuterons production. The best estimates of such deuteron cross-sections will be used to simulate weighted spectra of deuterons through NA61/SHINE GEANT description and to estimate the relevant acceptance and efficiency factors.

The entire analysis technique can be used for antideuteron production measurements, an enticing possibility with the present amount of available p+p data at 158 GeV/c. Similar data from future NA61/SHINE runs will be immensely helpful in measurement of antideuteron cross-sections as it is a particularly rare and therefore statistically starved process.

6 Proposed run schedule

The revised NA61/SHINE data-taking plan is presented in Table 8. Following the current accelerator schedule the plan assumes that the data-taking with a primary Xe beam will take place in 2017 and with a Pb beam in 2018. It is also assumed that hadron beams will be available for several months in 2017 and 2018 until the Long Shutdown 2.

Figure 53 schematically illustrates the status and plans for data-taking within the NA61/SHINE (beam momentum)-(system size) scan.

The 2017 beam request is explained as follows:

(i) 21 days of h^+ beam at 400 GeV/c are needed for the installation and testing of the facility upgrades: Forward-TPCs, Vertex Detector, SciFi Beam Detectors, PSD and DRS4 read-out.

Beam		Target	Momentum	Year	Days	Physics
Primary	Secondary		(A GeV/c)			
p			400			
	h^+	A	40-400	2017	21 days	installation/tests
p			400			
	p	Pb	30, 40	2017	28 days	SI
p			400			
	h^+	A	30–120	2017	42 days	ν
Xe		La	13, 19, 30, 40, 75, 150	2017	60 days	SI
p			400			
	p	Pb	13, 20	2018	28 days	SI
p			400			
	h^+	A	30–120	2018	42 days	ν
Pb		Pb	20, 40, 75, 150	2018	60 days	SI

Table 8: The NA61/SHINE data taking plan revised in 2016. The following abbreviations are used for the physics goals: SI – measurements for physics of strong interactions, ν – measurements for the Fermilab neutrino beams.

(ii) 28 days of proton beam at 30 and 40 GeV/c are needed for data-taking on p+Pb interactions.

(iii) 42 days of h^+ beam at 30–120 GeV/c are needed for data-taking for the Fermilab neutrino beams.

(iv) 60 days of Xe beam at 13A, 19A, 30A, 40A, 75A and 150A GeV/c are needed for data-taking on Xe+La collisions.

7 Ideas to Extend the NA61/SHINE Physics Program

The approved data-taking programme for NA61/SHINE should be completed by the end of 2018. The collaboration is now considering possible continuation of measurements after Long Shutdown 2. This would require a significant upgrade of the NA61/SHINE facility.

The planned measurements are motivated by questions and requirements coming from communities working on physics of strong interactions and neutrino physics.

The new measurements for physics of strong interactions aim to resolve the long-lasting tension between statistical and dynamical models of multi-particle production in high energy collisions. They shall include precise measurements of open charm

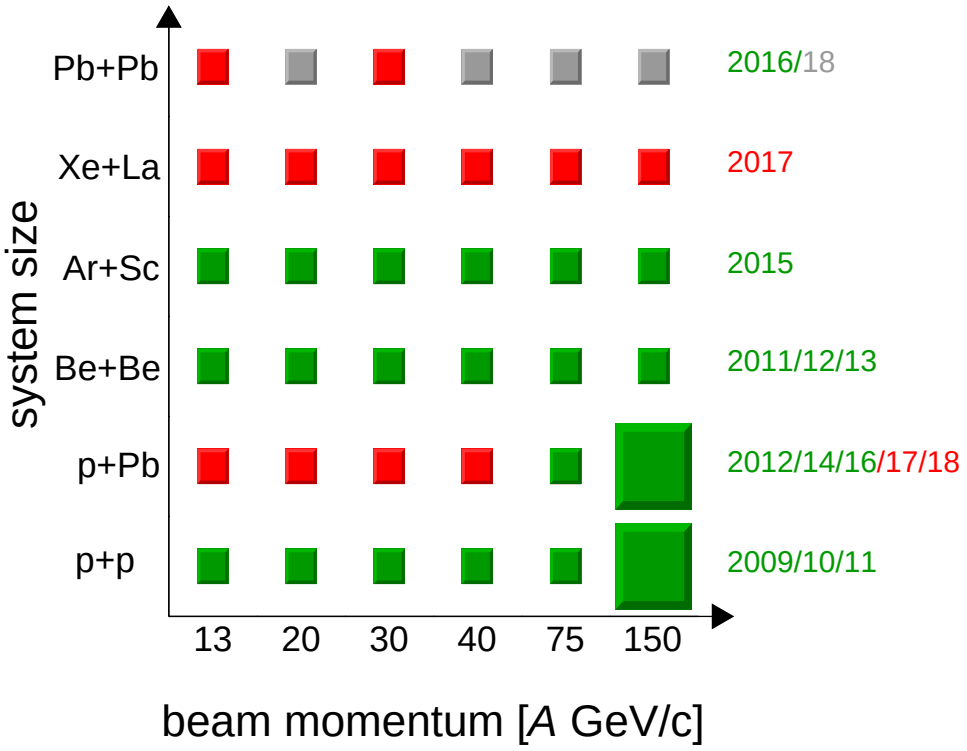

Figure 53: The NA61/SHINE data taking schedule for the (beam momentum)-(system size) scan and its proposed extension for the period 2016–2018 (in gray).

and multi-strange hyperon production, measurements of cumulative hadrons as well as measurements of fluctuations and correlations in the full phase space. In particular, systematic measurements of open charm production together with already existing data on J/ψ mesons by the NA38, NA50 and NA60 experiments at the CERN SPS should allow to finally distinguish between statistical and QCD-inspired models of J/ψ and open charm production in heavy ion collisions.

The new measurements for neutrino physics will include precise measurements of hadron emission from a replica target of the Long-Baseline Neutrino Facility (LBNF) at Fermilab required for the Deep Underground Neutrino Experiment (DUNE). The NA61/SHINE measurements with thin and replica targets for T2K demonstrated a need for precise data on hadron productions from the surface of targets of future long-baseline neutrino oscillation experiments, e.g. DUNE and Hyper-K. The design of DUNE targets (DUNE considers to use different targets for low and high energy tunes) will not be fixed before 2020. Thus the required measurements can be performed only after the LS2.

The new programme requires improvements of the beam quality and an increase of the beam intensity in the H2 beam line as well as major upgrades of the detector, which would include an extension of the operation time of existing detector components.

The work on improvements of the beam quality, which is relevant for the ongoing measurements of NA61/SHINE and other users of the SPS beams, has been already started by the BE and EN Departments. In particular, the 50 Hz oscillations of the beam intensity during the spill should be removed/reduced by the active compensation system introduced in 2016 . Additionally, in 2017 the regulation of the SPS main power supplies will be changed. Finally, observed changes of the beam position on the NA61/SHINE target are likely caused by malfunctioning power supplies in the H2 beam line and the problem should be identified and fixed in the near future. After the LS2 NA61/SHINE would need ion beam intensities up to 10^6 ions per spill, a factor of about ten increase in comparison to the currently used beam intensities. This may require an upgrade of the H2 beam line and NA61/SHINE detector radiation protection.

The new program requires major detector modifications, namely:

1. target and side-backward tracking system (to be designed and constructed) should be located inside the VTX-1 magnet,
2. the read-out rate should be increased to about 1 kHz,
3. a Large Acceptance Vertex Detector should be designed and constructed,
4. new Time-of-Flight detectors should be designed and constructed,
5. precise tracking system along the DUNE target(s) should be designed and constructed.

The work on the new set-up design and optimization has started. Simulations are performed within the SHINE Monte Carlo framework based on GEANT4. The detector after the LS2 may look similar to the one presented in Fig. 54.

It is considered to base the new detectors and upgrades of the existing ones on well established detector technologies and heavily use synergy between NA61/SHINE and other experiments, in particular ALICE. The read-out rate of the existing TPC can be increased to 1 kHz by re-using the ALICE TPC read-out electronics which ALICE plans to replace during the LS2. Also sensors developed by ALICE for the ITS upgrade could be use by NA61/SHINE to construct the side-backward detector and Large Acceptance Vertex Detector. Under discussion is construction of the new ToF detectors based on mRPC modules being developed for the MPD detector at the JINR NICA. In addition, the existing beam position detectors should be replaced by the SciFi ones which are under tests within NA61/SHINE.

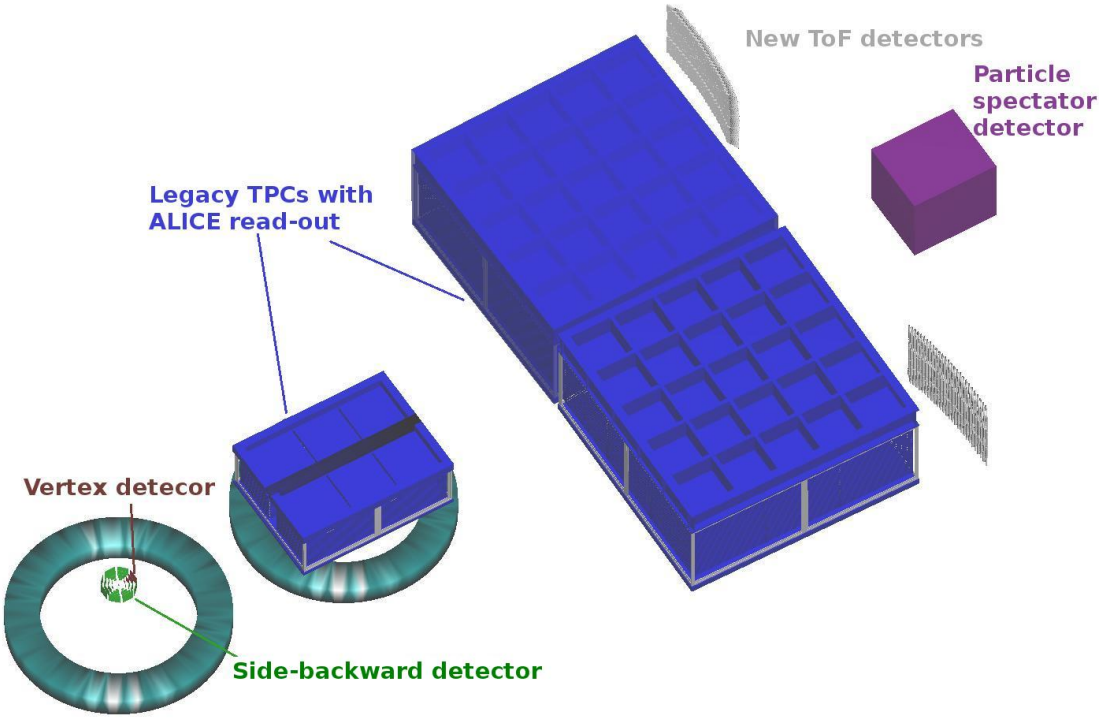

Figure 54: A first proposal of the NA61/SHINE set-up for measurements beyond 2020.

8 Summary

The summary of this report is as follows:

(i) Recorded data (see Section 2):

Failure of the VERTEX-1 superconducting magnet lead to postponing the data taking planned for autumn 2015 to autumn 2016: data for Fermilab neutrino beams, data on p+p interactions at 400 GeV/c and on Pb+Pb collisions. The data taking was started in September 2016. The beam time in 2015 was used for total cross-section measurements in hadron-nucleus interactions and for detector tests. The detector tests were performed also in May and July 2016. During the latter period data on p+Pb interactions at 80 GeV/c and p+C at 60 GeV/c were recorded.

(ii) Facility modifications (see Section 3):

(a) In September 2015 VERTEX-1 failed. A new Magnet Safety System was installed for both VERTEX-1 and VERTEX-2. Tests revealed VERTEX-1 was not damaged in the incident. Both magnets operate properly since July 2016.

(b) The Projectile Spectator Detector was upgraded and its parameters were optimised for the data taking with Xe and Pb beams: a new central module was added and new photodiodes in the central modules were installed. The efficiency of the air cooling system was improved by addition of vortex tubes.

(c) Tests of Small Acceptance Vertex Detector were conducted. Full detector will be tested on the Pb beam in November/December 2016.

(d) Forward-TPC 1 assembly and installation in the beam are planned before the end of 2016.

(e) Tests of a small system of the new readout electronics is planned before the end of 2016 and mass production is to be started in 2017.

(iii) Software modifications (see Section 4):
The most important achievements associated with the upgrade program of the NA61/SHINE software are:

(a) the S$\underline{\text{HINE}}$ reconstruction chain was validated against the "legacy" chain, together with the Monte-Carlo,

(b) the Collaboration uses CERN OpenStack service to host all infrastructure service

(c) the transformation process from SVN to GitLab repository has been started

(d) detector response simulation in the S$\underline{\text{HINE}}$ Monte Carlo chain has been validated

(e) global track reconstruction in the S$\underline{\text{HINE}}$ software including the new detectors has been started

(iv) Numerous new physics results, final and preliminary, were released, see Section 5. They include:

   (a) inclusive spectra of negatively charged pions and their mean multiplicity in central Ar+Sc collisions at 13A-150A GeV/c,

   (b) charged hadron multiplicity and multiplicity - (transverse momentum) fluctuations in central Ar+Sc collisions at 13A-150A GeV/c,

   (c) higher moments of charged hadron multiplicity distribution in inelastic p+p interactions at 20-158 GeV/c,

   (d) Λ hyperon spectra in inelastic p+p interactions at 40 GeV/c,

   (e) inelastic and production cross section for ^{7}Be+^{9}Be collisions at 13A-150A GeV/c,

   (f) high precision spectra of charged pions from the surface of the T2K replica target exposed by protons at 31 GeV/c,

   (g) production cross section for K^{+}+C interactions at 60 GeV/c,

   (h) evidence for deutron production in inelastic p+p interactions at 158 GeV/c.

(v) The data-taking plan for 2017 and 2018 (see Section 6) includes runs with primary Xe and Pb beams as well as secondary hadron beams needed for measurements for strong interaction and neutrino physics.

(vi) Ideas on NA61/SHINE measurements beyond 2020 are briefly summarized and include measurements for strong interactions and neutrino physics.

Acknowledgments

We would like to thank the CERN EP, BE and EN Departments for the strong support of NA61/SHINE.

This work was supported by the Hungarian Scientific Research Fund (grants OTKA 68506 and 71989), the János Bolyai Research Scholarship of the Hungarian Academy of Sciences, the Polish Ministry of Science and Higher Education (grants 667/N-CERN/2010/0, NN 202 48 4339 and NN 202 23 1837), the Polish National Center for Science (grants 2011/03/N/ST2/03691, 2013/11/N/ST2/03879, 2014/13/N/ST2/02565, 2014/14/E/ST2/00018, 2014/15/B/ST2/02537 and 2015/18/M/ST2/00125), the Foundation for Polish Science — MPD program, co-financed by the European Union within the European Regional Development Fund, the Federal Agency of Education of the Ministry of Education and Science of the Russian Federation (SPbSU research grant 11.38.242.2015), the Russian Academy of Science and the Russian Foundation for Basic Research (grants 08-02-00018, 09-02-00664 and 12-02-91503-CERN), the Ministry of Education, Culture, Sports, Science and Technology, Japan, Grant-in-Aid for Scientific Research (grants 18071005, 19034011, 19740162, 20740160 and 20039012), the German Research Foundation (grant

GA 1480/2-2), the EU-funded Marie Curie Outgoing Fellowship, Grant PIOF-GA-2013-624803, the Bulgarian Nuclear Regulatory Agency and the Joint Institute for Nuclear Research, Dubna (bilateral contract No. 4418-1-15/17), Ministry of Education and Science of the Republic of Serbia (grant OI171002), Swiss Nationalfonds Foundation (grant 200020117913/1), ETH Research Grant TH-01 07-3 and the U.S. Department of Energy.

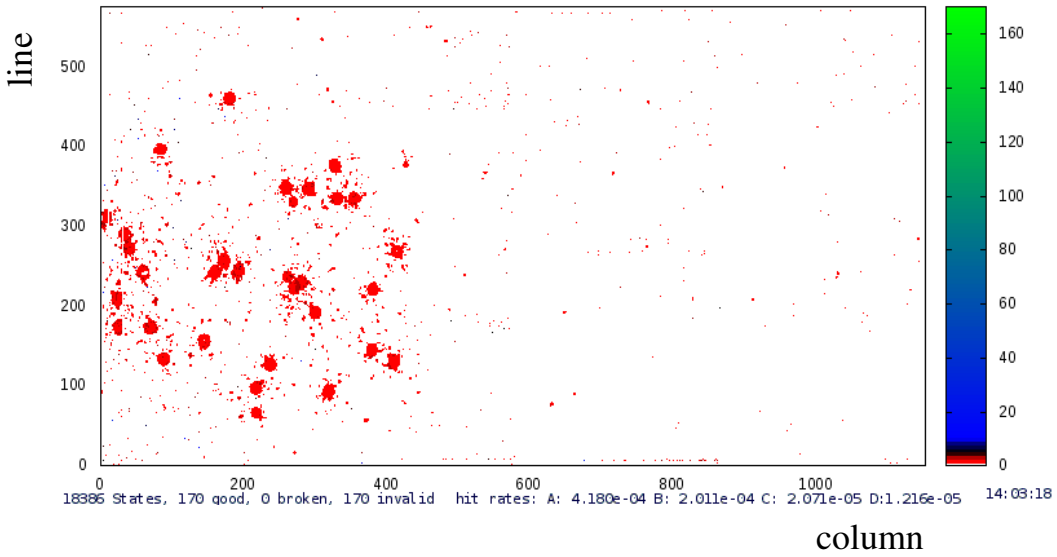

Figure 55: Beam Pb ions at 30A GeV/c captured in the MIMOSA-26 sensor. Exposition time was about 1 ms. Clusters created by Pb ions passing through the sensor contain about 200 pixels.

A Vertex Detector: Tests on Beam, Integration, Hardware Upgrades and Software

A.1 Analysis of data collected during November 2015 and July 2016 test.

In 2015 the NA61/SHINE Vertex Detector program reached a phase of prototyping and beam tests. The first test of one MIMOSA-26 sensor was performed in November 2016 using Pb beam at 30A GeV/c. The main motivation of this measurement was the test the resistivity of MIMOSA-26 sensor to the heavy ion beam in regards to the latch-up effects. During the test we were able to monitor the power consumption on the analog and digital sections of the sensor by measuring the related currents. We started the measurement with the tested sensor located at the distance of 10 mm from the beam spot (here we refer to the distance between the beam spot and the sensor closest edge). This distance was gradually decreased and the last data were taken with the sensor exposed directly to the beam spot. Figure 55 shows response of the sensor to the illumination by the Pb relativistic ions for the integration time of 100 ms. The sensor was kept exposed to the beam continuously for 24 hours and during this time tree latch-up cases have been observed by the persistent increase of the digital and analog currents by 10–30 μA. After each latch-up a power cycling was able to return the sensor to its normal operation. The DAQ system used during the test was equipped with the latch-up protection system (see more details in Sec. A.2), however the currents induced by the observed latch-up

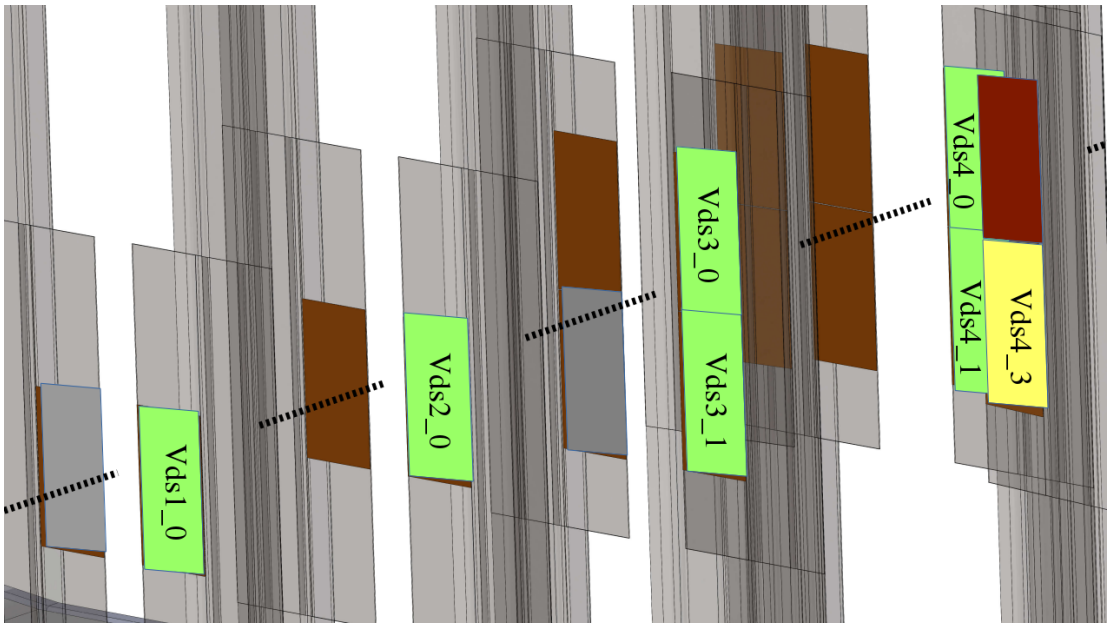

Figure 56: Layout of sensors (in green) used during the July 2016 test.

were to low to activate the system. Accordingly to the above observation we re-tuned the current thresholds used by the latch-up protection system.

In July 2016 the integrated detector was transported to CERN and installed in the NA61/SHINE experimental area for the test on beam of protons at 150 A GeV/c. The construction of the start version of vertex detector call Small Acceptance Vertex Detector (SAVD) was described in Ref. [5]. In the July test we used six sensors installed on one arm of Vertex Detector. The number of sensor was sufficient to verify the ability of track reconstruction in SAVD and the ability SAVD data correlation with other sub systems of the standard NA61/SHINE experimental set-up (beam detector, TPCs), as well as to test the performance of the basic subsystems of the detector which were:

(i) mechanical support,

(ii) readout system,

(iii) cooling system,

(iv) gas flow system including the helium enclosure box.

The picture of integrated sensors on the carbon fibre ladders installed in the arm of SAVD can be seen in Fig. 7. The integration technology with the related aspects like sensors performance after full integration is described in details in Sec. A.3.

The layout of sensors with the naming convention used during the test is depicted in Fig. 56. The synchronization of the SAVD data with central NA61/SHINE DAQ system was obtained by coding the arrival time of the central DAQ trigger to the SAVD DAQ

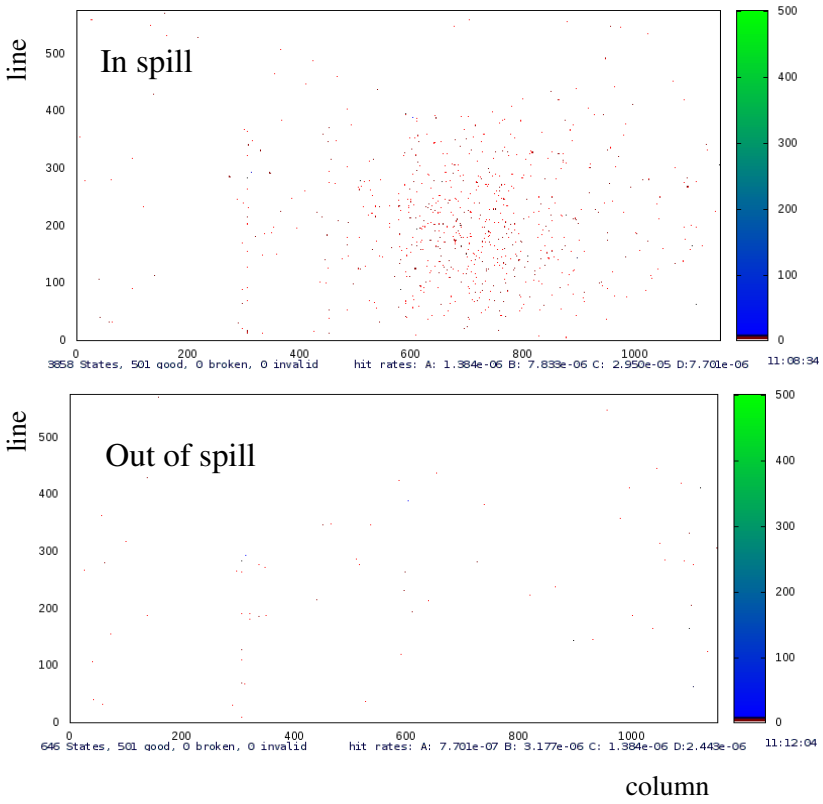

Figure 57: Example of sensor response to beam particles *(top)*. For comparison we show data collected in the same sensor, over the same period of time, but during the brake time between beam spills *(bottom)*.

data stream. The VD DAQ set-up and its integration with central NA61/SHINE DAQ system is described in details in Sec. A.4. During the test the sensors were kept in helium enclosure. The temperature of the circulating water used for cooling of sensors was set to 10°C and stabilized using HUBER thermostat. The elements of the cooling system and tubes coupling the system with the tubes integrated on ladders can be seen in Fig. 7. The prevention against water condensation on sensors, ladders and on the inner support structure was ensured by the helium enclosure.

To demonstrate the data correlation between sensors we exposed them directly to the beam particles. Figure 57 compares raw data collected in sensor $Vds1$-0 in the period when the beam was hitting the sensor (*top*) and during the break between two spills (*bottom*). The qualitative difference is clearly seen with appearance of pixel clusters produced by particles in the left figure lading the creation of the beam spot image. Cluster recognition procedure have been applied to reconstruct clusters and convert them to particles hits. The hit positions was taken as a cluster center of gravity.

In order to study the correlated response of tree sensors to passing particles we in-

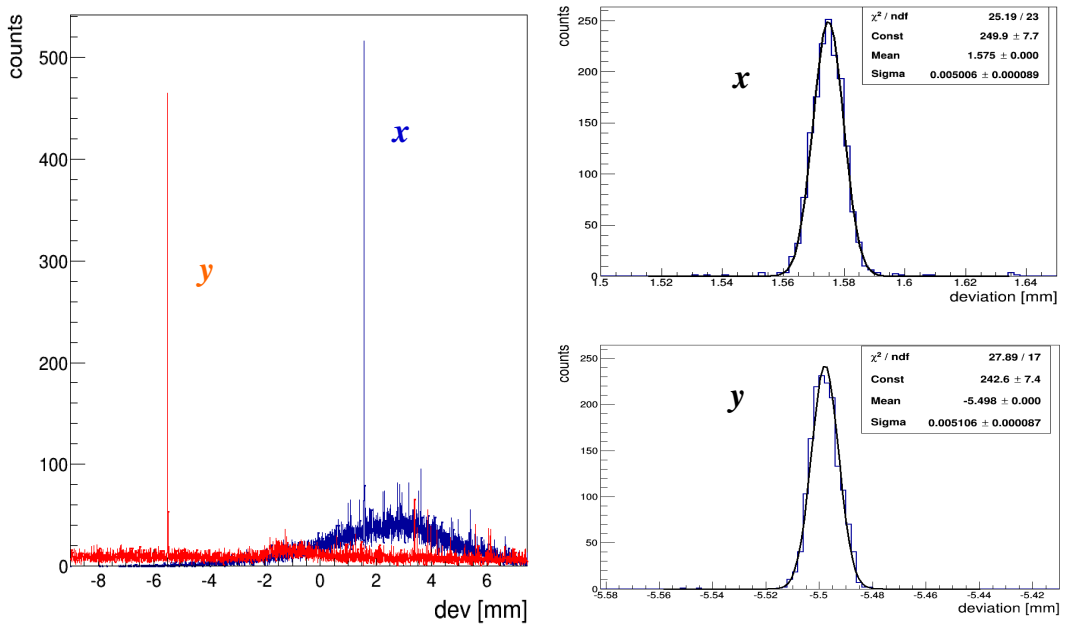

Figure 58: *Left:* distributions of dev_x (blue histogram) and dev_y (red histogram) for all tree hit combinations in sensors Vds1-0, Vds2-0 and Vds3-0. *Right:* distributions of dev_x *(top)* and dev_y *(bottom)* after applying $\pm 3\sigma$ cuts on dev_y and dev_x peaks, respectively.

troduced the measures dev_x and dev_x defined in the following way:

$$\mathrm{dev}_x = \frac{x_1 + x_3}{2} - x_2\,, \qquad \mathrm{dev}_y = \frac{y_1 + y_3}{2} - y_2\,,$$

where x_1, x_2 and x_3 (y_1, y_2 and y_3) refer to horizontal (vertical) coordinates of particle hits measured in sensors located on tree consecutive stations. The distributions of dev_x (blue histogram) and dev_y (red histogram) for all tree hit combinations in sensors Vds1-0, Vds2-0 and Vds3-0 are drawn in Fig. 58 (*left*). The well visible spikes on the large combinatorial background refer to peaks generated by passing beam particles. Because dev_x and dev_y are correlated for the same track, cutting on simultaneously on dev_x and dev_y allows for clear extraction of particle correlated components. This is illustrated in Fig. 58 (*right*) where distributions of dev_x and dev_y have been drawn after applying $\pm 3\sigma$ cuts on dev_y and dev_x, respectively. A straight line fitted to the related hits from tree stations can be associated with a reconstructed track. It turn out that dev_x and dev_x are sensitive to the relative rotations of sensors. This feature allowed to correct for the relative rotation of sensors. One can expect that, if x and y axes of all tree sensors are aligned then the widths of dev_y and dev_x distributions reach their minimum values. It is illustrated in Fig. 59. The figure shows dependency of the effective single sensor position resolution as a function relative rotation (around z axis) of Vds4-1 sensor in respect to Vds2-0 and Vds3-1. As one can see the best resolution is reached for the same

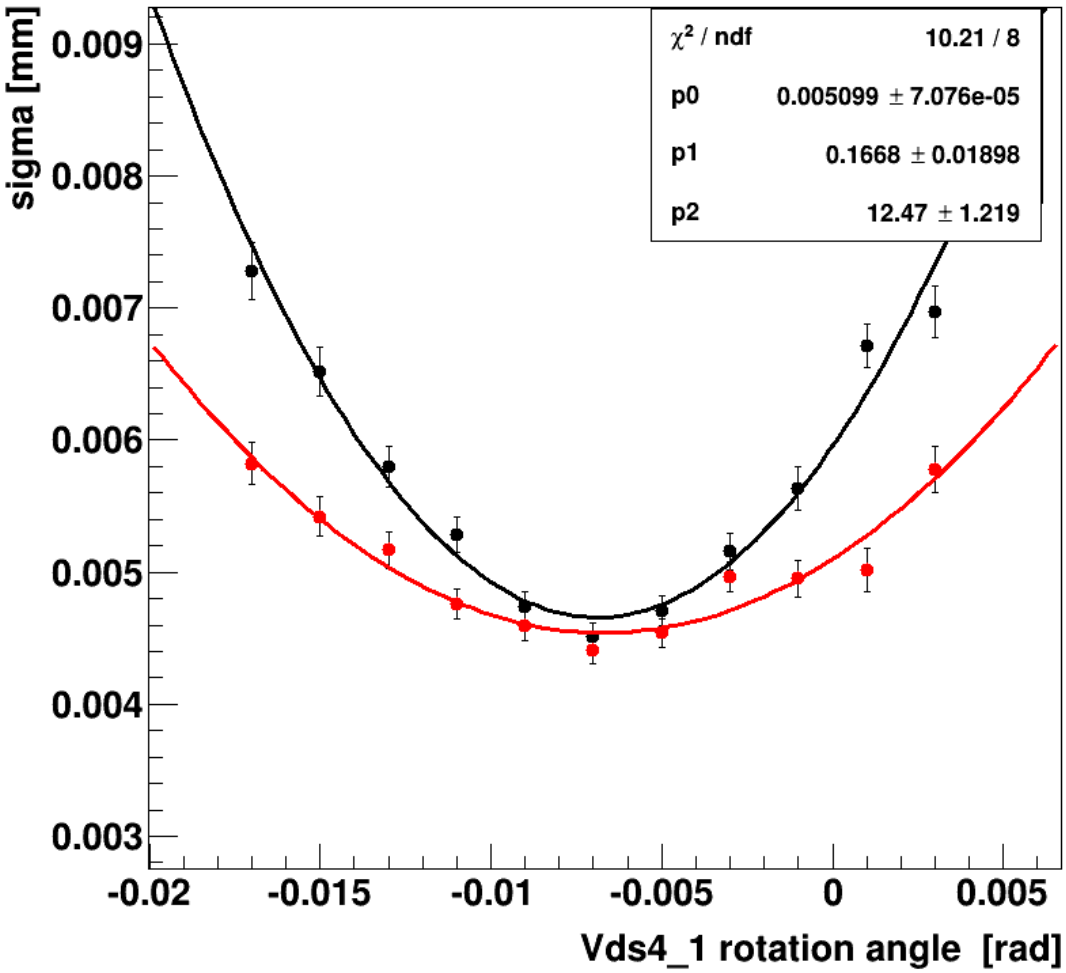

Figure 59: Dependency of the effective single sensor position resolution in x *(black dots)* and y *(red dots)* direction as a function of the relative rotation around z axis of $Vds4$-1 sensor in respect to $Vds2$-0 and $Vds3$-1.

rotation in both x and y direction. We applied the rotation tuning procedure to all the sensors, the results are collected the Tab. 9. Having all sensors x and y axes aligned

sensor	$Vds1$-0	$Vds2$-0	$Vds3$-0	$Vds3$-1	$Vds4$-0	$Vds4$-1
rotation [mrad]	9	0	0	0	-9.4	-6.8

Table 9: Rotation of sensors in respect to the z axis to be applied to align their x and y axes.

the system was ready to applied corrections to the transverse positions of sensors. The corrections were found from analysis of dev_x and dev_y distribution offsets for four different combinations of sensors, namely for $Vds1$-0, $Vds2$-0 and $Vds3$-0, $Vds2$-0, $Vds3$-0

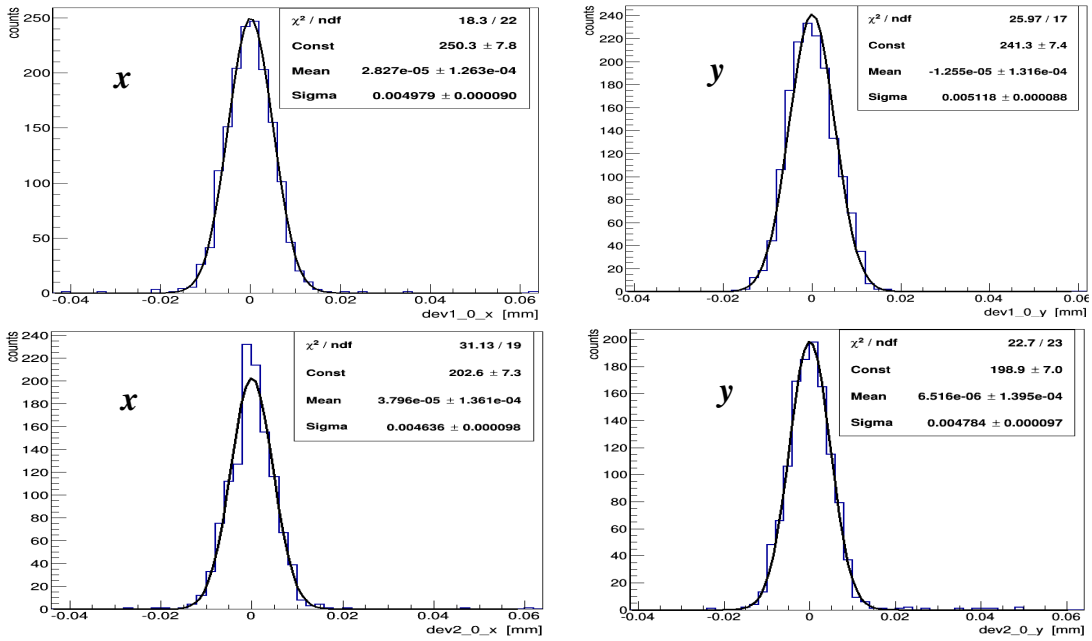

Figure 60: dev$_x$ and dev$_y$ distributions for 2 different combinations of sensors (see text) after tuning the sensor geometry.

and *Vds*4-0, *Vds*1-0, *Vds*2-0 and *Vds*3-1 and *Vds*2-0, *Vds*3-1 and *Vds*4-1. We tested, that after applying the correction to all sensors, the dev$_x$ and dev$_y$ distributions for the mention combination of sensors have been centered at 0. This is illustrated in Fig. 60 for *Vds*1-0, *Vds*2-0 and *Vds*3-0 (top panels) and *Vds*2-0, *Vds*3-0 and *Vds*4-0 (bottom panels) sensor combinations.

After geometry tuning the analysis focused on reconstructed track properties. Left panels Fig. 61 show distributions of x and y slopes of reconstructed tracks when the sensors were exposed directly to the beam particles. For both x and y coordinates a very narrow peaks are seen with $\sigma \approx 0.23$ mrad, that refers to the angular distribution of the beam particles. The shifts of maxima of the distributions from 0 reflect precision of SAVD detector positioning on the supporting platform. In contrary, on right panels of Fig. 61 the distributions of x and y slopes of the reconstructed tracks produced on 2 mm Pb target were drawn. The target was installed 5 cm upstream the Vds1 station. Red and blue histograms refer to two different combinations of sensors (see figure caption) which are up-down symmetric which is reflected in y-slope distribution. As expected for particles produced on target, in Fig. 61 rather broad distributions limited only by sensors acceptance are observed. For events with more then one reconstructed track it is possible to reconstruct the primary interaction point. Figure 62 shows longitudinal coordinate (*left*) and transverse coordinates (*right*) distributions of the two track closest proximity points. Position of Vds1 and Vds2 stations were indicated by the arrows. In the longitudinal distribution one can clearly see the reconstructed target profile (at ≈ -50 mm) while the transverse distribution shows the intersection of the beam spot

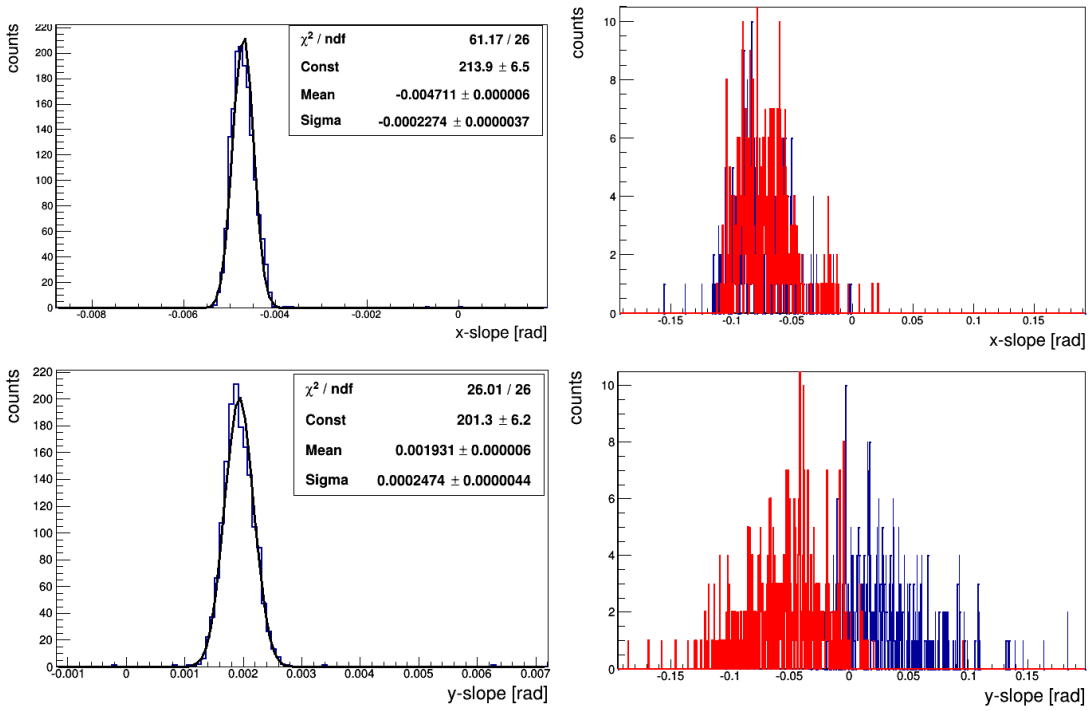

Figure 61: Angular distributions of the beam particles *(left panels)* and particle produced in hadronic interactions on Pb target *(right panels)*. Different histogram colors refer to different sensor combinations used in track reconstruction: $Vds2$-0, $Vds3$-0 and $Vds4$-0 *(blue)* and $Vds2$-0, $Vds3$-1 and $Vds4$-1 *(red)*.

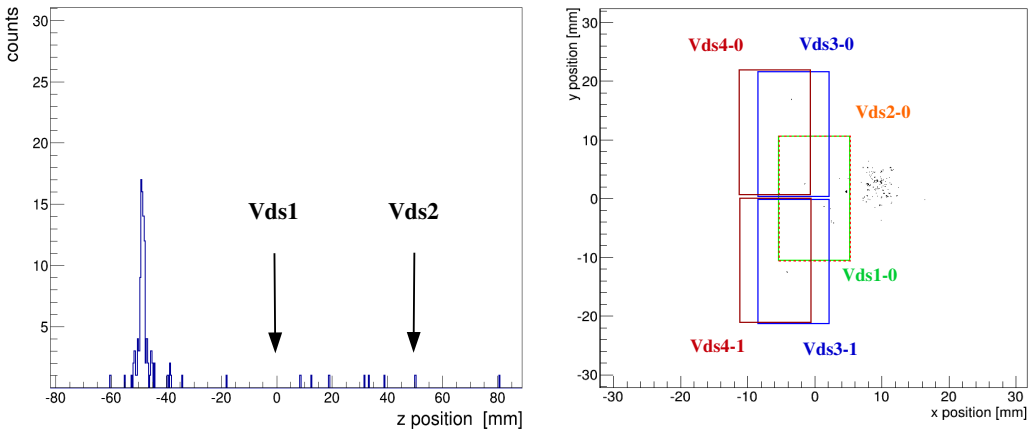

Figure 62: Reconstructed primary interaction points in lead target in the longitudinal direction (*left*) and in the transverse plane (*right*). Position of Vds1 and Vds2 stations were indicated by the arrows. The rectangular boxes show the active areas of the indicated sensors.

with Pb target. The rectangular boxes representing the active areas of all sensors used in analysis were indicated to show the relative distance between tracks and the sensors in the transverse plane.

The presented analysis demonstrated the ability of the detector to reconstruct tracks with expected position resolution of about 4 μm and the ability of the primary vertex reconstruction. The analysis is ongoing and in the next steps we plan to perform track reconstruction in the magnetic field using all four VD stations as well as demonstrate feasibility of matching the tracks reconstructed in SAVD with the tracks reconstructed with VTPC-1 and VTPC-2.

A.2 Latch-up protection and new firmware on TRBv3

As a part of preparations for the beam test in July some modification of hardware and software have been done. For the peripheral FPGA chips located the TRB3 board new firmware was prepared. The new firmware allows to count triggers arriving from central DAQ system directly on TRB3 board. This feature is an important part for the VD DAQ and central DAQ synchronization mechanism. The values of trigger counter are stored in header section of sensor data field. In addition, the peripheral FPGAs have ability to reset counter via signal from DAQ. Trigger and Reset signals are provided through the Converter Board version 2013 (CB).

In order to introduce the latch-up protection system the procedures for external interrupt handling were added in the microcontroler STM32F103RC located on the CB. These interrupts are generated by comparators responsible for current monitoring on the sensor power supply lines (digital and analog parts). The threshold values of power supply currents were set as maximum current consumption observed increased by 10 mA, namely, to 120 mA for the digital part and to 185 mA for the analog part. During the tests of latch-up protection mechanism we discovered, that the protection system is spontaneously activated just after powering the sensor. We have investigated stability of the voltages on CB. It turn out, that all outputs of DACs (LTC2620) have oscillations with amplitude at the level of tens mV and the frequency few MHz. In addition, at the outputs of all current monitors (ZXCT1022) the spikes with amplitude of hundreds of mV were encountered. To resolve this problems the values of capacitors at outputs of DACs were changed from 100 nF to 1 nF, and the extra 100 nF capacitors were added at the output of the chip. This modifications increased the reaction time of the protection system to 3 ms making it insensitive to the high frequency components.

In future more detailed study of the oscillation spectrum will be performed which eventually will allow to used more selective filtering and keep the the latch-up protection system reaction time as short as possible.

A.3 Current status of sensor integration

Construction of SAVD based on MIMOSA-26 sensors and ALICE ladders has started in spring 2016 at the Institute of Nuclear Physics (IKF) of the Goethe-University Frankfurt am Main. Each unit is composed of one or two 50 µm thin MIMOSA-26 sensors, a so called Carbon Fibre Extension Plate (CFEP)[4], a Flex-Print Cable (FPC)[5] and a single ALICE ladder used for its inner tracking system upgrade. Each unit is named the same way as the FPC it hosts.

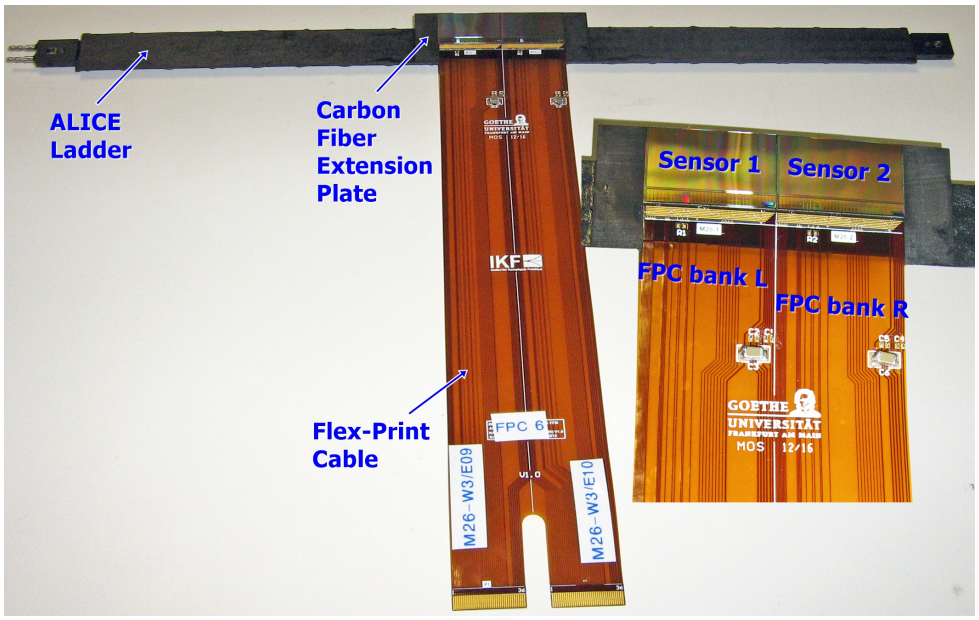

Figure 63: Single SAVD unit composed of two MIMOSA-26 sensors, carbon fibre extension plate, flex-print cable and an ALICE ladder.

Until May 2016 the units needed to accomplish the three first (downstream the target) SAVD arms were fully integrated and delivered to Krakow SAVD Team. Some days after delivery it was reported that some sensors became malfunctioning despite they were tested after each major integration step that is after wire bonding, then after bond encapsulation (both done on stand-alone extension plates) and after gluing the CFEP to the ALCIE ladders, see Fig. 64.

In the mean time, one more unit was constructed at IKF and some days after a malfunctioning sensor was also observed there. After that observation, the wire bond

[4]Each extension plate is composed of three 80 μm thin carbon fibre sheets oriented with respect to each other by 90°

[5]Each FPC features two independent sets of traces/banks needed to operate sensors, see also fig. 63. These sets are called "L" and "R", to distinguish between the sensor localized on the Left and the Right side of the cable.

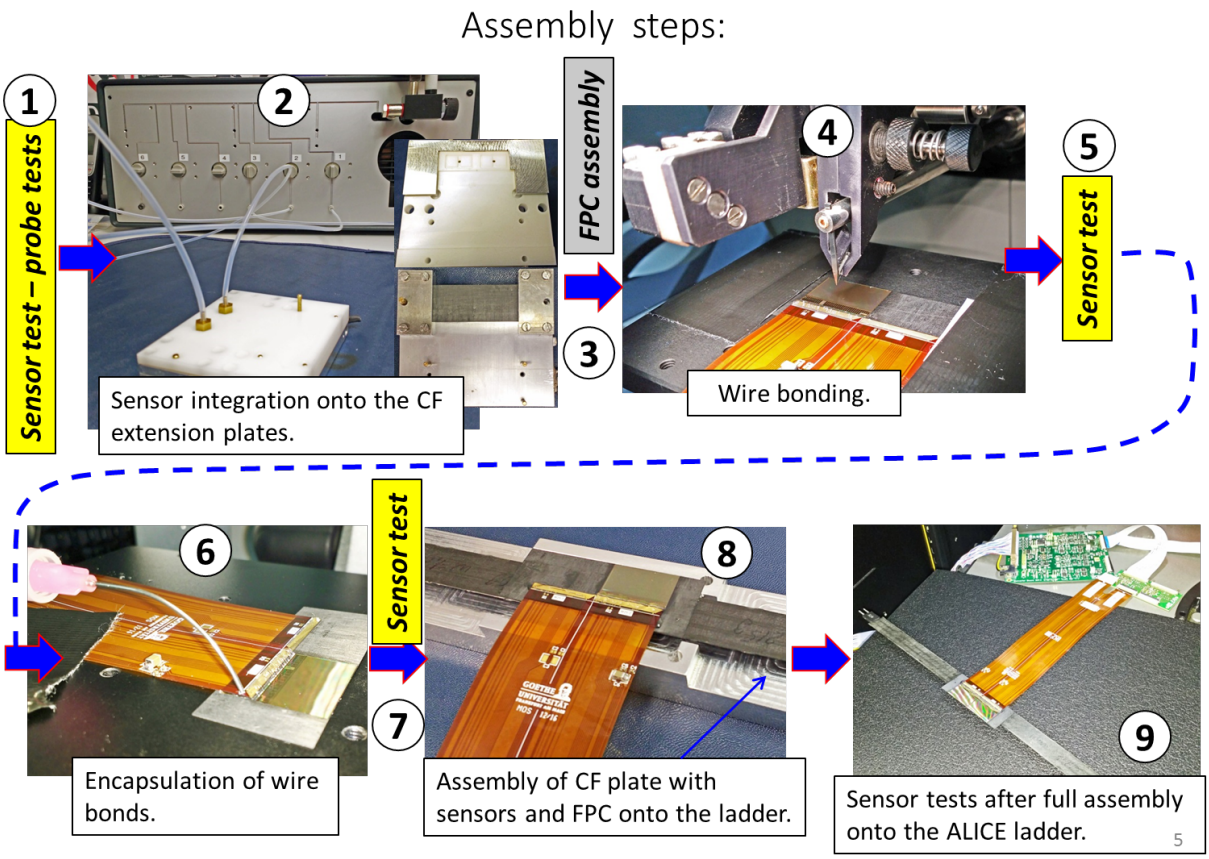

Figure 64: Single SAVD unit composed of two MIMOSA-26 sensors, a carbon fibre extension plate, a flex-print cable and an ALICE ladder.

encapsulation step was abandoned. The remaining units were constructed and transported to CERN without the encapsulation glue. Those units did not exhibit any malfunctioning sensors.

The IKF team has investigated possible origins of the sensor malfunctioning. Here the following observations were take into account:

(i) Transport: Excluded

(ii) Encapsulation: Procedure routinely used at IKF with 100% yield

(iii) Bonding: Exceptional long wires due to the level differences between the sensor (50 µm) and FPC (about 1.5 mm)

(iv) Bonding: Pull-tests revealed a different wire-bond breaking force for a uniform feet pattern that was meeting industrial requirements. This is a sign of FPC r AlSi wire material non-uniformities

(v) Bonding hardware: Wire was some years old (Al Si 1% wire becomes locally harder with time).

(vi) Bonding hardware: Machine makes uniform bonds

(vii) Bonding hardware: Heavily used wedges

To improve the quality of the bonding hardware, IKF purchased new a bonding wire and wedges. Then the encapsulation adhesive was ripped-off from the malfunctioning sensors together with wire bonds. This operation required special care and time to avoid ripping-off the aluminium bonding pads on the sensor side. When all bonds and encapsulate were removed, the new bonding was applied. Unfortunately, due to the FPC design (too narrow bonding pads) it was impossible to apply more than one bond per each sensor steering signal. It is advised to provide such redundancy for both flex-print cable and sensors of the future NA61 Vertex Detector.

This reparation work allow to recover all the malfunctioning sensors successfully. At the moment the SAVD can be equipped with 15 fully working sensors. Therefore we need to provide one more unit to accomplish both arms of the SAVD and account for some spares as well. The discussion with the sensor provider (IPHC-Strasbourg) is ongoing.

A.4 DAQ integration

SAVD readout design assumes separation of low level data acquisition from Central DAQ. Low Level data accumulated in TRBv3 FPGAs are sent as UDP packets through gigabit ethernet to the low level DAQ machine. Two streams of data consisting of data frames come through the gigabit ethernet switch to dedicated network interface. Data are acquired continuously as in trigger-less systems, so there is continuous stream of data coming from TRBv3 to low level DAQ computer. For integration with Central DAQ, trigger information is crucial for synchronization. The main trigger signal from NA61/SHINE comes by signal level converter to the converter boards and then it is processed by FPGAs with modified firmware. Frames originating from first FPGA are tagged in time-stamp field with trigger counter value.

In the initial version on the Low Level DAQ machine two processes originating from HADES were involved: daq_netmem and daq_evtbuild. A pair for the readout of one TRBv3, so 4 processes for full readout from two TRBv3. The daq_netmem process purpose is to readout the raw data coming from TRBv3 and put them to the shared memory region. The daq_evtbuild process goal is to read frames from shared memory region, check frames, append headers to them and save or send the data to provided storage unit.

The set-up of 2 TRBv3 being read by single PC was not used previously, so first there was a need to test such a set-up if it will work with full performance. A bunch of scripts were prepared to configure double set-up and acquire data in standalone mode. Tests revealed that it is possible to run in double configuration.

Integration with Central DAQ goals are providing filtered data from both TRBv3 units and put them on to NA61/SHINE specific internal data format called BOS banks. Filtering means that only 5 consecutive frames after the new trigger signal appears are

allocated for sending to Central DAQ. The daq_evtbuild process was modified to prepare such frames and to send them by socket to the prepared low level DAQ server software "na61vddaq". The purpose of low level DAQ server is to aggregate data frames from both TRBv3 units, pack them in BOS banks and send them to Central DAQ.

During the June tests, na61vddaq was tested synthetically and proved to work. Test of integration with Central DAQ was not possible during that time because Central DAQ readout system needed extensive and careful modifications to include the TCP/IP readout parallel to other readout systems. Also Central DAQ readout was finally prepared in push data mode as other detectors readout which is contradictory to the initial na61vddaq readout based on TCP/IP inquiry/replay mode. The readout design of Central DAQ requires busy logic signals provided by detectors, which were not used in continuous readout system based on TRBv3.

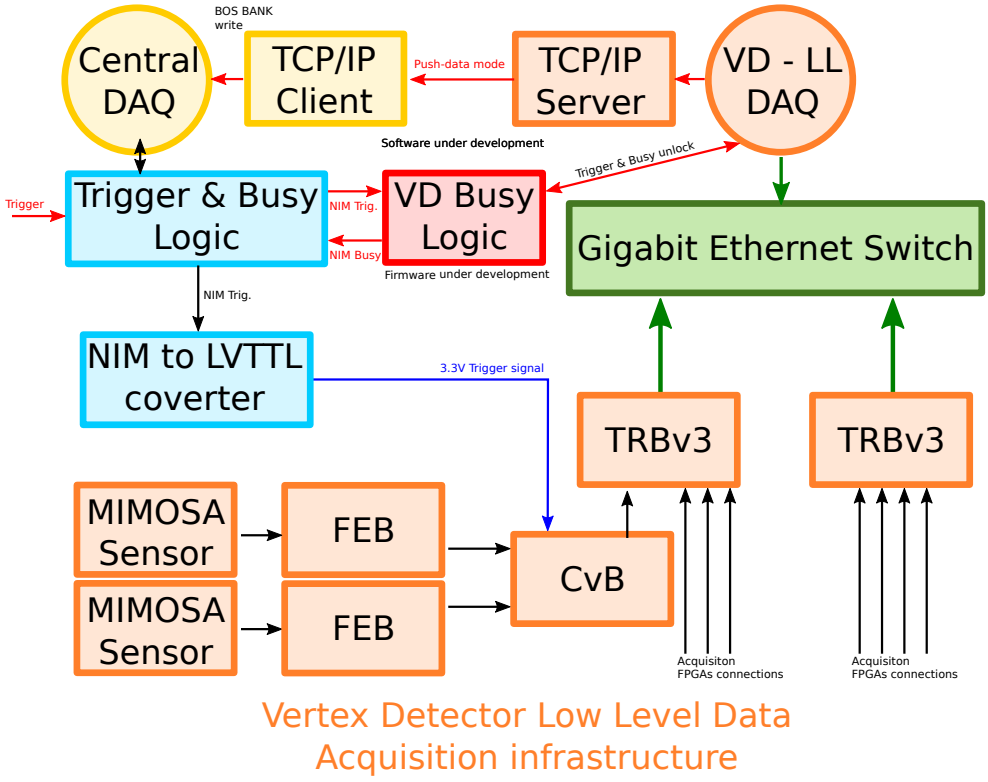

Figure 65: Vertex Detector readout diagram

To satisfy design requirements and additional busy logic piece of hardware was introduced. In figure 65 there is a diagram of VD readout system with centrally placed, red coloured block "VD Busy Logic" which will provide busy NIM signals after the trigger NIM signal arrives and hold it until the data from Low Level DAQ are transferred to Central DAQ.

The Busy Logic is based on Arduino Leonardo compatible micro-controller board connecting to VD Low Level DAQ computer by USB. It uses logic level converting cir-

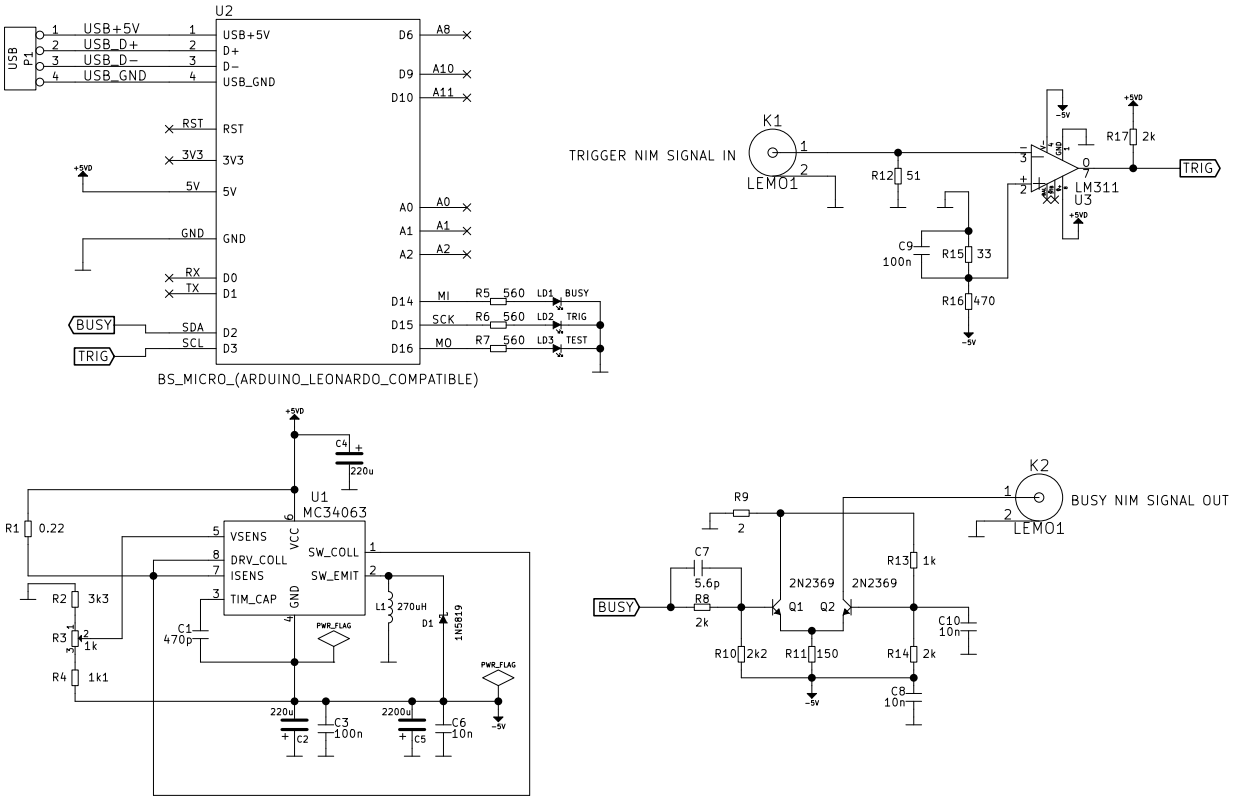

Figure 66: Vertex Detector Busy Logic schematic

cuits: NIM $\rightarrow$ TTL and TTL $\rightarrow$ NIM. Prototype unit is powered from USB connector (which provides +5 V), than it generates -5 V needed by level converters using the DC-DC switching regulator MC34063. The busy logic schematic is provided in Fig. 66.

As of the mid September, Central DAQ software is prepared for software integration. The work is ongoing on this for November/December tests.

A.5 Tolerance of the VD sensors to heavy ions

The SAVD of NA61/SHINE will be located as close as 3 mm from the beam axis. Therefore, the sensors forming the detector are exposed to a non-negligible flux of primary beam ions. Based on measured beam profiles shown in Fig. 67, the heavy ion flux impinging the sensors was estimated to reach $\sim 10^9$ ions/cm^2 for the most exposed region of SAVD.

Those ions generate both ionizing and non-ionizing radiation damage in the sensors. The ionizing radiation doses were estimated based on the Bethe-Bloch formula, which is considered as a reasonably reliable tool. It was found that the sensors will be exposed to an integrated ionizing radiation dose of slightly above 200 krad for a run of 40 days. This amount is slightly above the nominal radiation tolerance of the sensors but the issue may be solved by a scheduled replacement of the two affected sensors. The

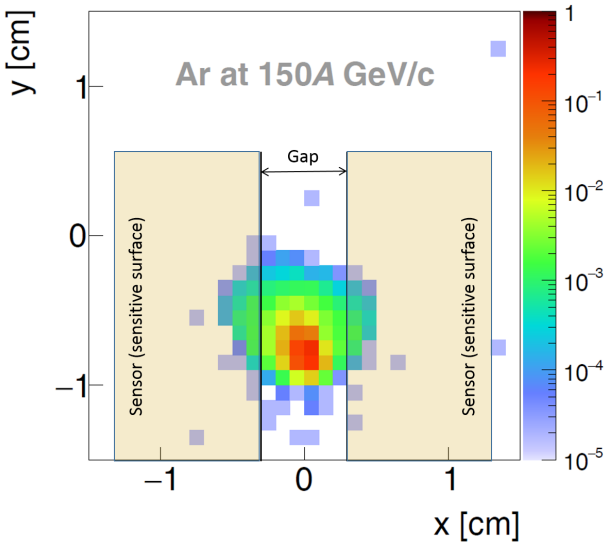

Figure 67: Measured profile of the primary Ar beam at 150A GeV/c at the NA61/SHINE target. The tails are suppressed by the veto counters around the beam. The gap of the SAVD ($\pm$3 mm) and the anticipated position of the sensors is shown. The numbers are normalized to one beam ion.

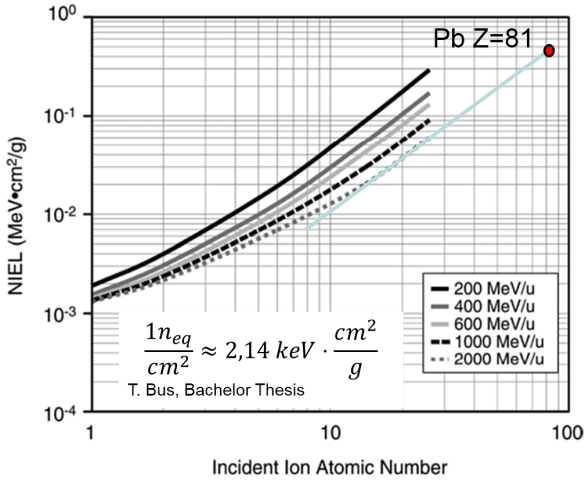

Figure 68: Non Ionising Energy Loss (NIEL) as a function of atomic number and energy of the ion. The extrapolation employed for estimating the non-ionizing radiation damage (see text for details) is shown by the red dot. Plot from Ref. [65].

integrated non-ionizing radiation dose is by far more difficult to estimate as there is few theoretical and empirical knowledge available so far. Results from a theoretical calculation can be found in [65] (see Fig. 68), which provides an estimate for ions lighter than

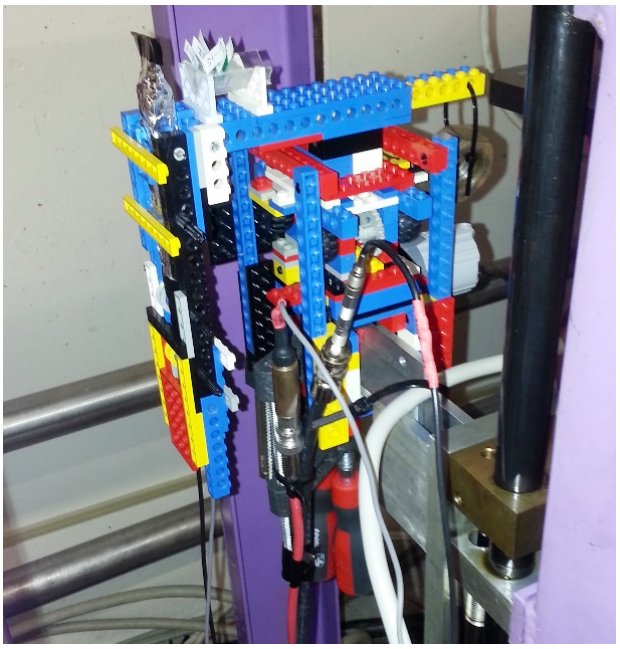

Figure 69: Holding structure used for the irradiating the CMOS sensor. The sensors are held by the V-shaped holder on top of the installation. The scintillator detector used for dosimetry is located at the left (upstream) side.

iron and energies below $2A$ GeV. An extrapolation of those estimates suggest that the hardness factor for heavy ions might be in the order of few 100 n_{eq} per highly relativistic lead ion. However, it was not clear if this coarse extrapolation is valid. Moreover, it was questioned if the NIEL model would be suited to predict the response of the partially depleted CMOS sensors to this rather exotic radiation. It was therefore decided to perform a specific experiment.

To do so, eight CMOS sensors were exposed to primary $30A$ GeV/c Pb-ions at SPS. Four of the sensors were MIMOSA-18AHR, which are manufactured in an AMS 0.35 µm high resistivity process. Those sensors are considered as representative for the MIMOSA-26AHR sensors used in the SAVD. Moreover, four MIMOSA-34THR sensors with 18 µm high resistivity epitaxial layer were irradiated. Those sensors are were produced in the Tower/Jazz 0.18 µm technology, which will presumably be used for the sensors of the ALICE-ITS upgrade and of the future CBM Micro Vertex Detector. To perform the irradiation, the sensors were mounted on a dedicated, remote controlled positioning table and placed 200 m upstream the target into the beam line of NA61/SHINE. The table was designed to move the sensors horizontally, while a vertical movement was provided by stationary installations of the beam line. Combining both installations allowed to find and to follow the beam without accessing the beam line. Dosimetry was provided by an ion sensitive, 4×4 mm^2 small scintillator. This scintillator together with its light guide and a suited, small PMT were placed on the support upstream the sensors. The signals

of the PMT were forwarded to the NA61/SHINE counting house and the dosimetry was performed by means of single ion counting.

The positioning table obtained a certain attention as it was implemented with LEGO Technic (see Fig. 69). This flexible, cost- and time efficient solution was chosen assuming that the plastic material would be mostly immune to activation and cause only a restricted multiple scattering of the primary beam. The Power Functions XL engine moving the table was controlled with the related standard LEGO 6 AA battery box. A distance of 150 m between both could be bridged by cutting a 50 cm long LEGO-cable and prolongating it with a 150 m long standard 1.5 mm^2 cables as used for 220V house installations. No position sensors were implemented, the table was controlled by the known moving speed and the time of movement. This procedure allowed for a position accuracy of $\sim$ 1 mm, which matched the requirements. As expected, the activation of the moving table including the scintillator and the PMT was found to be marginal (8 Bq of ^{7}Be were spotted after an exposition of $\sim 10^{10}$ Pb ions/cm^2).

The sensors were exposed to a maximum ion flux of 1.2×10^{10} Pb ions/cm^2. Hereafter, they were bonded at the IPHC Strasbourg and measurements of their properties were performed at Goethe University Frankfurt/M by members of the CBM collaboration. To do so, the sensors were operated illuminated with X-rays from a ^{55}Fe-source, which generates a known signal charge of 1640 electrons in the active volume of the sensors. Most of this charge is collected by a small group of pixels and the charge collected by a given number of grouped pixels devided by the total signal charge injected is denoted as the charge collection efficiency (CCE).

The CCE is considered as a sensitive tool for estimating impact of non-ionizing radiation damage. This is as massive particles remove silicon atoms from their location in the crystal lattice and such create pairs of interstitial atoms and vacations. In the case of massive damage, one expects sizeable clusters in which the crystal lattice is fully destroyed. From the electronic side, those crystal defects may trap signal electrons and force them to recombine with nearby holes. This effect turns into a drop of the CCE, which can easily be observed as a shift of the related peak in an amplitude spectrum.

Figure 70 shows an amplitude spectrum of a pixel array with 33×66 μm^2 pitch of the most irradiated MIMOSA-34. This pixel was chosen as it is considered to be most vulnerable to radiation and significant radiation effects were expected at doses above $\sim 3 \times 10^{12}$ n_{eq}/cm^2. The amplitude spectrum of the irradiated sensor is compared with the one of a non-irradiated, similar device. As one can see, the position of the signal peaks at $\sim$ 420 ADU depends only marginally of the radiation dose. The $\sim$ 5% drop in signal amplitude (and CCE) is considered as close to the uncertainty of the measurement procedure and can in any case be considered as having no practical impact on the sensor operation. The noise of the pixel was also checked and no significant noise increase due to irradiation was observed.

A preliminary interpretation of the ongoing study suggests therefore, that the most vulnerable pixel of the most irradiated sensor survived the radiation in first order without significant radiation damage. As this dose is by about one order of magnitude above the value expected for the NA61/SHINE SAVD, one may safely conclude that in con-

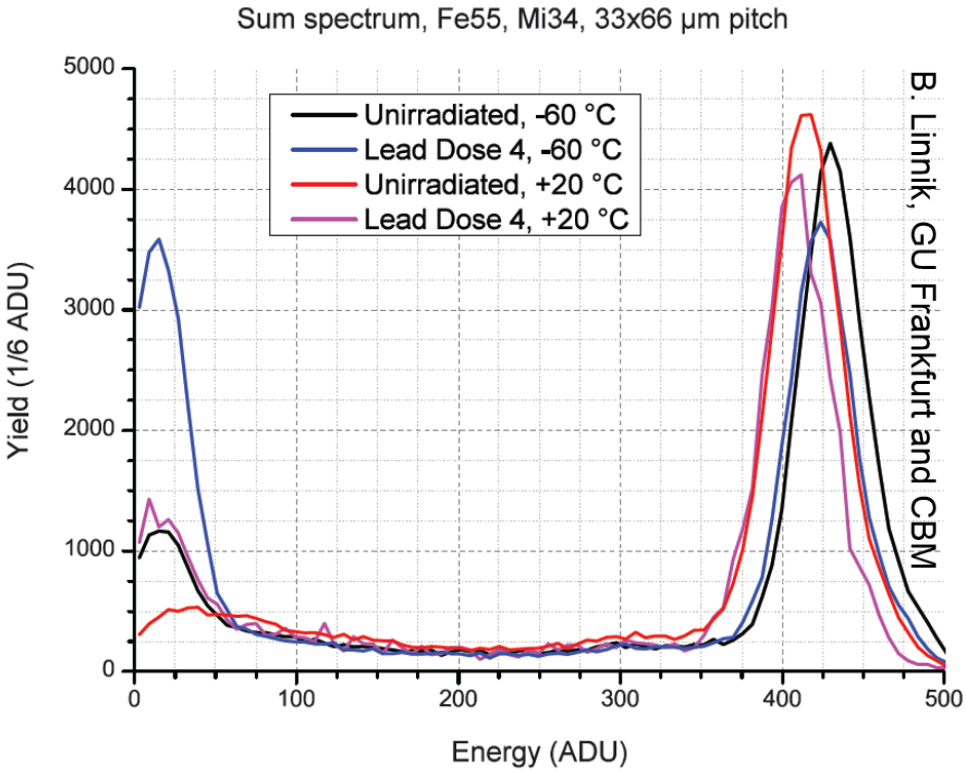

Figure 70: Amplitude spectrum of MIMOSA-34 for a non-irradiated sensor and the sensor exposed to the highest ion dose. The signal of groups of 25 pixels was added.

trast to the ionizing radiation damage, the non-ionizing radiation damage caused by primary beam ions is not of a worry for the operation of the SAVD detector.

In a next step, the data obtained from the irradiated sensors will be scanned for more possible, more subtle radiation effects. This activity aims to improve our global understanding of radiation effects of heavy ions in silicon detectors.

A.6 VD software status in SHINE

The complete software chain for simulation, reconstruction, calibration and analysis is being implemented in the NA61/SHINE software frame-work SHINE. Figure 71 shows a simplified view of this chain. Input data may be obtained either from real detector data or simulated data.

The part of SHINE responsible for simulations is called Luminance, and is based on GEANT4. A SAVD model has been implemented in this frame-work, and has been used to develop and test tracking algorithms. Also, performance comparisons of potential future large-acceptance versions of the VD was carried out in this frame-work. The digitiser to produce simulated raw data from the sensor signal response is still in

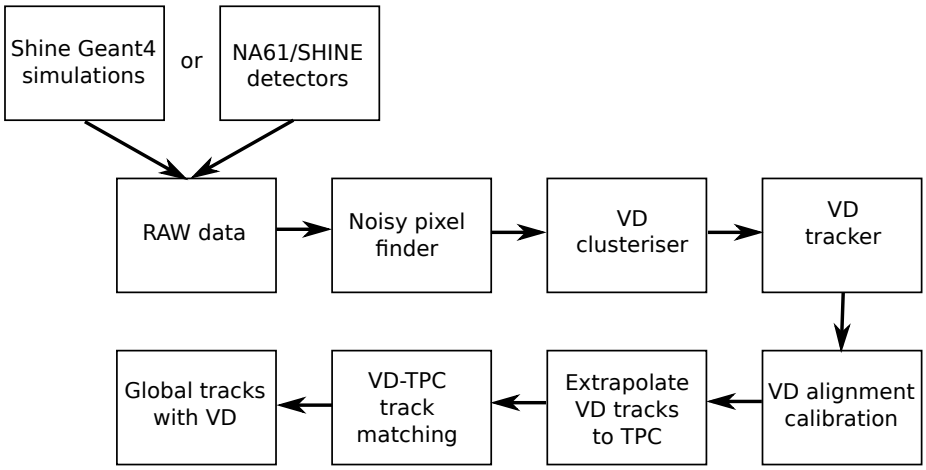

Figure 71: Overall SAVD data processing chain.

development, instead tracks produced by GEANT4 is used directly.

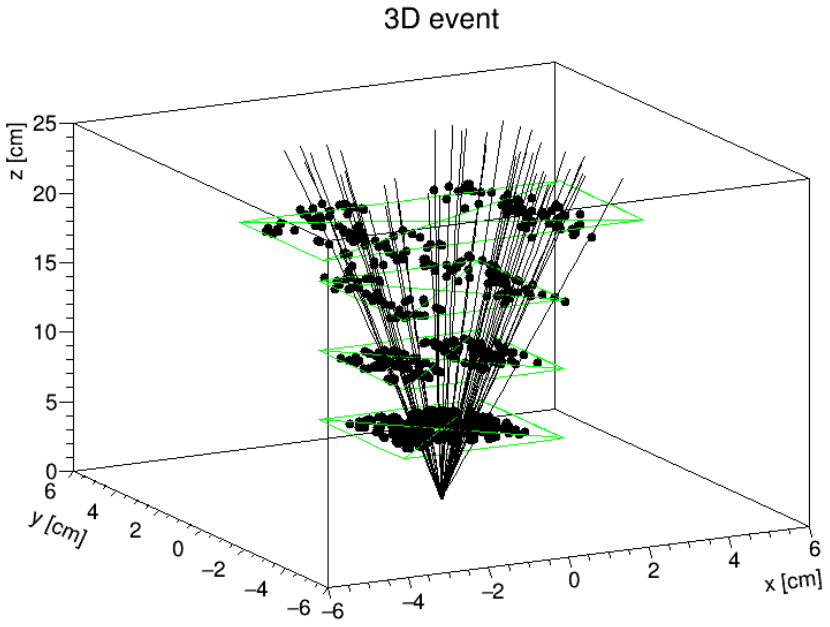

Figure 72: Reconstruction of Pb+Pb 158 GeV/c event simulated in Luminance.

Track reconstruction for SAVD is based on a global method when all points are processed in the same way and the speed of such method depends only on number of hits which makes it faster then local methods. As the track reconstruction method the Hough transform is implemented. It uses a parametric description of a track by a set of parameters. Once the track model is chosen coordinate space of the detector measurement could be transformed into the track parameter space. Then, in this so-called

accumulator space using the voting procedure track candidates are obtained as local maxima: the most popular candidates assumed to be real tracks.

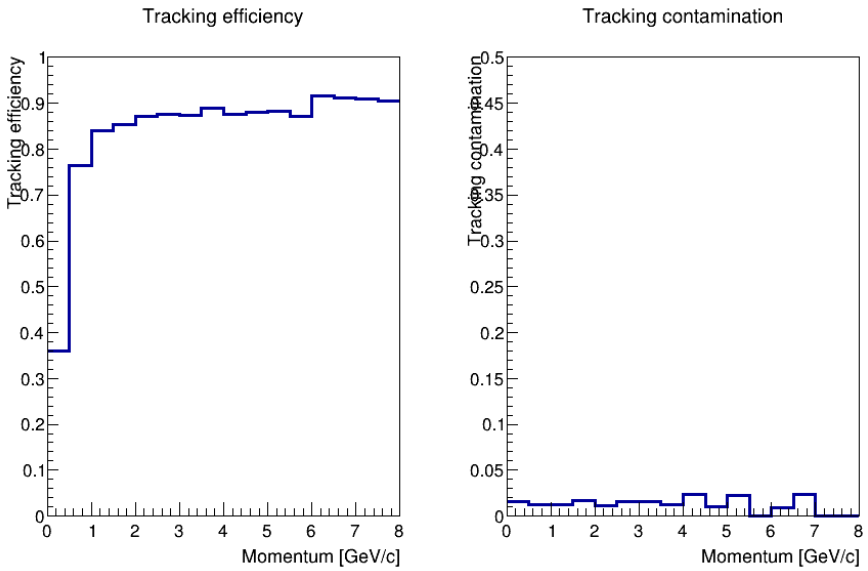

Figure 73: Efficiency of VD track reconstructed in Shine from simulated data.

The magnetic field in the SAVD volume is inhomogeneous (0.13 ÷0.25 T), and as the track model were chosen parabola in (x-z)-plane and linear in (y-z)-plane, i.e.

$$x = c^2 z + a_x z + b_x, \quad y = a_y z + b_y.$$

Figure 72 ilustrates reconstruction result of central Pb+Pb collisions at 158A GeV/c simulated in GEANT. In Fig. 73 the reconstruction efficiency (number of true reconstructed tracks divide by number of reconstructable tracks) and contamination (number of fake reconstructed tracks divide by number of reconstructable tracks) are plotted as a function of particle momentum.

The magnetic field in SAVD volume allows momentum reconstruction for SAVD-tracks:

$$p_{xz} = \frac{Ze \int B_y dl}{\sin \alpha_1 - \sin \alpha_2},$$

where α_1, α_2 - angles of the track on the first and last stations. Figure 74 shows the distribution of the reconstructed momentum and true momentum (from GEANT). Sigma of this distribution is 0.76 GeV/c. The momentum reconstruction in difficult as the field is weak and inhomogeneous, but this values could help in matching SAVD-tracks and TPC-tracks.

Following tracking, a calibration procedure should be applied to calculate correction values for the sensor alignment. The procedure has been demonstrated on data outside

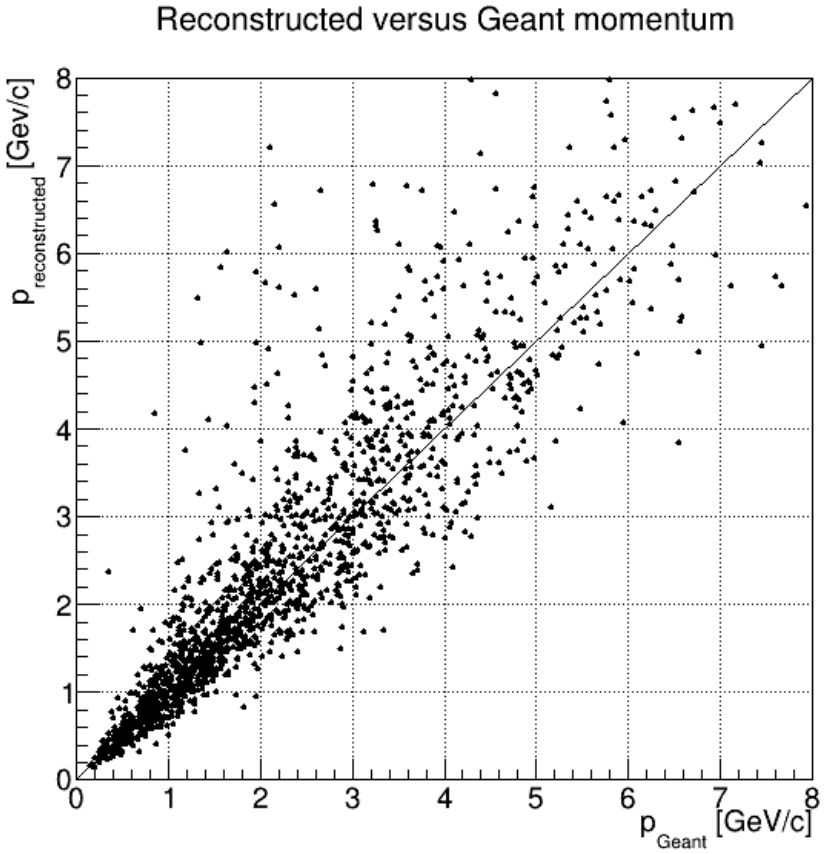

Figure 74: Comparison between simulated particle momentum and the reconstructed one using resulted from the SAVD data simulation and reconstruction.

the SHINE framework, and it now being transferred to SHINE. The procedure also has to take into account the alignment of the two arms as well as the target position. The calibrated valued may be applied to the next iteration of data reconstruction

Tracks are being reconstructed separately in TPCs and SAVD. The tracking algorithms employed in TPCs assumes a relatively dense path of hits, and is not suited for tracking in silicon detectors, where there are only hits at a few sparse stations. The tracks will be merged by extrapolating the SAVD tracks to the surface of VTPC-1. Here, matching tracks will be searched for by comparing track location, slope and momenta. Finally, global tracks will be created from the successfully merged tracks. The matching of SAVD and TPC tracks is currently under development.

B List of Recorded Data and Physics Results

1. p+p collisions at 13, 20, 31, 40, 80, and 158 GeV/c
   (a) Published results on π^- production in p+p at 20–158 GeV/c; based on h^- method [9]
   (b) Preliminary results on $\pi^\pm$, $K^\pm$, $(anti)p$ production in p+p at 20–158 GeV/c; based on information from dE/dx and $tof - dE/dx$ [66]; see also Ref. [67] for identified particle multiplicities in 4π
   (c) Published results on Λ production in p+p at 158 GeV/c [18]
   (d) Preliminary results on Λ production in p+p at 40 GeV/c [68]
   (e) Almost published (accepted by EPJC) results on transverse momentum and multiplicity fluctuations of non-identified hadrons in p+p at 20–158 GeV/c [26]; a new set of preliminary results for p+p in a slightly different acceptance was shown in Refs. [69,70]
   (f) Preliminary results on two-particle correlations of non-identified hadrons in azimuthal angle and pseudo-rapidity in p+p at 20–158 GeV/c [71,72]
   (g) Preliminary results on multiplicity fluctuations of identified particles (chemical fluctuations) in p+p at 31–158 GeV/c [73]; additional preliminary results on $\pi^+\pi^-$ fluctuations were shown in Refs. [74,75]
   (h) Preliminary results on higher order moments of multiplicity and net-charge fluctuations in p+p at 31–158 GeV/c [76], [69]
2. Be+Be collisions at 13A, 19A, 30A, 40A, 75A, and 150A GeV/c
   (a) Preliminary results on π^- production in Be+Be at 20–150A GeV/c; based on h^- method [77,78]
   (b) Preliminary results on cross-section in Be+Be at 13–150A GeV/c [69,77] (Ref. [69] shows updated results and for all energies)
   (c) Preliminary results on transverse momentum and multiplicity fluctuations of non-identified hadrons in Be+Be at 19–150A GeV/c [27,69] (those two references show results in slightly different acceptances)
   (d) Preliminary results on long-range correlations (in multiplicities and mean transverse momenta) in Be+Be at 150A GeV/c [79]
   (e) Preliminary results on long-range fluctuations (in electric charge) in Be+Be at 150A GeV/c [80]
3. Ar+Sc collisions at 13A, 19A, 30A, 40A, 75A, and 150A GeV/c
   (a) Preliminary results on π^- production in Ar+Sc at 13–150A GeV/c; based on h^- method [81], [82], [69]

(b) Preliminary results on transverse momentum and multiplicity fluctuations of non-identified hadrons in Ar+Sc at 19–150A GeV/c [70], [69]

(c) Preliminary results on multiplicity and multiplicity-forward energy fluctuations in Ar+Sc at 19–150A GeV/c [83], [69]

4. p+C collisions at 31 GeV/c (thin target and T2K replica target)

   (a) Measurements of $\pi^{\pm}$, $K^{\pm}$, K^0_S, Λ and proton production in proton-carbon interactions at 31 GeV/c [44], [84], [85], [86]

   (b) Measurements of $\pi^{\pm}$ differential yields from the surface of the T2K replica target for incoming 31 GeV/c protons [45]

5. π^-+C collisions at 158 and 360 GeV/c

   (a) Preliminary results on charged hadron production in π^-+C interactions at 158 and 360 GeV/c [87]

   (b) Preliminary results on charged pion production in π^-+C interactions at 158 and 360 GeV/c [88, 89]

   (c) Preliminary results on ρ^0 production in π^-+C interactions at 158 and 360 GeV/c [89]

References

[1] N. Antoniou *et al.*, [NA61/SHINE Collab.], "Study of hadron production in hadron nucleus and nucleus nucleus collisions at the CERN SPS," 2006. CERN-SPSC-2006-034.

[2] A. Dudarev (CERN), 2016. https://indico.cern.ch/event/512364/contributions/2301954/attachments/1338755/2015125/NA61_SHINE_Collaboration_meeting_on_19092016.pdf. NA61/SHINE Collaboration Meeting, CERN.

[3] S. Ravat (CERN), 2016. https://indico.cern.ch/event/512364/contributions/2301956/attachments/1338734/2016135/MSS2NA61.pdf. NA61/SHINE Collaboration Meeting, CERN.

[4] T. Dupont (CERN), 2016. https://indico.cern.ch/event/512364/contributions/2301957/attachments/1338174/2016169/New_Detection_quench_system_NA61.pdf. NA61/SHINE Collaboration Meeting, CERN.

[5] A. Aduszkiewicz, [NA61/SHINE Collab.], "Beam momentum scan with Pb+Pb collisions," Tech. Rep. CERN-SPSC-2015-038. SPSC-P-330-ADD-8, CERN, Geneva, Oct, 2015. https://cds.cern.ch/record/2059811.

[6] B. Abelev *et al.*, [ALICE Collab.] *J. Phys. G: Nucl. Part. Phys.* **41** (2014) 087002. https://cds.cern.ch/record/1625842.

[7] A. Aduszkiewicz, [NA61/SHINE Collaboration Collab.], "Report from the NA61/SHINE experiment," Tech. Rep. CERN-SPSC-2015-036. SPSC-SR-171, CERN, Geneva, Oct, 2015. http://cds.cern.ch/record/2059310.

[8] S. Ritt, R. Dinapoli, and U. Hartmann *Nucl. Instrum. Meth.* **A623** (2010) 486.

[9] N. Abgrall *et al.*, [NA61/SHINE Collab.] *Eur.Phys.J.* **C74** (2014) 2794, arXiv:1310.2417 [hep-ex].

[10] S. Afanasiev *et al.*, [NA49 Collab.] *Phys. Rev.* **C66** (2002) 054902.

[11] C. Alt *et al.*, [NA49 Collab.] *Phys. Rev.* **C77** (2008) 024903.

[12] W. Broniowski, M. Rybczynski, and P. Bozek *Comput.Phys.Commun.* **180** (2009) 69.

[13] K. Werner *Nucl. Phys. Proc. Suppl.* **175-176** (2008) 81–87.

[14] A. Golokhvastov *Phys.Atom.Nucl.* **64** (2001) 84–97.

[15] M. Gazdzicki and M. I. Gorenstein *Acta Phys.Polon.* **B30** (1999) 2705, arXiv:hep-ph/9803462 [hep-ph].

[16] I. Tanihata *et al. Phys. Rev. Lett.* **55** (1985) 2676.

[17] K. A. Olive *et al.*, [Particle Data Group Collab.] *Chin. Phys.* **C38** (2014) 090001.

[18] A. Aduszkiewicz *et al.*, [NA61/SHINE Collab.] *Eur. Phys. J.* **C76** no. 4, (2016) 198, arXiv:1510.03720 [hep-ex].

[19] V. Blobel *et al.*, [Bonn-Hamburg-Munich Collab.] *Nucl. Phys.* **B69** (1974) 454–492.

[20] V. V. Ammosov *et al. Nucl. Phys.* **B115** (1976) 269–286.

[21] M. Gazdzicki and D. Rohrich *Z.Phys.* **C71** (1996) 55–64, arXiv:hep-ex/9607004 [hep-ex].

[22] S. Bass *et al. Prog.Part.Nucl.Phys.* **41** (1998) 255–369, arXiv:nucl-th/9803035 [nucl-th].

[23] M. Bleicher *et al. J.Phys.* **G25** (1999) 1859–1896, arXiv:hep-ph/9909407 [hep-ph].

[24] B. Andersson, G. Gustafson, and H. Pi *Z. Phys.* **C57** (1993) 485–494.

[25] J. Geiss, W. Cassing, and C. Greiner *Nucl. Phys.* **A644** (1998) 107–138, arXiv:nucl-th/9805012 [nucl-th].

[26] A. Aduszkiewicz *et al.*, [NA61/SHINE Collab.] arXiv:1510.00163 [hep-ex].

[27] T. Czopowicz, [NA61/SHINE Collab.] *PoS* **CPOD2014** (2015) 054, arXiv:1503.01619 [nucl-ex].

[28] T. Anticic *et al.*, [NA49 Collab.] *Phys. Rev.* **C92** no. 4, (2015) 044905, arXiv:1509.04633 [nucl-ex].

[29] M. I. Gorenstein and K. Grebieszkow *Phys.Rev.* **C89** no. 3, (2014) 034903, arXiv:1309.7878 [nucl-th].

[30] M. I. G. R. V. Poberezhnyuk and M. Gazdzicki arXiv:1509.06557 [hep-ph].

[31] M. Gorenstein and M. Gazdzicki *Phys. Rev.* **C84** (2011) 014904.

[32] V. V. Begun, M. Gazdzicki, M. I. Gorenstein, M. Hauer, V. P. Konchakovski, and B. Lungwitz *Phys. Rev.* **C76** (2007) 024902, arXiv:nucl-th/0611075 [nucl-th].

[33] V. V. Begun, M. Gazdzicki, and M. I. Gorenstein *Phys. Rev.* **C78** (2008) 024904, arXiv:0804.0075 [hep-ph].

[34] C. Alt *et al.*, [NA49 Collab.] *Phys. Rev.* **C78** (2008) 034914.

[35] M. A. Stephanov *Phys. Rev. Lett.* **102** (2009) 032301, arXiv:0809.3450 [hep-ph].

[36] M. A. Stephanov *Phys. Rev. Lett.* **107** (2011) 052301, arXiv:1104.1627 [hep-ph].

[37] C. Alt *et al.*, [NA49 Collab.] *Phys. Rev.* **C68** (2003) 034903, arXiv:nucl-ex/0303001 [nucl-ex].

[38] C. Alt *et al.*, [NA49 Collab.] *Phys. Rev.* **C75** (2007) 044901, arXiv:nucl-ex/0606026 [nucl-ex].

[39] L. Adamczyk *et al.*, [STAR Collab.] *Phys. Rev. Lett.* **112** no. 16, (2014) 162301, arXiv:1401.3043 [nucl-ex].

[40] V. Klochkov and I. Selyuzhenkov, [CBM Collab.] *GSI Scientific Report 2015 :DOI:10.15120/GR-2016-1, MU-NQM-CBM-22* https://repository.gsi.de/record/194850 (2016) 8.

[41] I. Selyuzhenkov and S. Voloshin *Phys. Rev.* **C77** (2008) 034904, arXiv:0707.4672 [nucl-th].

[42] V. Gonzalez, J. Onderwaater, and I. Selyuzhenkov, [ALICE Collab.] *GSI Scientific Report 2015 :DOI:10.15120/GR-2016-1, MU-NQM-ALICE-11* https://repository.gsi.de/record/194850 (2016) 23.

[43] J. Onderwaater, I. Selyuzhenkov, and V. Gonzalez https://github.com/jonderwaater/FlowVectorCorrections (2015) available under GNU General Public License v.3.

[44] N. Abgrall *et al.*, [NA61/SHINE Collab.] *EPJ* **C76** no. 2, (2016) 84.

[45] N. Abgrall *et al.*, [NA61/SHINE Collab.] arXiv:1603.06774 [hep-ex].

[46] A. Carroll *et al. Phys. Lett.* **B80** (1979) 319.

[47] R. Engel, D. Heck, and T. Pierog *Ann. Rev. Nucl. Part. Sci.* **61** (2011) 467–489.

[48] J. Abraham *et al.*, [Pierre Auger Collab.] *Nucl. Instrum. Meth.* **A523** (2004) 50–95.

[49] G. Navarra *et al. Nucl. Instrum. Meth.* **A518** (2004) 207–209.

[50] R. Abbasi *et al.*, [IceCube Collab.] *Nucl. Instrum. Meth.* **A700** (2013) 188–220, arXiv:1207.6326 [astro-ph.IM].

[51] T. Abu-Zayyad *et al. Phys. Rev. Lett.* **84** (2000) 4276–4279.

[52] T. Abu-Zayyad *et al.*, [Telescope Array Collab.] *Nucl. Instrum. Meth.* **A689** (2013) 87–97, arXiv:1201.4964 [astro-ph.IM].

[53] J. C. Arteaga-Velazquez *et al. EPJ Web Conf.* **52** (2013) 07002.

[54] A. Aab *et al.*, [Pierre Auger Collab.] *Phys. Rev.* **D91** (2015) 032003.

[55] A. Aab *et al.*, [Pierre Auger Collab.] *Phys. Rev.* **D90** (2014) 012012.

[56] S. Ostapchenko *Phys.Rev.* **D83** (2011) 014018, arXiv:1010.1869 [hep-ph].

[57] T. Pierog, I. Karpenko, J. M. Katzy, E. Yatsenko, and K. Werner *Phys. Rev.* **C92** no. 3, (2015) 034906, arXiv:1306.0121 [hep-ph].

[58] F. Riehn *et al. PoS* **(ICRC2015)** (2015) 558, arXiv:1510.00568.

[59] D. S. Barton *et al. Phys. Rev.* **D27** (1983) 2580.

[60] M. Adamus *et al.*, [NA22 Collab.] *Z. Phys.* **C35** (1987) 7. [Sov. J. Nucl. Phys.47,271(1988)].

[61] I. V. Azhinenko *et al.*, [EHS/NA22 Collab.] *Z. Phys.* **C46** (1990) 525–536.

[62] N. Agababyan *et al.*, [EHS-NA22 Collaboration Collab.] *Z.Phys.* **C46** (1990) 387–395.

[63] A. Herve, [NA61/SHINE Collab.] in *PoS* [89], p. 330, arXiv:1509.06586 [nucl-ex].

[64] T.-P. Li and Y.-Q. Ma *Astrophys. J.* **272** (Sept., 1983) 317–324.

[65] M. Xapsos *et al. IEEE TNS* **51** no. 6, (2004) 3250–3254.

[66] S. Pulawski, [NA61 Collab.] *PoS* **CPOD2014** (2015) 010, arXiv:1502.07916 [nucl-ex].

[67] A. Aduszkiewicz, [NA61/SHINE Collab.], "Report from the NA61/SHINE experiment at the CERN SPS," Oct, 2015. http://cds.cern.ch/record/2059310.

[68] H. Stroebele, [NA61/SHINE Collab.], "New(s) from NA61: Λ in p+p and π^- in Ar+Sc," 2016. talk at the 16th International Conference on Strangeness in Quark Matter (SQM 2016) Berkeley, USA, June 27-July 1, 2016 (proceedings to be published), https://indico.cern.ch/event/403913/contributions/2142033/attachments/1300036/1940346/1000_HS-SQM16_final.pdf .

[69] K. Grebieszkow, [NA61/SHINE Collab.], "News from strong interactions program of the NA61/SHINE experiment," in *10th International Workshop on Critical Point and Onset of Deconfinement (CPOD 2016) Wroclaw, Poland, May 30-June 4, 2016*. 2016. arXiv:1608.01538 [nucl-ex]. http://inspirehep.net/record/1479456/files/arXiv:1608.01538.pdf.

[70] E. Andronov, [NA61/SHINE Collab.], "Transverse momentum and multiplicity fluctuations in Ar+Sc collisions at CERN SPS from NA61/SHINE," 2016. talk at 10th International Workshop on Critical Point and Onset of Deconfinement (CPOD 2016) Wroclaw, Poland, May 30-June 4, 2016 (proceedings to be published), https://indico.cern.ch/event/449173/contributions/2167165/attachments/1280888/1902801/EA_cpod.pdf .

[71] B. Maksiak, [NA61/SHINE Collab.] *PoS* **CPOD2014** (2015) 055, arXiv:1503.02470 [nucl-ex].

[72] A. Aduszkiewicz *et al.*, [NA61/SHINE Collab.] arXiv:1610.00482 [nucl-ex].

[73] M. Mackowiak-Pawlowska, [NA61/SHINE Collab.] *PoS* **CPOD2013** (2013) 048.

[74] N. Abgrall, [NA61/SHINE Collab.], "Report from the NA61/SHINE experiment at the CERN SPS," Oct, 2014. http://cds.cern.ch/record/1955138.

[75] M. Mackowiak-Pawlowska, [NA61/SHINE Collab.], "Fluctuations and correlations from the energy scan in p+p and Be+Be interactions at the SPS energies," 2015. talk at the XI Polish Workshop on Relativistic Heavy-Ion Collisions, https://indico.cern.ch/event/348749/contributions/1754804/attachments/688461/945511/pwhir.pdf .

[76] M. Mackowiak-Pawlowska, [NA61/SHINE Collab.], "Higher order moments of net-charge and multiplicity distributions in p+p interactions at SPS energies from NA61/SHINE," 2016. talk at 10th International Workshop on Critical Point and Onset of Deconfinement (CPOD 2016) Wroclaw, Poland, May 30-June 4, 2016 (proceedings to be published), https://indico.cern.ch/event/449173/contributions/2167176/attachments/1284531/1909796/cpod2016_mmp.pdf .

[77] E. Kaptur, [NA61/SHINE Collab.] *PoS* **CPOD2014** (2015) 053.

[78] S. Pulawski, [NA61/SHINE Collab.] *Acta Phys. Polon.* **B46** no. 11, (2015) 2381, arXiv:1510.07794 [nucl-ex].

[79] A. Seryakov, [NA61/SHINE Collab.] *J. Phys. Conf. Ser.* **668** no. 1, (2016) 012077, arXiv:1510.00847 [nucl-ex].

[80] E. Andronov, [NA61/SHINE Collab.] *J. Phys. Conf. Ser.* **668** no. 1, (2016) 012036, arXiv:1510.00174 [nucl-ex].

[81] M. Naskret, [NA61/SHINE Collab.], "Mean pion multiplicities in Ar+Sc collisions," 2016. talk at 10th International Workshop on Critical Point and Onset of Deconfinement (CPOD 2016) Wroclaw, Poland, May 30-June 4, 2016 (proceedings to be published), https://indico.cern.ch/event/449173/contributions/2175377/attachments/1280844/1902710/05_25_16.pdf .

[82] M. Lewicki, [NA61/SHINE Collab.], "Pion spectra in Ar+Sc interactions," 2016. talk at 10th International Workshop on Critical Point and Onset of Deconfinement (CPOD 2016) Wroclaw, Poland, May 30-June 4, 2016 (proceedings to be published), https://indico.cern.ch/event/449173/contributions/2176292/attachments/1285437/1911664/cpod_draft.pdf .

[83] A. Seryakov, [NA61/SHINE Collab.], "Centrality determination and multiplicity fluctuations in Ar+Sc collisions at CERN SPS from NA61/SHINE," 2016. talk at 10th International Workshop on Critical Point and Onset of Deconfinement (CPOD 2016) Wroclaw, Poland, May 30-June 4, 2016 (proceedings to be published), https://indico.cern.ch/event/449173/contributions/2176683/attachments/1281405/1903798/Seryakov_CPOD_2016_v4.pdf .

[84] N. Abgrall *et al.*, [NA61/SHINE Collab.] *Phys.Rev.* **C89** no. 2, (2014) 025205, arXiv:1309.1997 [physics.acc-ph].

[85] N. Abgrall *et al.*, [NA61/SHINE Collab.] *Phys. Rev.* **C84** (2011) 034604.

[86] N. Abgrall *et al.*, [NA61/SHINE Collab.] *Phys. Rev.* **C85** (2012) 035210.

[87] M. Unger, [NA61/SHINE Collab.] *EPJ Web Conf.* **52** (2013) 01009, arXiv:1305.5281 [nucl-ex].

[88] H. Dembinski, [NA61/SHINE Collab.], 2013. Proc. 33rd International Cosmic Ray Conference (ICRC2013): Rio de Janeiro, Brazil, July 2-9, 2013.

[89] A. Herve, [NA61/SHINE Collab.] *PoS* **ICRC2015** (2016) 330, arXiv:1509.06586 [nucl-ex].